UNIVERSITÀ CAMPUS BIO-MEDICO
DI ROMA

SCHOOL OF ENGINEERING

PHD PROGRAM IN BIOENGINEERING AND BIOSCIENCES

XXXI COURSE 2015-2018

PHD THESIS

SMART TOOLS FOR ORTHOPAEDIC SURGERY WITH SENSING CAPABILITY: A NOVEL APPROACH

Candidate
Iacopo Portaccio

Supervisor
Prof. **Dino Accoto**

A thesis submitted in partial fulfillment of the requirements for the degree of Doctor of Philosophy in Bioengineering and Biosciences

IACOPO PORTACCIO: *Smart tools for orthopaedic surgery with sensing capability: a novel approach*, Ph.D. Thesis, 2019, December.

CONTACTS
☞ iacopo.portaccio@gmail.com

It was a dark and stormy night.

SNOOPY

ABSTRACT

Low back pain is a very common and unsolved health problem and a major cause of disability, affecting work performances and general well-being. It is estimated that it affects roughly 60–80% of the adult population in the US. The strategies for treating this pathology range from conservative management to surgery. Novel biological technologies, such as regenerative medicine and bio-artificial organs, are already being tested in human pilot clinical trials. These approaches are an emerging and promising therapeutic tool that might stop, delay or reverse intervertebral disc degeneration. All the above surgical procedures are commonly delivered by injections into the nucleus pulposus through the annulus fibrosus route. However, even small needle annulus fibrosus punctures (25 gauge) may affect intervertebral disc biomechanics, cellularity and biosynthesis. An alternative approach to the annulus fibrosus route, namely the transpedicular route, has been developed and tested: it allows to preserve the annulus fibrosus intact, while the nucleus pulposus is reached via the endplate route. For this purpose, it is necessary to create a deep hole into the vertebra along the transpedicular trajectory. Generally, rotative drills are used, which can cause intraoperative complications: damaging of surrounding soft tissues and overheating of adjacent tissues up to necrosis are not uncommon. Moreover, the procedure is manually performed: the surgeon dexterity and experience, in fact, play a crucial role in maintaining the route toward the end plate of the vertebra during drilling. The accurate and safe creation of a single transpedicular bone hole to access to intervertebral disc space represents therefore an engineering challenge in the new transpedicular procedure. With this aim, a novel system has been developed for guiding surgical tools used for intervertebral access creation. The proposed positioning system (PS) allows to enhance the positional accuracy of drilling task. The PS allows the manual advancement of the drilling tool constrained along a fixed trajectory, in order to preserve the natural haptic perception of the surgeon, who remains in charge of modulating the drilling force and the feeding rate according to the position of the drill bit in the bone. Furthermore, a trajectory

planning algorithm has been implanted for guiding the insertion towards the intervertebral space based only on the acquisition of a few fluoroscopic images. The insertion orientation, and therefore the regulation of the system joints configuration, can be planned by a software based on two perpendicular C-arm fluoroscopic images and starting from the identification of the insertion point and of the insertion direction drawn on the images by the surgeon. The system has been dimensioned to be compatible with the size of C-arm workspace and to minimally interfere with the surgical procedure and the work of the medical staff.

Furthermore, in order to enhance the safety of the procedure, ultrasonic technology has been adopted for developing a new ultrasonic drill for deep holes creation. Ultrasonic bone cutting has advantages in controlling tissue damages because it selectively cuts only mineralized tissues, avoiding damages to soft tissues for frequencies in the range of 25 - 35 kHz. In this work a development process for bone ultrasonic drill has been proposed. The whole ultrasonic drill has been designed in COMSOL Multiphysics® environment, exploiting the multi-domain tools for simulation. After the manufacturing, the ultrasonic drill has been characterized in terms of vibration properties. The experimental results are in agreement with the simulations.

The safety issues in spinal transpedicular procedures cannot be solely exhausted by taking into account the aforementioned solutions. Generally, the accuracy problem in bone drilling consists in finding the right drill termination moment to guarantee that the rear hole will not be widened. Different hardware and software solutions have been developed in order to estimate the drill position during drilling for detecting the bone layers breakthrough. Nevertheless, the main disadvantage of these techniques is the use of the pushing force generating drill bit advancement as effective signal to discriminate among different bone tissues when the feed rate is constant. Therefore, the adoption of these methods is ineffective in the proposed surgical positioning system, where the surgeon can manually control the advancement of the drill bit, thus preserving the haptic feedback that she/he receives from the interaction between the tool and the bone tissues. To address the problem of tissue characterization while leaving the surgeon in complete control of the transpedicular procedure, the *average impedance* parameter has been introduced. A custom drill, embedded with force and position sensors, which allows the evaluation

of this new parameter, has been developed. In this work the average impedance estimation results on porcine models are discussed. In addition, the average impedance results obtained on human vertebrae drilling tests are presented and compared with bone mineral density evaluated from CT scans. Finally, in this work it is shown the feasibility to use the ultrasonic drill in the process for the bone layers breakthrough detection, thanks to its capability of sensing of the thrust force applied during bone drilling. This represents a huge advantage, since: *i*) all the advantages of the ultrasonic cutting, already described, are assured; *ii*) a single device allows cutting and sensing features simultaneously.

SUPPORT FUNDING ACKNOWLEDGMENTS

This work was supported by Università Campus Bio- Medico di Roma within the project START-Disc (Smart Surgical platform for the Transpedicular delivery of Advanced Regenerative Therapies into the intervertebral DISC space).

CONTENTS

LIST OF FIGURES

LIST OF TABLES

1 CHALLENGES IN SPINE SURGERY

1.1 INTRODUCTION

Low Back Pain (LBP) is a very common health problem and a major cause of disability, affecting work performances and general well-being. The worldwide incidence of low back pain is increasing[23]. Several studies suggest that between 70% and 85% of the population in Europe will suffer from low back disorders at some point in life [24]. Globally, LBP is the leading cause of societal burden (health and financial), involving more than 600 million people all over the world [25]. In Figures 1, 2 and 3 the Disability-Adjusted Life Years (DALY), that is a measure of overall disease burden, in relation to the risk of suffering from LBP due to occupational factors, behavioral factors and high mass index, are shown. Despite LBP is often believed a disease, it is indeed a symptom that can result from several different known or unknown abnormalities or diseases [26]. In general, LBP is a complex condition whose risk factors include, but are not limited to, occupational posture, depressive moods, obesity, body height and age. However, in order to diagnose LBP, and consequently plan an appropriate treatment, it is necessary to take into account the etiology of LBP based on patients history, physical examinanation, and outcomes of the diagnostic tests. Many authors suggest a relation between etiology and disease of spine that causes LBP [15, 16]. In Table 1 a summary of it is shown.
A clearly identified cause of LBP are lumbar disc disorders. Discogenic low back pain is a social problem accounting for over 40% of the patients with chronic low back pain. The high incidence highlights the importance of identifying strategies to prevent and treat these disorders [27, 28, 29, 30].

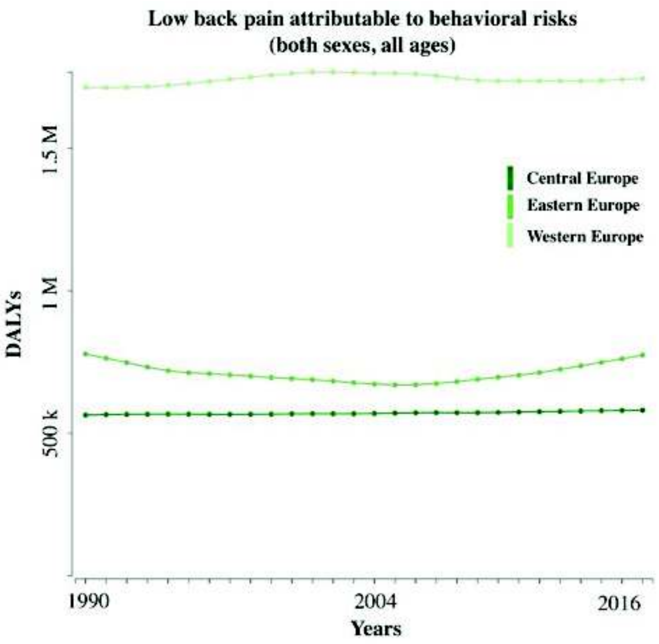

Figure 1: LBP attributable to behavioral risk, in disability-adjusted life-years (DALYs), since 1990 to 2017 in European region.

Institute for Health Metrics and Evaluation (IHME). GBD Compare. Seattle, WA: IHME, University of Washington, 2015. Available from http://vizhub.healthdata.org/gbd-compare. (Accessed July, 2019)

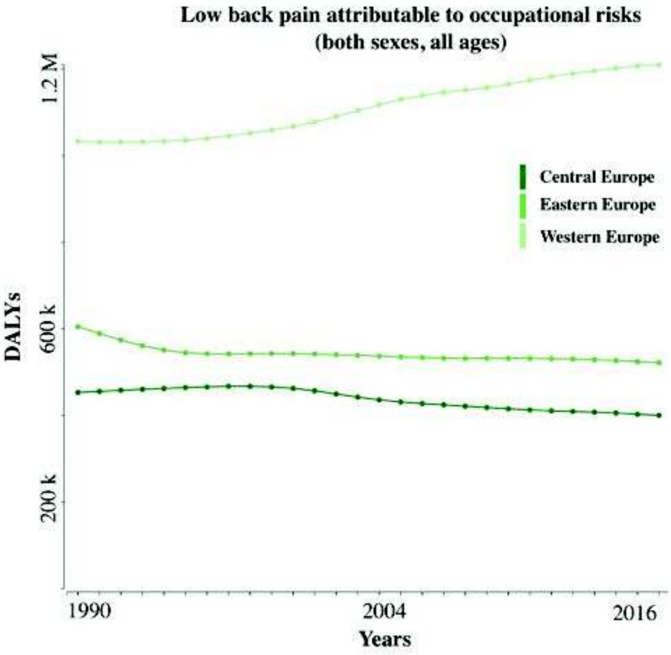

Figure 2: LBP attributable to occupational risk, in disability-adjusted life-years (DALYs), since 1990 to 2017 in European region.

Institute for Health Metrics and Evaluation (IHME). GBD Compare. Seattle, WA: IHME, University of Washington, 2015. Available from http://vizhub.healthdata.org/gbd-compare. (Accessed July, 2019)

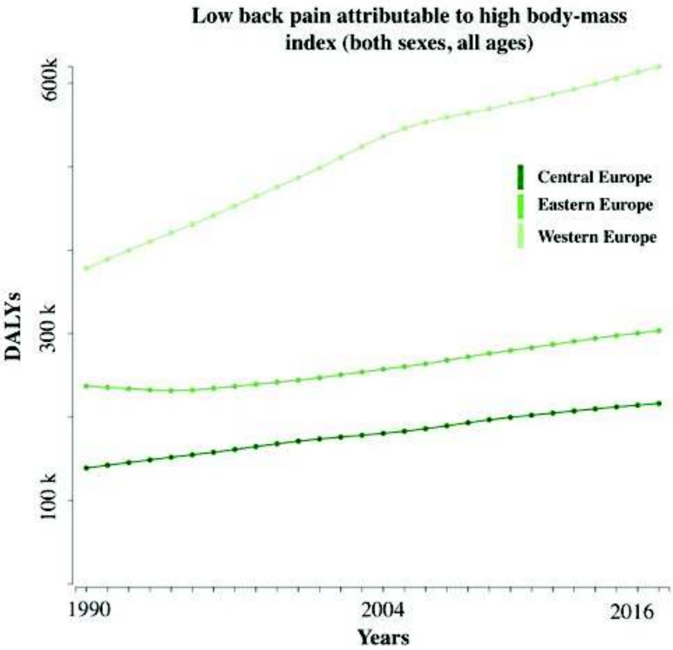

Figure 3: LBP attributable to high mass index, in disability-adjusted life-years (DALYs), since 1990 to 2017 in European region.

Institute for Health Metrics and Evaluation (IHME). GBD Compare. Seattle, WA: IHME, University of Washington, 2015.

Available from http://vizhub.healthdata.org/gbd-compare. (Accessed July, 2019)

Table 1: Etiology of LBP associated to possible diseases [15, 16].

Etiology	Disease
Trauma	Lumbar intervertebral disc hernia
	Fractures (associated with osteoporosis)
	Muscular/fascial low back pain
Inflammation	Tuberculous spondylitis
	Purulent spondylitis
	Infiammatory arthrisis
Neoplasia	Spondylosis deformans
	Metastatic carcinoma
	Spinal cord tumors
Degeneration	Spondylosis deformans
	Intervertebral disc degeneration
	Congenital disease
	Degeneration of facets, usually age-related
	Spinal stenosis
Visceral disease	Renal disease
	Disease of pelvic organs
	Gastrointestinal disease
Visceral disease	Psychogenic low back pain
	Hysteria
	Despression

Intervertebral disc degeneration is a natural process due to aging, albeit its exact causes are unknown. Different mechanisms may play a significant role, for example [31]:

- several gene alterations may contribute to degenerative cascade;
- mechanical stress may increase the intradiscal pressure and enhance the risk of structural damages;
- exposure to cigarette smoke may inhibit blood supply to discs.

Intervertebral disc degeneration primarily involves the *nucleus pulposus*, which is the gel-like core of the disc, with load bearing, shock-absorbing functions. It is confined by a multilamellar fibrocartilage, the *annulus fibrosus* [32]. With the loss of physiological properties, the nucleus becomes smaller and the inner pressure decreases, and so the compressive load is taken by the annulus fibrosus [1].

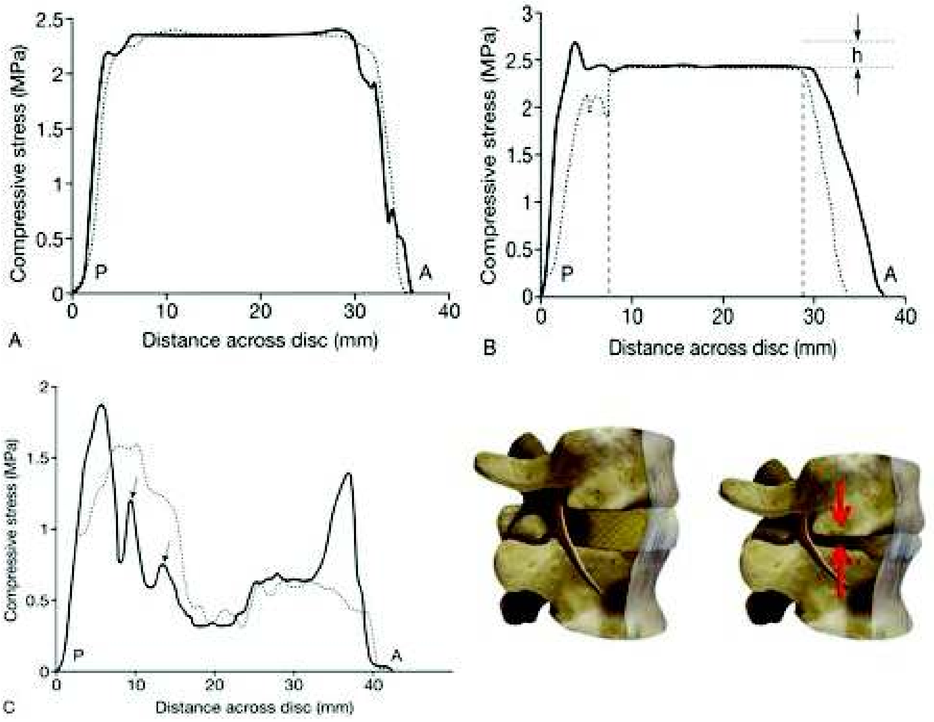

Figure 4: Stress profiles across the diameter of lumbar intervertebral discs subjected to 2 kN of compression. Vertical and horizontal stresses are indicated in solid and dot lines, respectively. The x-axis direction corresponds to posterior to anterior direction of vertebra. (A) Young disc. (B) Middle-aged disc, showing a stress concentration of magnitude "h" in the posterior annulus. (C) Degenerated disc with multiple stress concentrations in the annulus (arrow) [1]. In the bottom right-hand corner the global effect of disc degeneration.

The graphs in Figure 4 show how the compressive stress distribution varies for different grades of disc damage. The therapies for the management of the LBP associated with disc degeneration have primarily two goals [33]:

- **reduction of pain** through the administration of pharmacological or physical therapies;
- motor **function improvement** in daily activities.

Treatment of discogenic LBP ranges from conservative management, such as physical therapy and pain relieving medication, to highly invasive surgical intervention. Taking into account the surgical interventions, spinal fusion is still the standard surgical procedure for treatment of persistent discogenic

Figure 5: Rendering of spinal fixation.

LBP. Spinal fusion eliminates relative motion between two or more vertebrae through a "welding" procedure. Using pedicle screws, two metallic rods are fixed to the damage spine segment restoring stability (Figure 5). Despite some satisfactory outcomes, indications are uncertain and complications have been encountered, such as enhanced degeneration at adjacent disc levels.

Artificial disc replacement has therefore been suggested as an alternative to spinal fusion with the aim to better preserve the flexibility and range of motion at the operated level, while preventing degenerative changes in adjacent levels. However, recent studies suggest that the rate of complications after lumbar disc prosthesis treatment is considerable, especially in long term follow-up [34, 35, 36].

Novel biological technologies, such as gene therapy, cell therapy, tissue engineering, regenerative medicine and bio-artificial organs, are ready to enter, or are already being tested in human pilot clinical trials [37]. These approaches are an emerging and promising therapeutic tool that might stop, delay or reverse intervertebral disc degeneration. For example, recent evidence showed that treatments based on intradiscal injection of bone marrow mesenchymal stem/stromal cells (MSC) are clinically safe and effectively improve the course of intervertebral disc degeneration in vivo [37]. However, many aspects need to be further investigated to translate these methods to clinical applications. In particular, current research does not demonstrate which is the most efficient way to deliver the novel biological therapies and which is the least damaging surgical transplantation approach.

All the above surgical procedures are commonly delivered by injections into the nucleus pulposus through the annulus fibrosus route [38]. A major drawback of such surgical approaches is that the annulus fibrosus tissue is damaged, resulting in a compromised capability of containment of implanted materials or injected hydrogel into the nucleus. Moreover, even a very modest annulus fibrosus injury may induce or enhance a degenerative cascade of the disc [39, 40]. Several intervertebral disc degeneration animal models, based on annulus fibrosus damages ranging from punctures to stabbing, have been widely used in *in-vivo* interververtebral disc research [41]. Even small needle annulus fibrosus punctures (25 gauge) may affect intervertebral disc biomechanics, cellularity and biosynthesis [42]. Moreover, increased disc degeneration rate due to annulus punctures has been observed in a human study [43, 2]. A retrospective study, with 10 year follow-up, showed that discography performed through small needle punctures resulted in accelerated disc degeneration, higher disc herniation rate on the same side of the disc injection and changes in the endplate [43]. Furthermore, it has been recently shown on a rabbit disc degeneration model that the injection of MSCs into the nucleus pulposus through the annulus route may lead to cell leakage and accelerated osteophyte formation [44]. Similarly, a study that monitored the distribution of MSCs following *in-vivo* injection into nucleotomised porcine discs showed significant cell loss 3 days after matrix-assisted intradiscal MSC injection transfer into the discs from the annulus route, underlining that intervertebral disc targeting cell therapeutic approaches still suffer from unsolved problems in terms of delivery effectiveness [45].

In order to improve the efficacy of cells/hydrogel delivery for disc regeneration, an alternative approach to the annulus fibrosus route, namely the transpedicular route, has been developed and tested [2, 8, 46]. This emerging technique allows to preserve the annulus fibrosus intact, while the nucleus pulposus is reached via the endplate route. For this purpose, it is necessary to create a deep hole into the vertebra (peduncles) along the transpedicular trajectory (Figure 6).

This new alternative approach has been described and tested in human cadavers and large animal models, but is not without downsides, as bone is more difficult to penetrate and the cartilaginous endplate is damaged. However, these tissues can be more easily repaired/regenerated, in order to avoid leakage and extrusion of the selected therapeutic, than the more com-

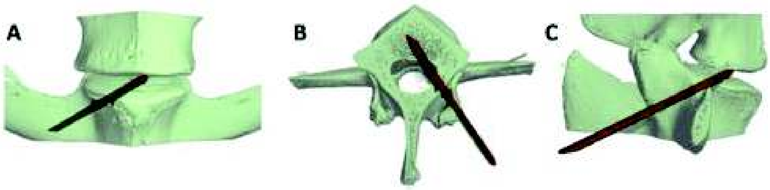

Figure 6: 3D-CT reconstructions of sheep spinal segments showing the transpedicular approach in frontal (A), coronal (B), sagittal (C) planes [2].

plex structure of the annulus fibrosus. The sealing and repairing of bone and cartilage could be obtained using a press-fit porous polyurethane scaffold to guide the regeneration [47, 48]. However, for its successful and efficient clinical application, appropriate surgical tools and techniques are required. Importantly, a less invasive and tissues damaging approach is still needed.

1.2 OBJECTIVES

In order to describe the PhD goals, and correspondingly the structure of this work, it is useful to describe the surgical procedure currently used for disc regeneration through the transpedicular approach, as reported in [8, 2], underlining: *i*) the surgical steps for reaching the intervertebral disc through the transpedicular route; *ii*) procedure-related risks and related precautions and *iii*) the surgical instruments currently used for this procedure.

Surgical procedure

The new transpedicular approach, performed by open surgery, requires that the surgeon, using a k-wire get in motion by an hand-held surgical rotative drill, creates an access to the intervertebral disc space by drilling the vertebra to obtain a deep tunnel, up to 50 mm long. In particular the tunnel toward the intervertebral disc is drilled through the pedicle. The pedicle is a thin shell of cortical bone, filled with cancellous bone, connecting the vertebral body with the posterior arch. Once the peduncle has been exposed, the surgeon begins to drill following a trajectory which has been mentally constructed. To verify the trajectory, the surgeon must interrupt several times the drilling operation, to acquire two fluoroscopic images perpendicular to each other (antero-posterior and medio lateral), that will determine whether the drilling trajectory is leading or not to the end plate. In the positive case, the surgeon can continuing the drilling operation, trying to follow the already undertaken direction. If negative, the surgeon must mentally re-plan a new drilling direction for reaching the endplate. The drilling operation is finally interrupted when the drill breaks through the endplate and reaches the intervertebral disk. The recognition of breakthrough between endplate and intervertebral disc is on the surgeon's *sensitivity*. Once the vertebra has been drilled up to the disc endplate, biological materials are delivered into the intervertebral disc by using a needle, and the bone tunnel can be filled with a sealing polymer. The risks that this procedure involves, include:

- biological damages due to high dose of radiations to which the patient and medical staff are exposed during the numerous fluoroscopic image acquisitions;
- high chance that the drill bit plunges outside the peduncle due to improper trajectory planning;
- high chance of mechanically damaging the surrounding soft tissues with the drill bit.

As mentioned before, the drilling procedure involves surgical drills and k-wires, which are the basic tools in any orthopedic surgeon's toolbox. Nevertheless during their use some intraoperative complications may occur. Drill-bit breakage, bone chips formation, damaging of surrounding soft tissues and overheating of adjacent tissues up to necrosis are not uncommon during bone drilling with rotational cutting tools [49].

Moreover it is worth to notice that the procedure is manually performed and that the surgeon dexterity and experience play an important role in maintaining the route toward the end plate of the vertebra during drilling. Another factor to keep in mind are the surgeon's tactile feedbacks during drilling that represent the only method, together with imaging, to: i) *monitor* the advancement of the drill through different bone layers, and ii) enhance the surgeon readiness in recognizing if the drill bit is damaging wrong tissues (vascular or neurologic).

Engineering challenges and PhD objectives

The surgical procedure described above clearly involves the engineering challenge of the ***accurate and safe creation of a single transpedicular bone hole to access to intervertebral disc space***.

For this purpose, keeping in mind the risks related to surgical procedure, the PhD objectives were:

- design and development of a system for guiding surgical tools for access creation to intervertebral disc space, able to decrease the exposure to ionizing radiation associated to X-ray imaging and to **improve the accuracy** of drilling task. Disc degeneration mainly occurs at L4/L5 level, whose mean anthropometric dimensions are reported in Figure 7 [3]. The access to disc, via transpedicular route, needs the creation of a tunnel in the pedicle usign a k-wire or drill bits with diameter up to $\phi = 4mm$. The angular accuracy can be estimated using a comprehensive CAD model of the vertebra and the tool for drilling (considering its maximum dimension of $4mm$) as shown in Figure 7. This evaluation allowed to estimate the maximum positional error of drill-bit equal to 5°. This underlines the need for accuracy of this procedure, and so the need for providing the surgeon with a guiding structure for insertion of the surgical tools during the transpedicular procedure. The mechanism should guide the drill towards the intervertebral disc keeping the planned trajectory, thus reducing the number of fluoroscopic images. Few fluoroscopic images are used to plan the transpedicular route thanks to a proposed *planning software*. The trajectory planning algorithm relies on the possibility of reconstructing the three-dimensional orientation of a segment using its projections on two orthogonal planes. In the case of the described surgical procedure, such projections are provided by two perpendicular fluoroscopic images of the operating site acquired through a C-arm fluoroscope. The design of the positioning system takes into account features and constrains imposed by the presence of instrumentation and medical staff in the operating room, making the whole platform low-cost and easily integrated into standard operating rooms.

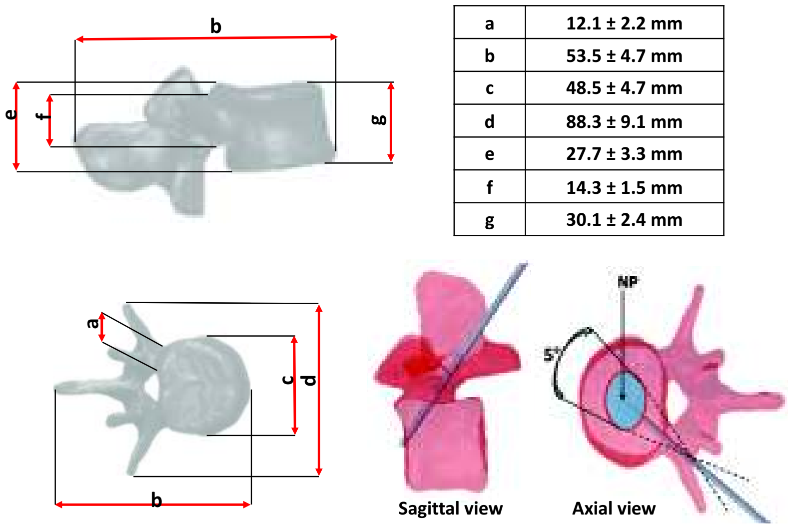

a	12.1 ± 2.2 mm
b	53.5 ± 4.7 mm
c	48.5 ± 4.7 mm
d	88.3 ± 9.1 mm
e	27.7 ± 3.3 mm
f	14.3 ± 1.5 mm
g	30.1 ± 2.4 mm

Figure 7: Mean dimensions of a lumbar vertebrae and diameter of the nucleus pulposus (NP) [3].

- design and development of a bone drilling system that enhances safety during drilling. With this aim, ultrasonic technology has been adopted. Ultrasonic drill uses high-frequency and high-energy microvibrations to selectively cut mineralized structures, leaving soft tissues undamaged, even in case of accidental contact. Ultrasonic bone cutting, minimizing possible damages to surrounding tissues, can be consider an **intrinsically safe** drilling method. Moreover, ultrasonic systems induce lighter thermal effects on the tissues than rotary drills [50]. This technology, already present on the market, however, is limited to shallow cuts. The challenge was to show that it is possible to use ultrasonic tools even for deep hole creation. Moreover, thanks to the piezoelectric transducer used for producing the high frequency mechanical vibration, the ultrasonic tool has also intrinsic sensing capability for evaluating thrust force. This feature has been exploited in a breaktrougth detection algorithm for bone layers identification. In this way the ultrasonic drill is equipped with a redundant system for drilling safety.

Table 2 shows a summary of the surgical procedure and the related technological challenges.

Table 2: Overview of the transpedicular procedure and the related technological challenges.

Surgical tasks	**Means needed for transpedicular approach**	**Risks**	**Technological challenges**
Access creation	Use of rotational drill hand-held by the surgeon for bony tunnel creation.	High risks related to accidental injuries to surrounding soft tissues	Adoption of intrinsically safe drilling technologies (such as ultrasonic drill) for deep bony tunnel
Tool advancement and tissues identification	Manual advancement of the drill bit and adjusted based on surgeon's tactile feedback and experience. Fluoroscopy guidance is necessary to assess penetration depth	Related to the readiness and sensitivity of the surgeon to recognize the bone layers breakthrough and to biological damages due to X-ray exposure	Implementation of a system for estimation and monitoring of the bone impedance for bone breakthrough detection
Tool orientation	The spatial orientation of the drill is regulated manually by the surgeon. The drilling trajectories are mentally reconstructed by the surgeon according to two perpendicular fluoroscopic images	The planning of the drilling trajectory is completely demanded to the experience of the surgeon with the high risk of a wrong route causing irreparable damage	The drilling tool must be guided and oriented by a guiding mechanism according to a planned route evaluated by a planning software based on spatial reconstruction of the objects in fluoroscopic images

1.3 THESIS OVERVIEW

The thesis has been organized as follows (see the Figure 8):

- in Chapter 2 the state of the art on minimally invasive spine surgery is presented as well as the surgical procedure pointed out in this work, namely the treatment of intervertebral disc degeneration through the transpedicular approach. The analyses of the procedure led to the definition of the requirements of a surgical platform to assist the surgeon in performing the procedure. The design of the platform is described. The kinematic architecture of the platform is reported, and finally the software planning is described.

- Chapter 3 describes the methods for safe bone drilling. Different bone machining techniques are presented, highlighting the performance of two important technologies, namely the rotative and the ultrasonic ones. Moreover, different techniques for bone layers identification are reported. The Chapter is devoted to describe the open challenges in bone drilling.

- in Chapter 4 the process designed for developing the ultrasonic drill for deep hole is presented. Different tools and strategy for ultrasonic device design are compared. The piezoelectric actuator, the resonant parts and power supply with its different control systems are described. Finally, the results of the proposed development process are discussed.

- in Chapter 5 an *average impedance* parameter is defined to identify bone layers during drilling. An algorithm of layers identification based on the variation of the average impedance over a moving position window is presented. Results from bench tests on porcine models are discussed. In addition, the average impedance results obtained on human vertebrae drilling test is presented and compared with bone mineral density evaluated from CT scans. Finally, experimental setup and results of force sensing characterization of ultrasonic drill are discussed in order to implement a new process for bone impedance evaluation.

- in Chapter 6 conclusions and final considerations are reported.

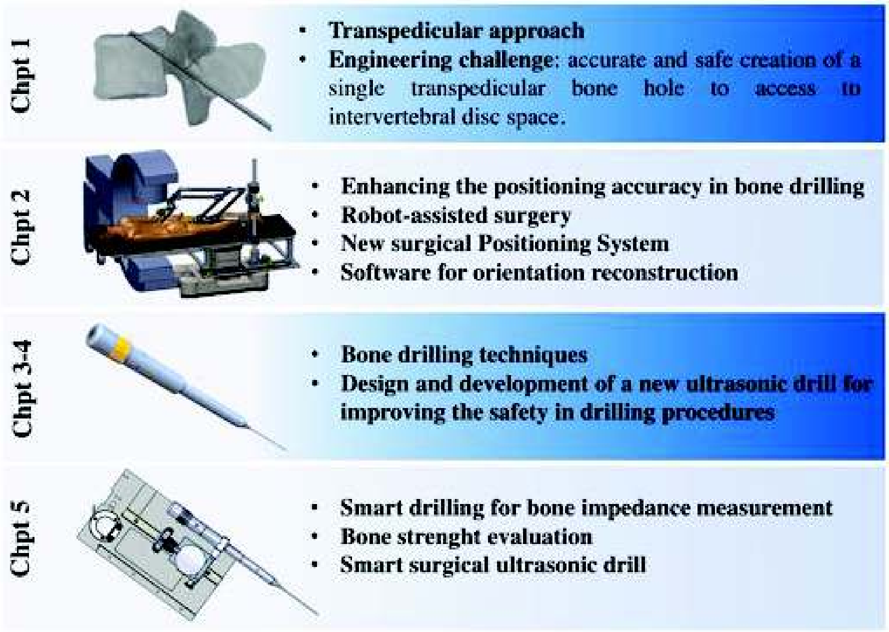

Chpt 1
- **Transpedicular approach**
- **Engineering challenge**: accurate and safe creation of a single transpedicular bone hole to access to intervertebral disc space.

Chpt 2
- **Enhancing the positioning accuracy in bone drilling**
- **Robot-assisted surgery**
- **New surgical Positioning System**
- **Software for orientation reconstruction**

Chpt 3-4
- **Bone drilling techniques**
- **Design and development of a new ultrasonic drill for improving the safety in drilling procedures**

Chpt 5
- **Smart drilling for bone impedance measurement**
- **Bone strenght evaluation**
- **Smart surgical ultrasonic drill**

Figure 8: Thesis overview.

2

POSITIONING ACCURACY IN BONE DRILLING

In common language, a well done action is often described using the sentence "*carried out with the precision of a surgeon*". Precision is one of the attributes that distinguishes a surgeon both in and outside the operating room. A challenge for orthopaedic and spine surgeons, dealing with procedures that involves anatomical sites where nervous tissues are present, is to maintain a high level of accuracy and precision during the surgery using the traditional manual tools. Enabling accurate implant placement or/and precise drilling following preoperative simulated trajectory are of paramount importance for good surgical results. However the maintaining of a high accuracy level in these precision tasks is not assured using handheld surgical tools, as drills for the creation of bony tunnel in prescribed trajectories. The accuracy of a manipulator is a measure of how close the manipulator can come to a given point within the workspace [51]. Moreover, in traditional surgery, drilling trajectories are mentally reconstructed by the surgeon starting from perpendicular X-ray images. This technique introduces high risk factors for the patient due to drilling route the inadvertently surgeons can undertake and the need of high X-ray dose. For this reason, in the last decades robotics has been adopted in surgery for improving the surgical procedures. In [52] is demonstrated that the robot in performing accurate milling of the implant cavities for hip replacement surgery is superior in terms of accuracy and motion steadiness. Many other work are dedicated to demonstrate the preeminence of robotics in performing surgical tool manipulation or bone preparation in orthopaedic surgery. In this Chapter, the state of art about the robots adopted in surgery, specifically in orthopedics, are presented. Different strategies for accuracy enhanching are discussed. At last, a new surgical platform on purpose developed for transpedicular route procedure is presented and discussed.

2.1 TECHNOLOGIES FOR SURGERY ACCURACY ENHANCING

From the second half of the 20th century the world has been revolutionized by the introduction of computers in all fields of human life [53]. This revolution has been accompanied by the progressive development of robotics in the most disparate fields, first of all the manufacturing one, speeding up the assembly line. The use of a robot in some application scenarios brings about a large list of advantages, in terms of: *i*) increasing the efficiency in the execution of a repetitive tasks; *ii*) improving accuracy [54]. For these reasons robots are used to automate or improve such industrial processes as welding and assembly [55, 56, 17]. Keeping in mind the advantages deriving from the adoption of robotic technologies, and their ability to couple complex informations to physical actions in order to perform a useful task, starting from the 1980s robotics is being increasingly used also in surgery. The first robot for surgical application was developed by NASA and Stanford Research Institute in the 1980s [57], to enhance surgical skills, and allow telesurgery. Many surgical systems have been developed to guarantee an effective surgical procedure and assistance to surgeons [58, 59]. Taylor et al. in [55] groups the advantages of surgical robotics adoption into three areas:

- the potential of a medical robot to significantly improve surgeon technical capability exploiting the complementary strengths of humans and robots;
- the potential of medical robots to promote surgical accuracy and safety to prevent both human errors and the unintentional damages to delicate structures due to surgical instruments;
- the ability of medical robots to promote consistency while capturing detailed online information for every procedure. These data can be used in statistical analyses examining many cases to develop better surgical plans.

In the last decades the advances in surgery have focused on minimizing the invasiveness of surgical procedures. Minimally invasive surgery (MIS) uses a variety of techniques to minimize the damage inflicted to the body. In general, MIS is associated with less pain, a shorter hospital stay and fewer complications.

More than 90% of interventions are now performed through minimally invasive approaches, with projected growth rates of up to 15% in the next 5–10 years [60]. Compared to thirty years ago, this represents a substantial change of paradigm allowing a number of benefits for the patients and their well-being in daily life after the surgery [61, 62, 63, 64].

Technological development, also in the robotic field, has meant that MIS was increasingly adopted by surgeons despite the potential disadvantages of this technique, such as limited operating space and field of vision, the lack of haptic feedback, loss of stereo vision and depth perception, diminished hand-eye coordination, prolonged learning curves and training periods [65, 66, 67]. Minimally invasive technologies are used in a wide range of surgical procedures including enduvascular surgery, general surgery, neurosurgery and orthopedic surgery. As widely reported in the review of Snyder et al. [68], as the early 1900s the first minimally invasive techniques for spine surgery were implemented. Only in 1991 the first discectomy operation using laparoscopic techniques was performed [69]. These studies have paved the way for the systematic introduction of robotic technologies for the surgical treatment of orthopedic pathologies. Surgical robotic platforms are employed to treat a wide variety of orthopedic disorders and to deal with different procedures, such as minimally-invasive and percutaneous repair, e.g. for spinal fractures, spine fusion or joint replacement. Robot-assisted Minimally Invasive Spine Surgery (MISS) has the potential of improving outcomes thanks to the increased accuracy in the preparation of bone surfaces, increased reliability and reproducibility of results, better spatial precision, shorter exposure times to radiation [70, 71, 72, 73]. Robots appear to be ideal surgical assistants in spinal surgery due to their inherent characteristics: the ability to perform tasks repeatedly without fatigue or loss in accuracy, the ability to lessen or eliminate hand tremors and the ability to accurately guide the surgeon to the target with high precision. In order to improve safety and accuracy of MISS, since several years the combined use of surgical robotics and navigation system technologies has been adopted.

Robot assisted surgery is a technique that involves the combined use of robot and medical imaging data processing. Robot for assisted surgery can be grouped, as proposed by Korb et al. in [4], into two categories:

- the first group includes telesurgical systems, which dependent from interactive communication with the surgeon during the whole surgical procedure, and are not preprogrammed using preoperative medical images. Telemanipulators rely on intraoperative images, which are often given by endoscopes, but can also be given by intraoperative CT or MR imaging devices (Figure 9).

- The other group encompasses preprogrammed surgical robots. Preprogrammed robots are normally guided by the use of preoperative images and execute a preoperatively defined trajectory. The plan is established before the intervention and normally will not be changed. The surgeon supervises the execution of the planned trajectory by the robot. Such systems are well-suited for interventions, in which bones are drilled or cut, because they are rigid, and the preoperative images are still valid intraoperatively, for example, in orthopaedic or maxillofacial surgeries (Figure 10).

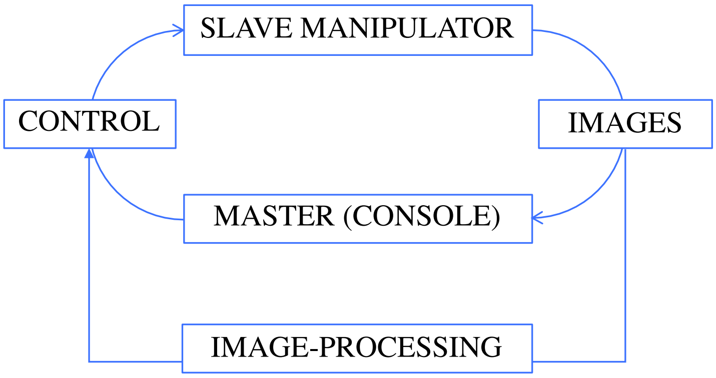

Figure 9: Workflow of a surgical operation with a telemanipulator. Adapted from [4].

Preprogrammed surgical robots allow a reduction of biological damages due to X-ray exposure, repeatedly used in standard procedures, thanks to the combined use of a pre-operative planning using Surgical Navigation Systems (SNSs). A SNS attempts to localize or determine the position of surgical tools in order to guide them toward specific targets, providing on a display the spatial information about surgical tools or implants position with respect to the target [74, 75, 5]. SNSs comprise: a stereoscopic camera emitting infrared light, reflective markers, the navigation software and a computer platform with screen

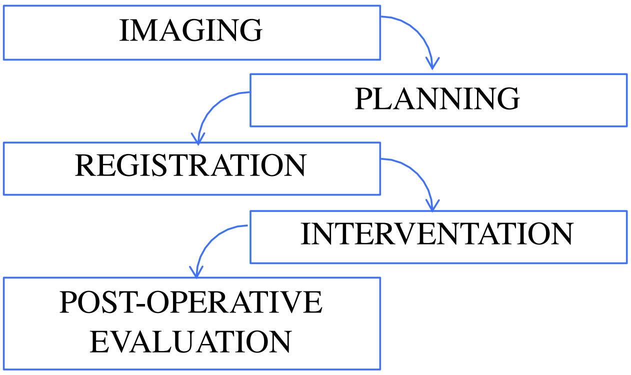

Figure 10: Workflow of a surgical operation with a surgical robot. Adapted from [4, 5].

in which the 3D reconstruction of patient anatomy and tool position are displayed. Navigation procedure usually involves the following steps [18, 76, 77, 78]:

- **image data acquisition and processing**. Generally, images from Computed Tomography (CT) or Magnetic Resonance Imaging (MRI) are used for the creation of patient specific models.
- **Matching** involving registration of patient's anatomy with the preoperative medical image with the intraoperative images, in which external markers on patient's body before gathering the image data are used.
- **Referencing** of the markers identified during matching as reference markers during surgery, for avoiding mismatching due to surgeon's actions or patient's breathing.
- **Tool tracking** in order to visualize in real-time the procedures, it is necessary to track the location and orientation of the tools. Navigation technologies commonly include sensors to track the position of both the anatomical target and the surgical tool. Optoelectronic systems, for example, are composed of Charge-Coupled Device cameras to record the relative position between an anatomical site and surgical tools, which are marked through LED or reflective markers/objects.
- **Tool visualization** in static or dynamic image formed with the help of image data from bone and instrument trackers.

A different and cheaper navigation method is based on fluoroscopy. It allows the construction of an intra-operative map following the stereotactic surgery principles [79]. In orthopaedic procedures, a C-arm fluoroscope is commonly used and the images are acquired while a support with markers (such as LEDs) is attached to the image intensifier of the C-arm and to the target bones or to the surgical tools. In this way it is possible to univocally determine their relative positions and to plan the insertion of surgical tools. Furthermore, a 3D view can be reconstructed from multiple isocentered C-arm images. However, these techniques also involve the use of optoelectronic systems and the patient normally receives a high dose of X-rays due to the long exposure time[80].

The only use of SNS is not sufficient to guarantee the accuracy level needed for surgical procedures, especially when the spine is involved. In fact the surgeon does not just need trajectory planning toward the target; rather she/he needs that the surgical tool is precisely positioned according to the plan, avoiding the inaccuracy of hand-controlled positioning of surgical tools. Robot systems for surgery are sub-classified into [74, 81]:

- *passive systems* that do not perform any actions on patients; rather, they assist surgeons during preoperative planning, surgical simulation, or intraoperative guidance. The energy needed for moving the surgical tool is provided by the surgeon. The robot is locked into predefined position and it is used as a holder that fixes the orientation of the surgical tool to facilitate the advancement toward the preoperatively defined target. An example of passive system is Viewing Wand (ISG Technologies) that comprises FARO, an articulated six-degree of freedom surgical arm with manually guided probe [82, 83, 6] (Figure 11). The probe position with respect to the skull is used for registration or navigation. To keep stability of positioning, the arm is equipped with brakes.

- *Semiactive systems* perform some actions, such as moving a drill guide sleeve, but they do not perform surgical actions. Generally, semiactive systems are employed for simple tasks, such as needle insertion with linear motion, osteotomy with planar motion or laparoscopy with conical motion. An example is represented by NeuroMate, a stereotaxic targeting device for neurosurgery (first neurosurgical robot to get FDA clearance) [84, 85]. At the beginning of surgical procedure the robot holds a calibration cage and X-ray imaging is used to register the patient's coordinate system to the robot (5 degree of freedom); then the robot is controlled according to the preoperative plan. When the robot reaches the position, the neurosurgeon can insert the tool through the robot's guiding channel [85, 86, 87].

- *Active systems* are powered robots that actively interact with the patient under the supervision of the surgeon, who monitors the procedure and intervenes as needed. In this case it is of paramount importance to take into consideration safety issues introducing redundancy in kinematics and sensors, going to the detriment though hardware and software complexity and more costly design [88, 89].

Figure 11: FARO (FARO Medical Technologies, Orlando, FL) surgical arm adopted in Viewing Wand (I.S.G. Technologies, Mississauga, Ontario, Canada) system [6].

Among the first active systems developed for orthopedic surgery there is ROBODOC (Integrated Surgical Systems, Davis, CA, USA) and CASPAR (URS Ortho GmbH, Rastatt, Germany), that perform some surgical actions preoperatively programmed. Their workflow is similar to that of CAD/CAM system, in addition including an intraoperatively match of preoperative images and planning of the intervention [90]. The ROBODOC system performed the milling automatically based on the surgical

Figure 12: The NeuroMate^{TM}robot system (Integrated Surgical Systems, Davis, CA).

Figure 13: ROBODOC (Integrated Surgical Systems, Davis, CA, USA).

plan, and it has been used in many types of orthopedic surgical procedures including: total hip arthroplasty, femur preparation, acetabular cup replacement, knee surgery and spine surgery. It has received a CE mark (1996), and FDA clearance for total hip replacement (1998) and total knee replacement (2009) [91]. The robot is instrumented with six-axis force sensor at the wrist. The force sensing is used for safety monitoring, to allow the surgeon to manually direct the robot arm and to vary the velocity of tool motion as a function of the forces experienced during milling [92, 93]. The tip of the robot carries a high-speed rotary cutter which can accurately bore a femoral cavity for hip implant. ROBODOC works with a pre-operative planner called ORTHODOC, which allows a computer model of the appropriate size and shape of implant to be positioned over a three-dimensional model of the hip, reconstructed from a series of CT scans. The position and orientation of the implant can be adjusted until the surgeon is satisfied [74, 92, 94, 95]. A direct competitor to ROBODOC was CASPAR system, no longer for sale, that was designed for automatically bone drilling from a preoperative plan based on CT data [96, 97].

Another system is RIO robotic arm (MAKO Surgical Corporation, Ft. Lauderdale, FL, USA), that received FDA clearance in 2008. The RIO is used for knee arthroplasty or patellofemoral arthroplasty [91, 98]. The RIO arm and the surgeon simultaneously hold the surgical tool, with which the surgeon drills the surgical site (Figure 14). The arm is backdrivable with low friction and low inertia, so that the surgeon can easily move the tool. The arm resists motions outside of the planned cutting envelope by pushing back on the surgeon's hand. RIO does not require the bone to be fixed to itself, relying on a camera system to track bone and tools intraoperatively [99, 100, 101].

While navigation and robotic system have been well accepted in surgery, with widespread use in urology and general surgery, robotics in spinal surgery remains a relatively new development [73]. In the years that followed, other surgical robots were developed to assist orthopedic surgeons. In particular, as it regards the spine surgery, a miniaturized robot for pedicle screw placement, namely the Spine Assist (Mazor Surgical Technologies, Caesarea, Israel), has been developed and approved by FDA [102, 103] (Figure 15). The SpineAssist is a bone-mounted semiactive robot designed with the purpose of assisting the surgeon in spinal fusion procedures or fracture repairs, guiding percutaneously, with 6 Degree of Freedom (DoF), the insertion of pedicles screws [104]. The bone mounting feature ensures that the robot compensates in agreement with breath-induced and other patient's motions, to the detriment of the procedure invasiveness. In fact the robot is mounted on the adjacent healthy vertebras. The SpineAssist uses an image-based mechanical guidance technique: a workstation takes care of matching the preoperative CT scans with intraoperative fluo-

Figure 14: RIO by MAKO Surgical Corporation (Ft Lauderdale, FL, USA)

roscopic images for trajectory planning, kinematic calculations, and robot control [105, 106]. Moreover, the software allows optimization of length, diameter, positioning, and trajectories of the implants. The surgical procedure starts with anchoring the mounting platform with k-wire to spinous processes. Then, a fiducial array is placed to the mounting platform. Two fluoroscopies are taken in anteroposterior plane and 60° oblique to the lateral plane. In this way the workstation computes the matching and registration of the pre- and intra-operative images. After planning, the fiducial array is removed and robot is anchored on mounting platform. The robot is employed in accordance with the surgical plan to provide the trajectory and the entry point for the instrumentation and a metal arm holds the drill guide. In this way the surgeon can safely drill all the vertebras moving the robot along the mounting rail.

Figure 15: Mazor SpineAssist (Mazor Surgical Technologies, Caesarea, Israel).

SpineAssist was used in more than 25 medical centers between 2005 and 2011 on more than 2000 patients, showing its benefits including the reduction of the duration of fluoroscopic exposure, better accuracy due to computerized assisted planning and navigation, avoidance of human caused complications and less trauma for the patient [107, 108]. Disadvantages of the SpineAssist include a longer duration of the procedure and the operational cost is higher, requiring a good trained medical staff. The same company in 2011 introduced Renaissance Robotic System, the second-generation of SpineAssist. Renaissance obtained FDA clearance (2011) and CE mark for spinal surgery, and a CE mark for brain procedures [109]. Renaissance Robotic system has dimensions and weight smaller respect to the previous one, moreover the system was designed with better ergonomic structure and the sensitivity of positioning was enhanced. Moreover, Renaissance includes an add-on for existing fluoroscopy C-arms that provides 3D images for intraoperative verification of implant placement [110].

The use of Renaissance needs the following steps [111]:

- *preoperative planning*. CT images, with 0.4 - 1 mm cross-section interval, are loaded into the software. The software converts CT images into 3D imaging. Once the surgeon determines the vertebral segments for surgical intervention, she/he may select the localization, diameter and length of instruments and the type of the intervention and the planning data are loaded to the robot in the operating room.

- *Registration of clamp position*. Preoperative planning information is matched with preoperative x-ray images. This process can be performed using a disposable 3D marker kit placed onto the clamp where anterior and posterior images and oblique x-ray images are taken.

- *Robot assembly and motion*. The robot can be stabilized on a suitable platform with the aid of a clamp. After the correct coordinates are received by the robot, gaits for a reliable trajectory are reported and in which the surgeon can insert the appropriate cannula and K-wires onto the appropriate trajectory.

- *Manual application* of pedicle screws that can manually be tightened.

Starting from 2016 Mazor Robotics has introduced a new product for spinal and brain surgery, the Mazor X$^{\text{TM}}$(Figure 16). The Mazor X$^{\text{TM}}$robotic guidance system allows pre-operative or intra-operative planning and robotic-guided execution of multiple trajectories. The new system is a bed-mounted robotic guidance system that leaves the workstation away from the operating table to minimize the risk of crowding during the procedure. In order to assure greater predictability and precision, Mazor X$^{\text{TM}}$includes three integrated processes: *i*) planning, *ii*) guidance and *iii*) verification. It is composed by a workstation and 6 dof articulated arm with an overall accuracy of 1.5 mm. Also the last version of Mazor robots maintains a secure rigid patient fixation.

Despite of the several advantages, different authors state that uses and efficacy of surgical robotics have not been well established yet: long-term follow up studies still have not been conducted able to enable surgical robotics to become the best standard for orthopaedic procedures [17]. Among the main obstacles it is possible to mention the high costs and the need of setting up a dedicated operating room coordinating robot system with imaging [112]. Other issues associated with the use of surgical robotis regard the considerable amount of time and associated costs required to train the surgical team, as well as

Figure 16: Mazor X^{TM}(Mazor Surgical Technologies, Caesarea, Israel).

the increased time for both preoperative planning and intraoperative use [104, 112, 113, 114]. Moreover, contradictory results on reduction of radiation exposure are reported [113, 115, 116]. Patient anatomy needs to be immobilized by fixing it to the operating room table, and the patient movements need to be compensated for by tracking it in real time and adjusting the fixed robot position accordingly, increasing the complexity of the robot's registration to the target anatomy [117]. Kim VB et al in [118] identify potential disadvantages in lack of compatible instruments and equipment with robots end-effector. On the other hand, as Joseph et al. describe in [119], robotics in spine surgery is in its infancy, and it is still necessary to identify the ideal role for robots among spinal instrumentation.

The way to gain the acceptance and consequently the adoption of technologies to support the surgeon could be to design simple and cheap robotic arms able to actively involve surgeons in the surgical workflows. For this reason, the design of the robot and its functionality must maximize the strengths of the human operator in term of efficacy and accuracy on the performed procedure (Table 3). The goal of surgical robotics is not to replace the surgeon, rather to provide to her/him with a new set of very versatile tools that extend her/his ability. Moreover, keeping in mind the will of the surgeons of maintaining control over the surgical procedure, the assisting robot must be designed considering the specific tasks to delegate to it. This consideration is necessary in order to decrease kinematics and control strategy complexity of the system and to design task-

Table 3: Differences between surgeons and robots. Adapted from [17].

	Surgeons	**Robots**
Strengths	Dexterous Flexible and adaptable Able to use qualitative information Good judgment Rudimentary haptic abilities Can integrate extensive and diverse information	High geometric accuracy Stable and untiring Repeatability Can be equipped with different sensors
Limitation	Prone to tremor and fatigue Limited geometric accuracy Limited ability to use quantitative information	No judgement Unable to use qualitative information Expensive More studies needed

specific robot. For example robots for percutaneous needle insertion need only three degrees of freedom: 2 DoF to orient a needle about an entry point and 1 DoF to control insertion depth. For this guidance applications, passive arms with joints embedded encoders are often sufficient for low-risk maneuvers, simple and precise tasks [120, 121, 122, 123].

2.1.1 Design principles of surgical robots

The design of a surgical robot must take into account some constraints that cannot be ignored in relation to the use that will be made of it. Unlike the industrial robots, which work isolated from the users by preventing machine workspace from human intrusion, surgical robots cooperate with the surgeon, medical staff and interact the patient. For this reasons, the influence of human factor and specific clinical constraints in design process must be considered. Moreover, the required functionalities are defined according to different surgical operations, that imply the surgical robot must be designed for specific operations on targeted anatomy.

In particular, it is worth noticing that during the use of a surgical robot:

- the working conditions change with each patient, e.g. due to different characteristics of soft tissues, position of the patient on the operating table, size of the body and accessibility of the organs;
- "trial/error" nor "doing again" movements of the robot must be excluded;
- it is necessary a pre-operative study of the intervention;

- planned operations could request a modification during the operation according to the experience and judgment ability of the surgeon;

- the position with respect to the patient varies between two operations and the environment is usually unstructured: operating rooms are cluttered with several other medical systems (radiology, anesthesia, surgery, etc.);

- a limited workspace is preferred in order to prevent hazardous collisions between its moving parts and the medical staff or the patient;

- a fixed operating point for protection against unexpected motion of surgical tools should be settled.

It should be emphasized, that surgeons are not engineers with technical experience in robotics (dedicated user-friendly human-machine interface must be introduced to facilitate the use of the robot and its features) but their contribute is fundamental in design process especially in requirement analysis.

Generally, as Kuo et al. highlight in [124], the kinematic design is the predominant phase in the design of robotic manipulators for minimally invasive surgery. In this phase safety, accuracy, ergonomics, and dexterity issues must be taken into account and transformed into technical specification, (e.g. the mechanism topology, workspace) to satisfy the surgical requirements. Usually in minimally invasive surgery, surgical instrument are manipulated with a 4 DoF pivoting motion including three rotational DoFs and onte translational DoF (Figure 17) [125, 126]. In [124], Kuo defines three different kinematic design requirements in order to manipulate surgical instrument with robotic manipulator:

- the end-effector must allow 4 DoF (three rotational DoFs and onte translational DoF);

- the axes of three revolute DoF should intersect at some point which should locate some distance away from the manipulator;

- the translational DoF should move along a fixed direction respect to the end-effector (along which the surgical instrument is being inserted and retracted).

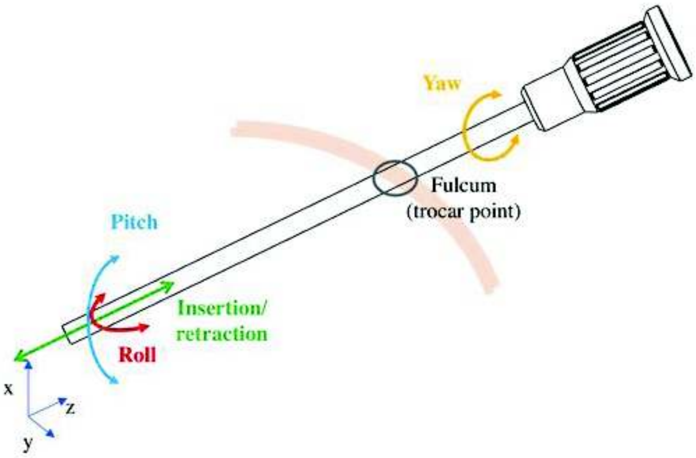

Figure 17: The four degrees of freedom of motion for an MIS instrument, adapted from [7].

These requirements can be met choosing different robotic architectures, in particular three basic architectures are available: *i*) serial architecture, *ii*) parallel architecture and *iii*) hybrid architecture. Each architecture is characterized by the type of kinematic chain connecting the end-effector to the base link, and specifically (Figure 18):

- **serial architecture** is the classic anthropomorphic manipulator composed by a single open loop kinematic chain, where adjacent links are interconnected by a revolute joint. It is characterized by a large work space and high dexterity. The most important disadvantage is the low precision that results from cumulative joint errors and deflection of the links. High inertia, due to high number of series moving parts, affects the performance too [51, 127].

- **parallel architecture** is composed by two or more close loop kinematic chains, where the end-effector is connected to the base link by at least two different and independent kinematic chains. The limits of the parallel manipulators are the small work space and low dexterity respect to the serial ones. However, there are numerous advantages allowing the adoption of this kind of architecture for surgical robots. The parallel architecture provides high pay-load: the load on end-effector is shared by different kinematic chains, offering high rigidity to the structure. The joint errors are not added up, rather are shared by joints: it affords high accuracy to the manipulator [51, 127, 128, 129, 130, 131].

- **hybrid architecture** is the combination of the serial and parallel architectures. Generally, the hybrid architecture is composed by open and closed kinematic chains.

The most compliant architecture with the fundamental requirements for surgical robot is the parallel architecture. The compactness and lightness of parallel architectures simplify the relocation of the robot in the operating room and save necessary space. The relatively small work volume of the parallel robots, if correctly designed, can introduce an important safety feature. In addition, parallel robots behave safely near singularity. The parallel robots provide accuracy with lower price when compared to similar serial robots with the same accuracy level. These high levels of accuracy are important for spine surgery [127].

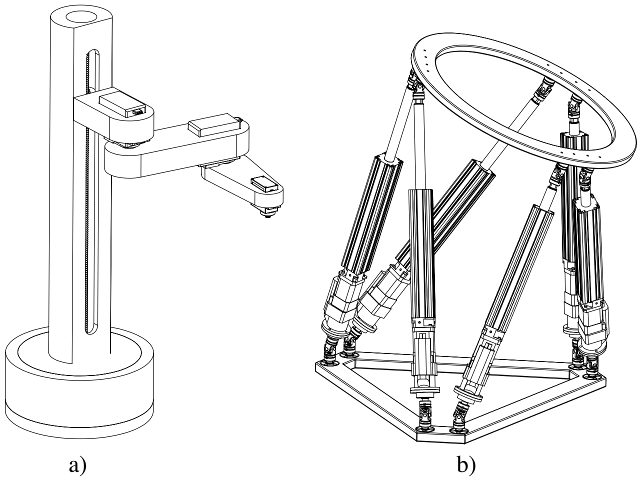

Figure 18: a) Scara robot, example of serial robot; b) Stewart platform, example of parallel architecture.

2.1.2 Remote center of motion

As described, surgical robot has to manipulate surgical tools working with large angular mobility about a single point or within a limited small spatial volume. In particular the surgical tools is pivoted around a single point. In laparoscopic a "fulcrum effect" at patient's abdominal wall is desired. The surgical tool has only four DOFs (three rotations and depth of penetration) centered at the entry point and very constrained lateral motions are acceptable. Moreover, the extracorporeal workspace volume must guarantee that the robotic manipulator does not collide with patient during surgery. For those reasons, in minimally invasive surgery robots with appropriate kinematic architecture, that allow a fixed rotational center located some distance away from the structure and patient, are often adopted. These manipulators are designed taking into account the concept of remote center-of-motion (RCM) and they can decouple rotational and translational motion of tools. Kuo in [7] describes the RCM as "geometrically a point at which one or more rotational motions are centered and these motion are under remote-control by the mechanism". The adoption of RCM robot decreases the risk of injury during surgery not allowing lateral motions of instrumentations [132]. Many mechanical solutions including RCM with different DoFs and designs have been proposed in [133, 134, 135, 136].

2.2 A NEW SURGICAL POSITIONING SYSTEM

Referring to surgical procedures described in Section 1.2, a new *passive* Surgical Positioning System (SPS) for guiding orthopedic drill during transpedicular approach and supporting spine surgeons in MISS has been developed. The choice to design a passive system arises from the fact that orthopaedic or neural surgeons may prefer an assisting device rather than a substituting one in performing surgical procedures, as shown in [105]. Passive systems preserve the skills of the surgeon, who remains the only supervisor of the surgical tool advancement along a drilling path. The introduction of SPS allows a mitigation of tremor during the orientation of surgical drill enhancing the accuracy of drilling trajectory.

It is worth noting that such approach would complement the haptic feedback on which the surgeon usually relies on handheld manual drillings. The proposed SPS is conceived to be integrated in a surgical platform capable of assisting the surgeon in the transpedicular procedure to treat degenerative intervertebral disc diseases (refer to Chapter 1). This procedure entails an access to the intervertebral space through a transpedicular route and can be performed percutaneously, overcoming the disadvantages of open surgery. To this aim it is necessary to orient a cannula to guide the bone (vertebra) drill along a planned route, for creating the access to the intervertebral disc through the vertebral pedicle. The designed system includes a software for the identification of the target cannula orientation, starting from the desired insertion point, and from the pre-planned insertion direction, and a mechanical support handling the cannula and orienting it as required. Starting from two perpendicular fluoroscopic images, the software can assist the surgeon to plan a safe route to reach the intervertebral space. Thus, the software developed for the transpedicular route planning aims to reduce the number of fluoroscopic images, decreasing the absorbed radiation dose. Furthermore, the SPS simplifies the cannula insertion procedure: route planning does not require the use of an additional optoelectronic system, but it is only based on fluoroscopic images captured with a C-arm fluoroscope. In addition, the SPS is designed to be easily integrated with the surgical instruments commonly available in the operating room.

2.2.1 Requirements

As mentioned in Chapter 1, the novel transpedicular approach for intervertebral disc regeneration foresees that the nucleus polposus is accessed via the pedicles without disruption to the AF. Figure 19 shows two fluoroscopic images where the needle for intervertebral disc inspection is highlighted in red. Nowadays this task is performed manually by the surgeon. The proper positioning of the k-wire is verified by acquiring several antero-posterior and medio-lateral fluoroscopic images taken during drilling, thus exposing the patient to a high dose of radiations. Once the vertebra has been drilled up to the disc endplate, biological materials are delivered into the IVD using a needle. The surgeon establishes an access to the IVD by drilling the bone of the vertebra with a k-wire.

To introduce the new transpedicular procedure in clinical practice it is necessary to develop a SPS coping with some constraints:

- *i)* The surgical procedure should be performed percutaneously rather than through an open surgery. So far it has been tested only on cadavers and large animals in open surgery but, through the design of an appropriate SPS compensating for the lack of sight on the operating field, it could be performed also percutaneously. Moreover, it is crucial to have a tool able to support the surgeon in the planning of the optimal insertion direction of the drill without the need for several fluoroscopic images.

- *ii)* The SPS should be compatible with the space available in the operating area and with the equipment used during surgery, such as the C-arm fluoroscope. In particular, it should not hamper the 90° rotation of the C-arm to switch between the antero-posterior and the medio-lateral acquisitions, as shown in Fig. 20.

- *iii)* The SPS should not hinder the actions of the involved medical operators. It should be anchored to a single side of the operating table, e.g. to its lateral bars, and in particular to the one opposite to the medical staff.

- *iv)* The SPS should include a Mechanical Positioning Device (MPD) supporting and orienting the surgical tools with passive joints to be manually regulated by the surgeon and to be subsequently locked in a specific configuration. Moreover, the MPD should include *i)* two rotary DoFs to regulate the orientation in the axial and sagittal planes, *ii)* three linear DoFs for its gross positioning before the fine orientation and *iii)* a Remote Center of Motion (RCM) to avoid damaging soft tissues during the orientation adjustment.

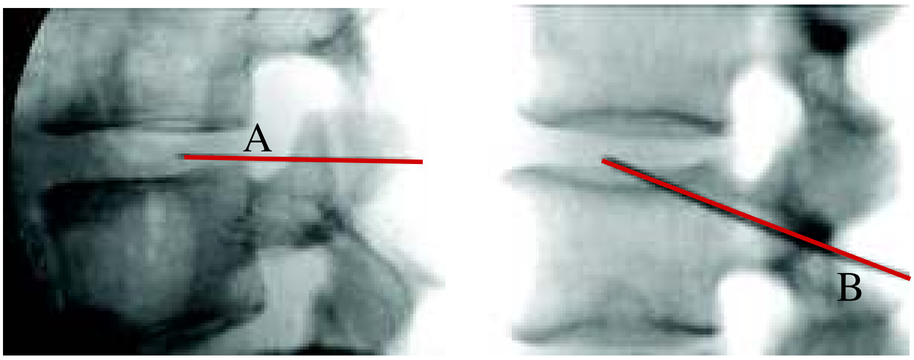

(a) (b)

Figure 19: Medio-lateral view of two approaches to the IVD. The cannula is represented in red. Traditional approach via the AF 19a;New approach through the pedicle 19b proposed in [8].

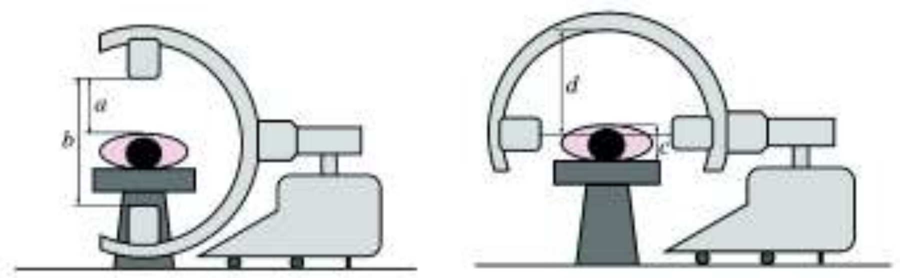

(a) (b)

Figure 20: Schematic representation of the fluoroscopic images acquisition through the C-arm. 20a Acquisition of the antero-posterior image; 20b Acquisition of the medio-lateral image. The reported dimensions are: $a = 390$ mm, $b = 780$ mm, $c = 300$ mm, $d = 700$ mm.

2.3 DESIGN OF THE POSITIONING SYSTEM

2.3.1 Insertion procedure

As described in Sec. 2.2.1, the new transpedicular procedure for the delivery of regenerative materials in the intervertebral disc requires in the creation of an access to the disc through a vertebral pedicle. Such access is obtained by drilling the bone tissue, starting from an insertion point located on the vertebral pedicle up to the disc endplate. It is crucial to properly plan the drilling path to avoid intercepting neural structures such as nerve roots and to minimize the number of acquired fluoroscopic images possibly needed to monitor the cannula advancement, e.g. through position sensors.

The transpedicular procedure has been tested in traditional open surgery conditions [8, 2]. In this thesis it is proposed a new SPS that will allow to perform transpedicular procedure in a minimally invasive way, i.e. based on a single percutaneous access. The SPS consists of two components: *i)* a MPD that holds a cannulated guide through which the surgeon can insert different surgical tools (e.g. the driller to reach the disc endplate); *ii)* a software with a Graphic User Interface (GUI) that allows the surgeon to define the desired cannula orientation (directed from the insertion point to the endplate) and that calculates the configuration of the MPD needed to orient the cannula as required. More specifically, as shown in Fig. 21, the insertion procedure comprises the following steps:

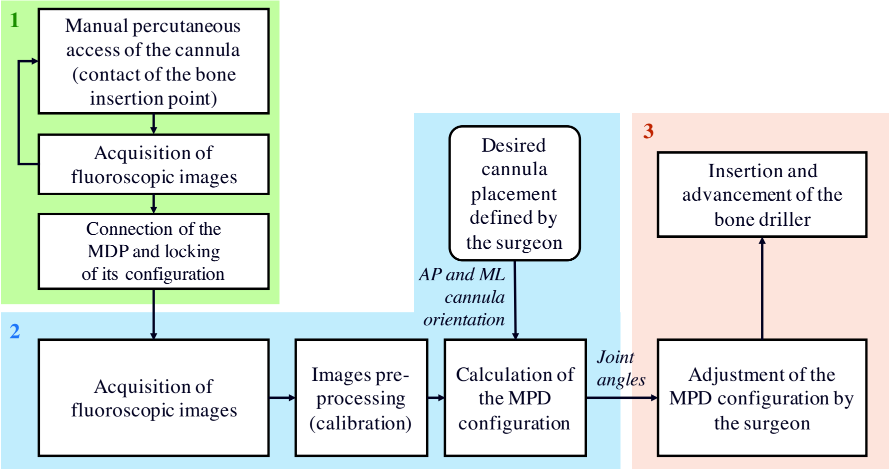

Figure 21: Block scheme of the surgical procedure steps. 1. Percutaneous access of the cannula; 2. Orientation planning; 3. Adjustment of the MPD.

1. *Percutaneous access of the cannula.* The surgeon inserts percutaneously a cannula into the soft tissues of the back in caudocranial direction until its tip touches the vertebra. This action is performed manually and the actual position of the cannula is identified by acquiring two perpendicular (antero-posterior and medio-lateral) fluoroscopic images to check if the insertion point on the vertebra is correctly located on the pedicle. The process possibly needs to be iterated until the cannula tip is properly placed. Finally, the MPD is connected to the cannula and its joints are locked to fix its configuration.

2. *Orientation planning.* Two fluoroscopic images in antero posterior and medio lateral projections are acquired again, as shown in Fig. 22 (to check that the fixation of the MPD do not alter the position of the cannula tip). The planning software pre-processes these two images to compensate for a possible offset between them. This offset could be present if the base of the C-arm is accidentally translated by the operators between the two acquisitions. The surgeon, starting from the insertion point (cannula tip on the vertebra), draws a desired path to the endplate on the two fluoroscopic images. The software derives the desired spatial orientation of the cannula and returns the joint angles

needed to set the configuration of the MPD so that the cannula insertion direction is the one desired (details will be reported in Sec. 2.3.3).

3. *Adjustment of the MPD.* The adjustment of joint angles of the MPD, and hence of its configuration, is manually performed by the surgeon. She/he can then insert the driller within the guiding cannula to start the drilling of the bone.

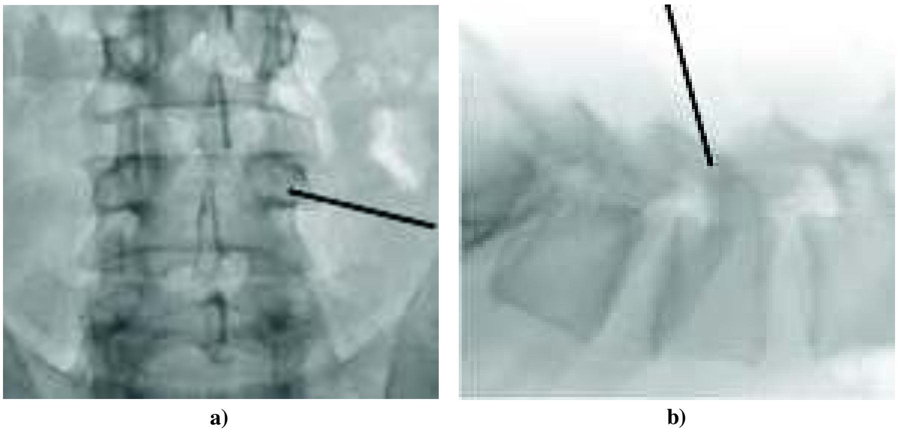

Figure 22: Fluoroscopic images and cannula desired placement (black line). a) Antero-posterior view; b) Medio-lateral view.

At the end of the described process the surgeon can occasionally stop the drilling to acquire additional images and check that the pre-planned advancement direction is actually the safest one to reach the endplate without damages to neural structures. If needed, the driller and the cannula can be extracted and a new insertion can be performed by restarting the whole procedure as described above.

2.3.2 Kinematic structure of the mechanical positioning device

The hardware part of the SPS is the MPD, whose kinematic structure (Figure 23) includes:

- A linear 3-DoFs Cartesian stage that can be anchored to the lateral bars of the operating table (prismatic joints are indicated with d_i, $i = 1, \ldots, 3$) for the initial rough positioning of the tool before the subsequent fine orientation adjustment.

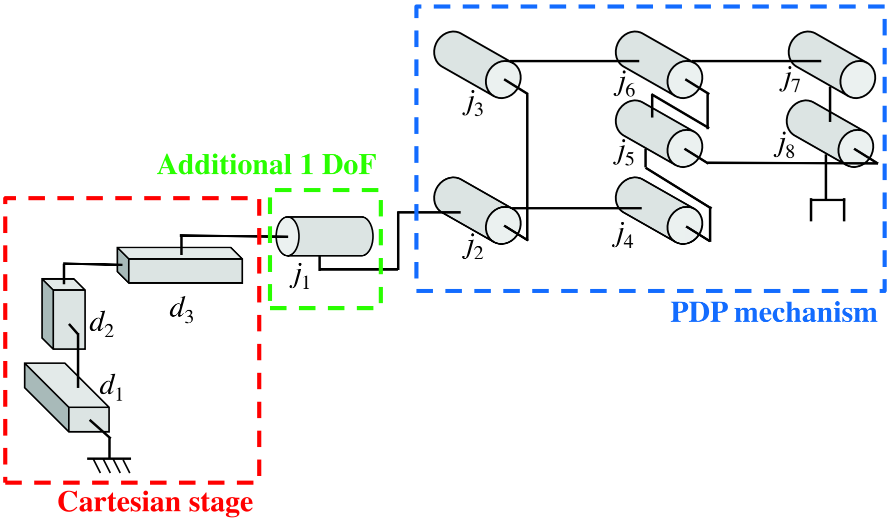

Figure 23: Kinematic structure of the proposed 5-DoFs MPD. Rotary joints j_i $(i = 2, \ldots, 8)$ implement a planar double parallelogram (see also Figure 24) for the orientation of the cannula in the sagittal plane while joint j_1 is added to regulate the orientation in the axial plane. Prismatic joints d_i $(i = 1, \ldots, 3)$ are added for the initial rough position regulation of the tool before the final fine orientation adjustment. The ground indicates the operating table on which the positioning system is connected.

- A Planar Double Parallelogram (PDP) mechanism with 1-DoF RCM, as further detailed in Figure 24, that orients the cannula around two rotation axes thanks to an additional rotary joint j_1. In this way, two independent rotational motions for the PDP mechanism can be produced: one is caused by joint rotation j_2 of an angle θ_2 in PDP plane, and the other one is obtained through the rotation of the PDP mechanism of an angle θ_1 around the link a_1 axis, thanks to the joint j_1. The global reference frame and the reference anatomical planes are shown in Figure 28. The PDP plane is parallel to the the axial plane, and its inclination is varied by θ_1. This inclination can be directly read on a sagittal section, where the a_6 projection forms an angle β with the y axis. For fixed values of θ_1 and θ_2 it is possible to define the angle α between the cannula (link a_6) and the x axis.

The dimensions of the links are chosen taking into account the workspace of the fluoroscope and the human size as reported in Section. 2.2.1. In particular, length l_3 is equal to

Table 4: Dimension of link l_1, l_2 and l_3.

Link	**Length (mm)**
l_1	45
l_2	184
l_3	155

the average width of the human torso. Link dimensions are reported in Table 4.

The whole system formed by the Cartesian stage and the PDP mechanism is positioned on one side of the operating table allowing a positional and orientational task with 5 DoFs (Figure 26).

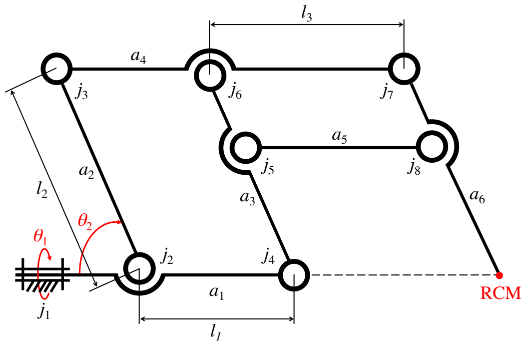

Figure 24: Kinematic representation of the PDP mechanism and additional rotary joint j_1 used to orient the cannula in the sagittal plane (angle β) and in the axial plane (angle α). The joint responsible for the first regulation is j_1 (angle θ_1) while the one responsible for the second regulation is j_2 (angle θ_2). The links l_1, l_2 and l_3 were dimensioned to comply with the spatial constrained imposed by the C-arm as represented in Fig. 20. The link a_6 represents the direction of the cannula.

The developed SPS is shown in Figure 26. As shown in Figure 23 the SPS comprises two sub-modules. A third module can be considered when a linear guide is attached to the end-effector in which the surgical drill can slide pushed by the surgeon. The kinematic parameters can be adjusted by the surgeon using five knobs, that correspond to 5dof of the SPS. The driving joints (d_1, d_2, d_3, j_1 and j_2) are irreversible (non-backdriveable) and are actuated by the surgeon through

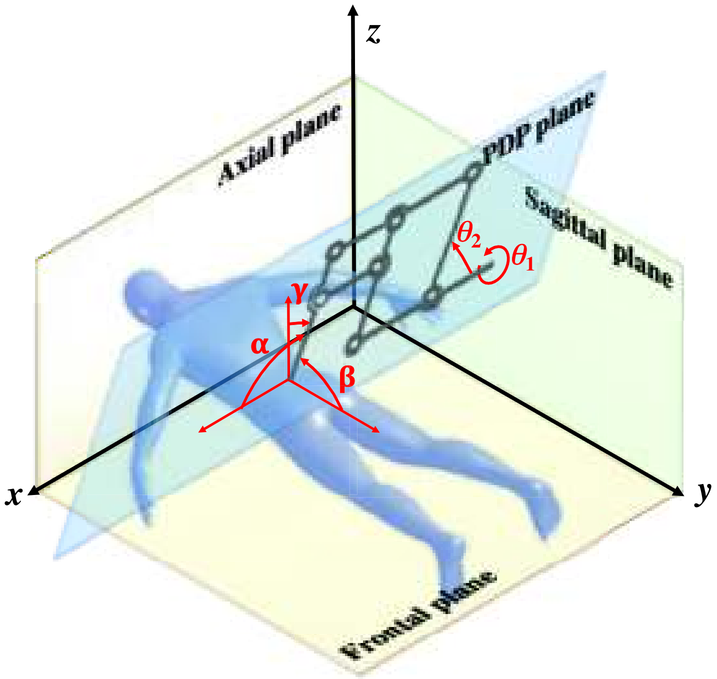

Figure 25: Reference anatomical planes and cannula orientation angles, α, β and γ, with respect to the global reference frame. The angles θ_1 and θ_2 represent the joint angles of the MPD.

Table 5: The specifications of SPS.

Payload	up to 20 Kg
Useful workspace [mm]	755x600x331
Mass [Kg]	64,7
Material	Al EN AW 6060; Steel EN 1.4404; Carbon Fibre
Number of dof	5

knobs. The knobs are connected with a worm gear. The torque C, impressed to the worm by the surgeon, is transformed in direction and module according with the worm drive reduction ratio. The whole system is developed using three different materials: joints are made of alluminium EN AW 6060 and stainless steel EN 1.4404, while carbon fiber tubes are used for links. The specifications of SPS are reported in Table 5.

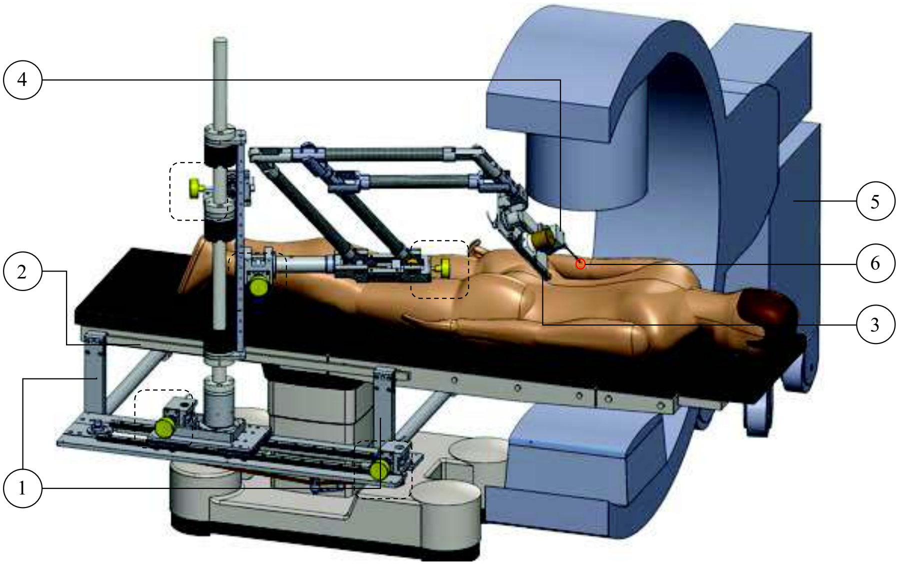

Figure 26: The configuration of the positioning system can be adjusted by manually operating the knobs (highlighted in yellow). 1) clamping bars; 2) side bar of the operating table; 3) linear guide; 4) surgical tool; 5) C-arm; 6) RCM of the double planar parallelogram.

2.3.3 Software for orientation reconstruction

The reconstruction of the cannula placement is based on the possibility of determining the spatial orientation of a segment starting from its two orthogonal projections. The problem can be described considering a single global reference frame x–y–z (Fig. 28), that can be defined by assuring that both the C-arm and the SPS are referenced with regard to the same surgical table. This assures that the orientation of the images relative to the mechanism is correct.

In particular: *i)* the y axis is directed towards the longitudinal axis of the patient, that is prone on the operating table; *ii)* the planar PDP mechanism lies on a plane parallel to the axial one; *iii)* the C-arm lies on a plane parallel to the axial plane and it can be rotated around an axis parallel to the y axis (Figure 20) to obtain two perpendicular projections on the frontal and sagittal planes of the surgical site (antero-posterior and medio-lateral views respectively). The acquired images contain the necessary information to determine the current orientation of the cannula and to plan its insertion so that the drill can safely reach the IVD space. Starting from the antero-posterior and medio-lateral images (Figure 22), the software can evaluate the

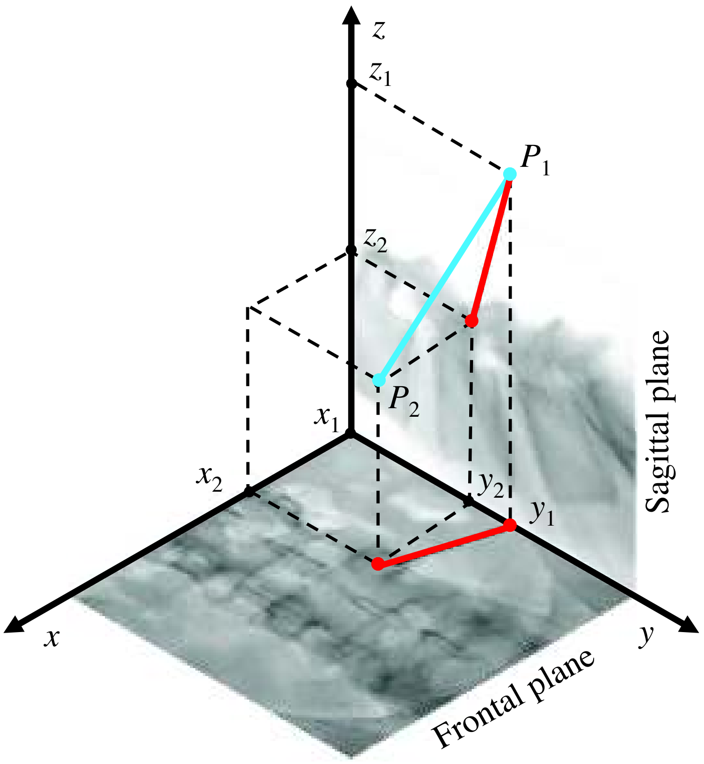

Figure 27: Schematic representation of the cannula orientation (segment $\overline{P_1P_2}$ in light blu) starting from the desired placement (red) identified by the surgeon on the antero-posterior view (frontal plane) and medio-lateral view (sagittal plane).

angles of the rotary joints of the positioning system (θ_1 and θ_2, see Figure 24). Indeed, the software calculates the three orientation angles of an arbitrarily oriented segment with respect to Cartesian axes (α, β and γ).

With reference to Figure 27, from the projections on the sagittal and frontal planes, it is possible to identify the tip of the cannula (point P_2) and its other visible extremity (point P_1) and their projections. In this configuration the tip of the cannula is identified by the coordinates (x_2, y_2) in the frontal projection and by (y_2, z_2) in the sagittal view. Likewise, for the other endpoint of the cannula, the coordinates (x_1, y_1, z_1) of the point P_1 can be identified. Accordingly, the reconstructed segment $\overline{P_1P_2}$

has the same spatial orientation of the cannula. The vector $\underline{r}$ represents the direction of the segment $\overline{P_1P_2}$:

$$\underline{r} = \begin{pmatrix} x_1 - x_2 \\ y_1 - y_2 \\ z_1 - z_2 \end{pmatrix} = \begin{pmatrix} l \\ m \\ n \end{pmatrix} \tag{1}$$

It is possible to calculate the orientation angles of the cannula in the Cartesian coordinate system as follows:

$$\begin{aligned} \alpha &= \arccos(\cos(\widehat{\underline{r}x})) = \arccos(\pm l/r) \\ \beta &= \arccos(\cos(\widehat{\underline{r}y})) = \arccos(\pm m/r) \\ \gamma &= \arccos(\cos(\widehat{\underline{r}z})) = \arccos(\pm n/r) \end{aligned} \tag{2}$$

Once the direction cosines are know, it is possible to evaluate the kinematic parameters of the PDP, namely the angles θ_1 and θ_2. Considering the reference frame shown in Figure 28, it is possible to describe the pose of PDP using a spherical coordinate system. The position of PDP is described by the equation set:

$$\begin{cases} x = \rho \sin(\theta) \cos(\phi) \\ y = \rho \sin(\theta) \sin(\phi) \\ z = \rho \cos(\theta) \end{cases} \tag{3}$$

where ρ is the length of the polar vector. At the same time, a spatial point can be described using the direction cosine:

$$\begin{cases} x = \rho \cos(\alpha) \\ y = \rho \cos(\beta), \\ z = \rho \cos(\gamma) \end{cases} \tag{4}$$

So, substituing Equation 4 into 3 the relation between the direction cosine and the spherical coordinate is obtained:

$$\begin{cases} \sin(\theta) \cos(\phi) = \cos(\alpha) \\ \sin(\theta) \sin(\phi) = \cos(\beta), \\ \cos(\theta) = \cos(\gamma) \end{cases} \tag{5}$$

from which it is possible to derive the following relation:

$$\gamma = \theta \tag{6}$$

$$\phi = \arctan(\cos(\beta), \cos(\alpha)) \tag{7}$$

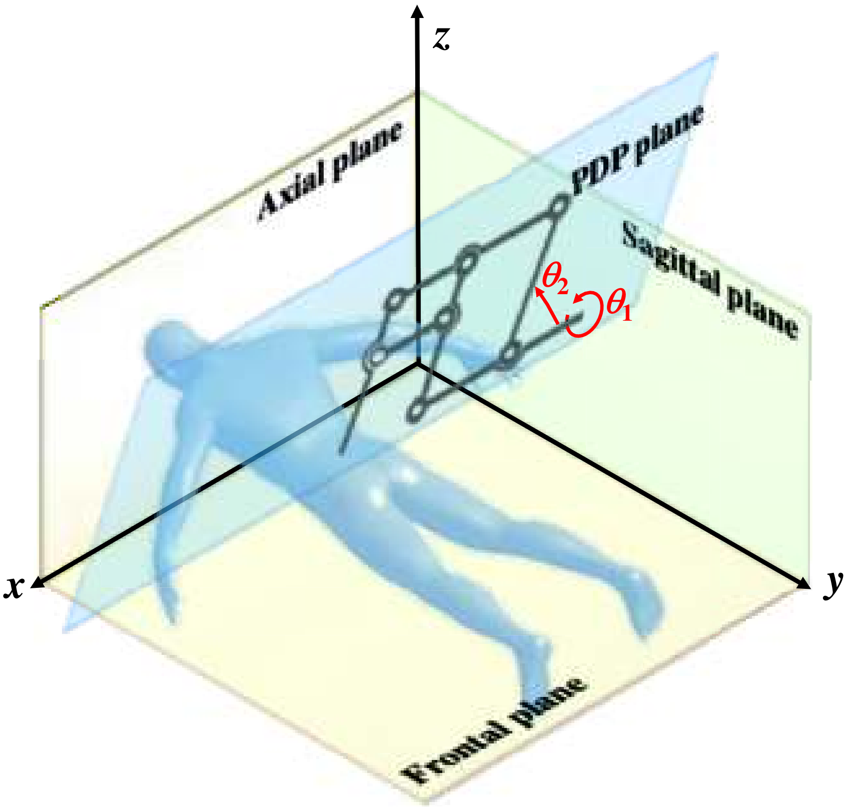

Figure 28: Reference anatomical planes and cannula orientation angles, α, β and γ, with respect to the global reference frame. The angles θ_1 and θ_2 represent the joint angles of the MPD.

Equations 6 and 7 allow, starting from two perpendicular X-ray images, to evaluate the current pose of the PDP and to plan the transpedicular route, by selecting on both images the entry point into the intervertebral disc space.

GUI implementation

As mentioned, the trajectory-planning algorithm relies on the possibility of reconstructing the three-dimensional orientation of a segment using its projections on two orthogonal planes. The software developed and implemented in MATLAB (Mathworks, Natick MA, USA) allows to: *i*) determine the current orientation of the cannula and the related configuration of the positioning system; *ii*) plan a safe route to reach the intervertebral space; *iii*) return the joint parameters θ_1 and θ_2 to update the configuration of the positioning system so that the driller can reach the intervertebral disc space following the planned route. A global reference frame, $O-x-y-z$, is adopted for the resolution of the problem (Figure 3). The calculation of current orientation and trajectory planning requires the following steps:

1. Identifying on both images the same detail (e.g. vertebra thickness, cannula length) and scaling the two views so that such detail has the same dimensions in ML and AP views. In this way, scale changes, due to accidental shifts of the rotation center of C-arm during the acquisition, are compensated.

2. Identifying two points (P_1 and P_2) of the cannula on ML and AP views (e.g. the tip and the distal point) in order to: *i*) operate a registration of the images (along the y-direction); *ii*) evaluate the current orientation of the cannula and the corresponding configuration of the positioning system (Figure 3). These points must have a common y^* coordinate. If during the images acquisition the C-arm is inadvertently moved from its position in x–y plane the software can carry out a calibration for matching the y coordinates of the two projections. The offset calculation is done by evaluating $y_{off} = y_2 - y_1$ so that the images have the same reference frame and the software can continue the planning.

3. Choosing on both projections the desired entry point on the vertebra end plate. The surgeon chooses the desired access points to disc space on the frontal projection, which has coordinates (x_a, y_a) (blue point in frontal projection of Figure 29b). The software draws a straight line ($y = y_a$) on the sagittal view in y–z plane (Figure 29b). Along this line the surgeon has to select the access point in the sagittal view (see blue point in sagittal projection of Fig. 29b). At this point the software draws a line representing the transpedicular route projected on the two views (Fig. 3). Therefore, the surgeon can visualize the planned route and analyze it. If it does not meet the safety requirements for the patient (e.g. it is too close to nervous structures) the surgeon can redefine a new route.

4. Once the transpedicular trajectory is defined, the software returns the joint parameters according to which the operator can manually adjust the configuration of the positioning system (Fig. 3).

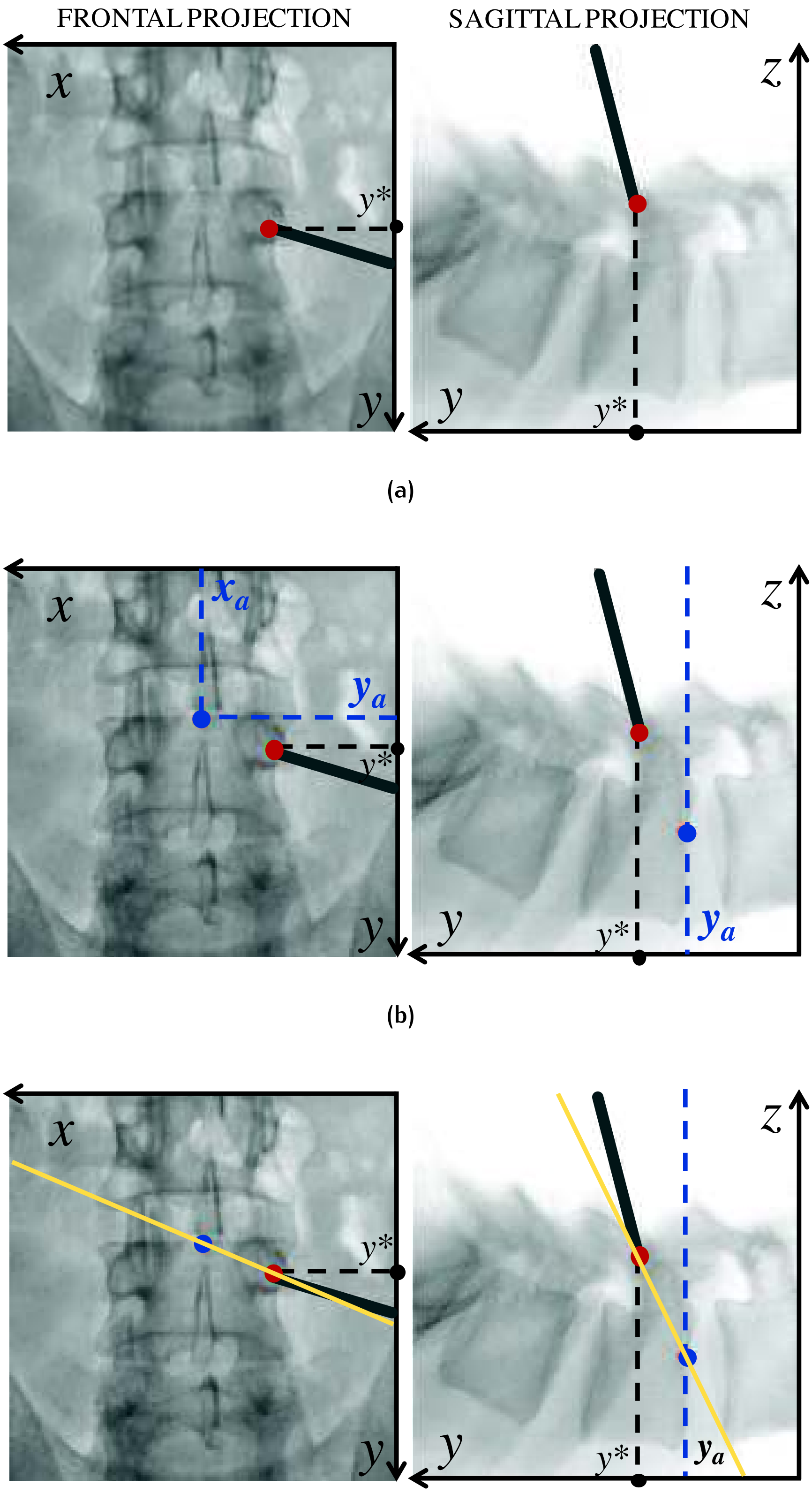

(a)

(b)

(c)

Figure 29: Steps of the orientation planning. 29a Identification of the current position of the cannula tip (red points). 29b. Identification of the desired position of the cannula tip (blue point). 29c Planned insertion direction (yellow line).

3 BONE DRILLING TECHNIQUES

Orthopaedic surgery treats disorders of the musculoskeletal system. There are various types of orthopedic surgery, mainly related to bones or joints, and to the adjacent soft tissues: muscles, ligaments and tendons. In all cases, orthopedic surgery can be performed either traditionally, by open surgery, or arthroscopically. Many orthopedic operations involve drilling tasks into the bone [137]. Bone tissue is an anisotropic viscoelastic, composite material constituted basically by two types of tissue: outside it presents a dense, compact (low porosity) rigid structure, named *cortical* bone. It works like a shell for the inner bone tissue called *cancellous*, or *trabecular*, bone. This is comparatively less dense and rigid and consists of loose networks of bony struts. Spongy bone tissue can completely fill the bone, or circumscribe the medullary cavity occupied by the yellow bone marrow.

Table 6 shows the mechanical properties of different kind of bone tissues [138, 139].

The desired outcome of bone machining, specifically of drilling, is obtaining a tunnel into the bone with required diameter without inducing physical and thermal damage to the adjacent tissues. Drilling into bone is a fundamental skill for surgeons: the task can be easy in the case of long bones, or very difficult as in the case of drilling through the vertebral pedicles, where incorrectly drilled holes can result in nerve or vascular damage, fractured pedicles, or even spinal cord injuries.

Many solutions have been proposed to improve the safety of drilling procedures. Generally, the key points to be taken into consideration for safe bone machining are:

- effects of machining parameters on bone tissues (e.g. angular speed of the drill bit).
- Tool design and kind of technology adopted for development of new methods and setups.

- Automation and robotics for safety increase.
- Biological impact.

In last decades, different mechatronic solutions for improving of bone machining have been designed and tested. Some of these include the adoption of bone breakthrough algorithms relying on the use of image-based trajectory control or on the implementation of detection algorithms for different bone layers. Other approaches for a safe bone cutting involve the use of piezoelectric blades. In fact, ultrasonic machining of bone is an intrinsic safe technique because the cutting effect regards only the mineralized tissues, overcoming the risk of damaging the surrounding soft tissues.

This Chapter is focused on bone surgery, in particular on different bone machining techniques and related technologies. Different technological solutions are shown and compared in order to highlight the limits and advantages in terms of safety.

Table 6: Mechanical bone properties [18].

Bone type	**Density** (kg/m^3)	**Elastic modulus** (GPa)	**Ultimate strength** (MPa)	**Flexural modulus** (GPa)	**Flexural strength** (Mpa)	**Shear modulus** (GPa)	**Shear strength** (MPa)
Cortical	1800-2000	10-26	60-167	14-22.6	50-180	3.3-6	50-180
Cancellous (high density)	700-975	0.8-1.5	6-12	0.8-1.5	6-12	0.3-0.5	6-12
Cancellous (low density)	300-550	0.07-0.4	2-3	0.07-0.4	2-3	0.03-0.15	2-3

3.1 BONE MACHINING TECHNIQUES: AN OVERVIEW

One of the fundamental steps in bone surgery is bone machining. For example, bone machining is required in fracture repair, laminectomy, bone grafting, dental implantation and osteotomy. Bone machining inflicts new damage to the bone tissue. The process has to be performed gently not to over damage the surrounding healthy tissue. As proposed in [18], bones machining can be carried out with two different approaches:

- **conventional methods**, involving mechanical tools in direct contact with the bone. These methods have the same name of the fundamental operation they perform (e.g. drilling).
- **non-conventional methods**, including novel approaches such as high-energy density radiation-based techniques or integration of existing advanced machining techniques into hybrid methods.

Generally, the key points to be taken into consideration for safe bone machining are listed below:

- effects of machining parameters on bone tissues (e.g. angular speed of the drill bit).
- Tool design and kind of technology adopted for development of new methods and setups.
- Automation and robotics for safety increase.
- Biological impact.

Conventional methods

Conventional methods includes:

- **Drilling**: it is the basic operation for creating a hole into the bone, e.g. for screw insertion to fix fractured parts for immobilization. This technique employs electric or pneumatic drills. Different drill bits are available for different operations (Figure 30).

- **Sawing**: it is the operation of cutting bone to shorten or to change its alignment. It is used in common orthopedic procedures such as hip and knee replacement, wrist/elbow/shoulder surgery. Sawing tools may be powered electrically, pneumatically, or manually. Figure 31 shows different solutions for surgical saws.
- **Grinding** and **milling** operations allow to reshape bone geometries and surface finish. These techniques employs different cutting tools and surgical burs (Figure32).

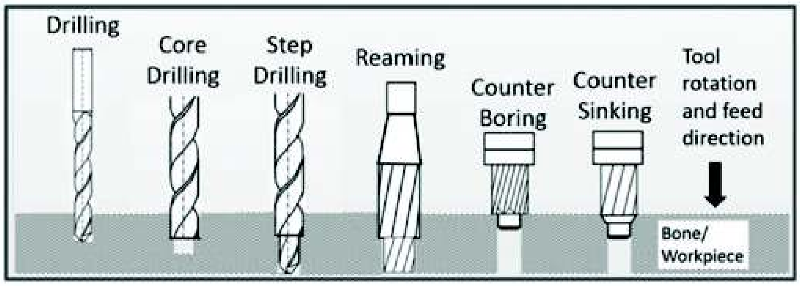

Figure 30: Typical surgical drilling tools for bone machining.

Figure 31: Typical surgical saw: (top) longitudinal and (bottom) transverse.

For the purposes of the transpedicular procedure described in Chapter 1 it is necessary to create a hole inside the vertebra to access the intervertebral space. For this reason the drilling technique will be furthered detailed in the next Section 3.2.1.

Non-conventional methods

Other approaches for bone surgery, as anticipated, involve the use of non-conventional methods. These techniques require the use of various energy sources such as photon/electron beams or mechanical vibrations. These techniques include:

Figure 32: Typical surgical grinding tools for bone machining

- **Laser machining**: it uses heat as the primary means of machining and can be used for drilling, cutting and grinding [140]. Laser machining has some of advantages compared to conventional methods in terms of: *i*) no physical contact between tool and bone, preventing possible contamination; *ii*) shorter operation time; *iii*) no traumatic vibrations; *iv*) electronically controlled cutting precision and *v* possible cauterisation effect [18].

- **Microwave machining**: it exploits the low dielectric loss of the bone. This kind of material allows the microwave to pass through and react with hard tissues causing heat generation by resistive losses of moving charged- ions and oscillations of charged molecules. At temperatures over 50° C, tissues may undergo vaporization and carbonization [18]. This technique is not yet adopted in clinical practice. Its major drawback is the undesired damage of adjacent tissues [141, 142, 143].

- **Waterjet machining**: it employs high pressure jet of water for bone cutting, offering the advantages of a precise cut, no tissues heating and it can also be used in the anatomical sites difficult to reach [144, 145].

- **Ultrasonic machining**: it exploits the conversion of electrical energy into mechanical vibrations through resonant parts. The physical principles behind this bone machining technique are abrasion and cavitation. The micro-vibrations created by a piezoelectric transducer produce a high frequency hammering effect, that in turn induces a micro chipping of bone tissues. This technique can be employed for cutting, drilling and grinding. Section 3.2.2 is dedicated to a detailed analysis of ultrasonic tools for bone cutting.

Non-conventional techniques are not as widely used in clinical practice as conventional ones, but hold a huge potential for the future. Nowadays ultrasonic machining is the only used in clinical practice, as other techniques present some drawbacks. In particular, in [146, 147] laser machined bones has been compared with different techniques and more bleeding has been observed respect to ultrasonic machining. Microwave machining presents some constraints related to safety concerns for medical staff, patients and a dedicate operating set up. In addition, in literature are not reported important machining parameters such as force and temperature rise, thus a further detailed investigations are required before microwave machining can be adopted in clinical uses [141]. For what concern the water-jet machining, the most important disadvantage is the need of abrasive particles that might compromise the operative outcome in terms of sterilization and biocompatibility [144, 145].

3.2 COMPARISON BETWEEN ROTATIVE AND ULTRASONIC DRILLS

The aim of orthopaedic cutting tools is to successfully cut bone tissues minimizing the damages inflicted by the surgical tools. With this focus, this Section is dedicated to highlight the difference between rotative and ultrasonic drills in terms of safety and bone post-operative regeneration. The Section continues with the presentation of the two mentioned techniques and then, the clinical results of their application reported in literature.

3.2.1 Drilling bone with rotative tools

Drilling machining is the most used techniques in orthopaedic surgery for treating numerous pathologies, although it presents some issues. Drilling with rotary tools involves heat generation causing a transient rise in temperature of treated bone and adjacent soft tissues [148, 149, 150, 151, 152]. Temperature rise induces a trauma to the bone and it can even entail osteonecrosis. Osteonecrosis may also be induced the micro-cracks associated with mechanical stresses [153, 154, 155, 156, 157].

The drilling operation, and related temperature rise, is influenced by different parameters related to the drill specifications and drilling parameters. Pandey et al. in [19], summarized these parameters as in the Table 7.

Many works are reported in literature regarding the drilling performance related to different drilling parameters. Results may be controversial: some works show how a low rotational drilling speed is associated with a lower temperature rise [158, 159]; others suggest that high speed drilling could cause less noxious effect to the bone than low speed drilling [160, 161, 162]. A study conducted on human cadavers highlights that

Table 7: Parameters influencing heat generation in drilling task [19].

Drilling parameters	Drill specification
Drilling speed	Drill bits diameter
Feed rate	Cutting face
Drilling energy	Rake angle
Cooling	Drill wear
Drilling depth	Drill point

an increasing pushing force on the drill is associated with a decrease of maximum temperatures, because higher forces reduce the operational time [163]. A few studies relate temperature rise to drilling energy, defined as the energy expended for producing a hole. Drilling energy is directly related to the amount of heat generated during drilling: lower cutting energy is associated to less thermal stress in the cutting region, while higher cutting energy implies higher heat generated leading to higher temperature rise [164, 165]. It has been demonstrated that high drilling speed associated to a high force is desirable in terms of temperature rise [166, 167]. Clearly, the temperature rise during drilling is also influenced by the mechanical resistance offered by the drilled tissues and, in the case of percutaneous approaches, by the surrounding soft tissues that represent a mechanical load for drill bit rotation [168, 169].
Some precautions for reducing the intra-operative temperature rise have been identified. Modern drills are equipped whit a coolant system for the irrigation of surgical site [170, 171]. In order to improve the performance of drilling task, drill and related drill-bits design, and the relative position between drill-bits and bone also have been investigated. The studies demonstrate that a larger drill-bit diameter causes a higher temperature rise [171, 148, 172], but at the same time a smaller drill bit diameter increases the risk of deviation from the target entry point [173]. Other studies present mathematical models or FEM analyses to predict temperature rise and optimize drill design [151, 174, 175, 176, 177, 178].

3.2.2 Ultrasonic bone cutting

Ultrasonic machining technique of biological hard tissues (e.g. bones and teeth) is in use since the middle of the 20th century [179, 180, 181, 182]. The first ultrasonic devices for cutting biological tissues were usually used with an abrasive paste between the device tip and the bone. In 1955 Vang patented the first vibrating device, which could cut both soft and hard tissues without the need of an abrasive paste [183]. In 1974, Volkov presented 311 cases in which an ultrasonic drill simplified orthopedic procedures [184]. In that study, the device drove an end-effector (chisel or saw) operating at 25-30 kHz longitudinal vibration with peak-to-peak tip vibration amplitude greater than 50 μm. Temperature rise did not exceed $70-80°$ C for a short duration, up to 10 s, thus allowing minimal cellular necrosis. In [182], it is shown how different cutting parameters (e.g. operative frequencies, cutting force, cutting rate) influence the outcome. In particular, it was found that cutting force was increased with the thrust force applied by the surgeon. As cutting amplitude of vibration increased the cutting rate was seen to increase and required pressures were reduced. Moreover, it wasn't noted the effect on cutting rate and required pressure related to a variation of the operating frequencies.

Subsequent studies, comparing the performance of these new ultrasonic devices with surgical tools for conventional machining, concluded that the ultrasonic ones provided the surgeon with more precision while reducing soft tissue damage [185]. Nevertheless, material removal rate and post-operative tissue healing rates were found to be slower when an ultrasonic chisel was used. This finding delayed the introduction of ultrasonic devices in clinical practice [186, 187, 188, 189, 190]. In addition, ultrasonic devices were difficult to handle and required manual control of the excitation signal and therefore they were not always driven at the proper frequency [185]. The advances in piezoelectric materials allowed to reduced the instrument size, favouring their adoption in many surgical fields, ranging from maxillofacial surgery, neurosurgery to orthopaedics. Ultrasonic bone cutting has advantages in controlling tissue damages because [191, 192, 193, 194, 195, 196, 197]:

- it reduces the cutting temperature and associated detrimental after-effects to the bone.
- It selectively cuts only mineralized tissues, avoiding damages to soft tissues for frequencies in the range of $25 - 35$kHz. In fact, in that frequency range soft tissues can vibrate at the same tool tip frequency without trauma [198].
- It reduces bleeding, as observed during maxillofacial surgery. This effect may be due to cavitation effect associated with ultrasonic vibrations [199, 200].
- It can create a precise and thin cutting line in any direction, even in areas with a difficult access. Also curvilinear cutting is allowed [201]. This characteristic allows to adopt ultrasonic cutting also for cranial osteoplasty [202, 203].

Nowadays, different commercial ultrasonic tools are available on market for bone cutting. Table 8 shows the devices currently used in ultrasonic surgery and their main features and capabilities.

Despite its many advantages, piezoelectric surgery still has some drawbacks compared to conventional techniques:

- it is slower compared to burs or oscillating saws [20, 204, 191].
- It is associated with a longer initial learning time as surgeons have to become familiar with the use of ultrasonic chisel during the osteotomy procedure [20, 204, 205].
- It is restricted to minimally invasive surface bone works.
- Increasing pressure on the hand tool is discouraged, as increasing the working pressure impedes the vibration of the tip, thus the energy is transformed into heat triggering osteonecrosis [206].

3.2.3 Clinical evidences

Many clinical studies show the benefits of ultrasonic devices. In particular a lot of study using Piezosurgery (Mectron, Carasco, Italy) are available in literature. Piezosurgery is a tipycal ultrasonic vibration cutting device which consists of a generator that

Table 8: Devices currently used in ultrasonic surgery [20]. All of them are equipped with irrigation system.

Device name / Company	**Surgical procedures**	**Frequency range (kHz)**	**Cut depth (mm)**
Piezosurgery, Mectron S.P.A.	dental, maxillofacial, spinal, ENT, neurosurgery	24-36 (oscillating in longitudinal and flexural mode)	up to 20
BoneScalpel, Misonix	use for osteotomy	22,5 (oscillating in longitudinal mode)	up to 20
Sonopet Ultrasonic Aspirator, Striker	maxillofacial, orthopedic, neurosurgery	25-34 (oscillating in longitudinal and torsional motion)	shallow depth

Figure 33: Histologic photomicrograph of cutting bone with different devices. From left to right: osteotomy by bone saw, bone bur and bone ultrasonic system. The ultrasonic system used was Piezosurgery (Mectron, Carasco, Italy) [9].

generates high-frequency elettrical signals, an operating handle that includes ultrasonic transducer, an amplitude transformer and works tips [207]. In Figure 33 a comparison of dissections made with Piezosurgery device and a traditional cutting tool is shown. In [9, 207, 208] it is pointed out that the ultrasonic cut:

- has a more controlled geometry (e.g. parallel edges);
- reduces burnt tissues and allows faster healing;
- minimizes traumatic stress. In fact, the removal of bone with an ultrasonic cutting device takes place in a single plane (longitudinal direction) compared with the rotary drill, which has both a push and pulling action, involving torque values harmful for bone tissues [191].
- protects vital soft structures such as blood vessels and nerves.

Piezosurgery and conventional osteotomy has been compared in different clinical investigation and application. In [208], the authors compare the use of Piezosurgery, oscillating saw and high speed rotative drill in performing cranioplasty. In this study 34 procedures were conducted, of which 18 using Piezosurgery. The duration of osteotomy was significantly longer in Piezosurgery group, but it is compensated with a slightly blood loss respect to the conventional methods. With regard to safety of soft tissues, the same precautions were needed respect to the three different methods. Also in [203], Piezosurgery is recommended for craniofacial surgery, able to prevent dura matter damages. Another study relates the results of the inferior third molar extraction with Piezosurgery and rotative drill

[209]. In this case, Piezosurgery was associated with less post-operative discomfort due to minimal bone injury caused during cutting. Furthermore, new bone formation was more rapid than with rotative drill and the need for pressure on the handpiece was lower. Other studies for intra-oral and maxillofacial applications showed that the Piezosurgery is the best solution for bone harvesting, even for very dense cortical bone [210]. The ultrasonic vibrations allow the cleavage of the solid interfaces facilitating the separation of the graft from the donor site [190, 211, 212]. In [196] the authors reviewed the published literature on ultrasonic osteotomy in oral surgery and implantology. Summarizing the advantages and disadvantages, they state that ultrasonic osteotomy is the only choice in procedures with high risks of damage nerve tissues, offering a valid alternative respect to conventional tool adopted in neck and spine surgeries. Al-Mahfoudh et al. in [213] describe their preliminary experience of ultrasonic bone cutting in spinal surgery using Misonix Bone Scalpel ™ in 62 cases. The bone cutter was used to achieve laminectomies for access to intradural tumors with minimal neurovascular and soft tissues damage and no long-term complication. Graouvogel et al, using Piezosurgery for anterior cervical discectomy with fusion list the advantages of piezoelectric cutter, but suggest a re-design of the handpiece to facilitate the intraoperative handling [214]. Other experiences in hand, otologic, orbital and long bone surgery with piezoelectric cutter device are reported in [190, 215, 216, 217]. Generally, it can be concluded that the adoption of ultrasonic device:

- reduces the cutting force to cut hard bone compared with conventional tools. In [218] is reported a reduction on thrust force from a maximum value of 66 N for conventional drilling to a maximum of 36 N in ultrasonically-assisted drilling.

- reduce the temperature rise during clinical surgical procedures compare with rotative tools. In particular, for piezoelectric surgery the amplitude of vibrations do not influences bone temperature, unlike drilling speed and feed rate [219, 220, 221].

- allows a very precise cut because it is produced by vibration of the tip. In fact, when surgeon handles the piezoelectric handpiece is not solicited by the tool vibration, unlike of motorized cutting tools. This allows a greater surgical sensitivity and dexterity [222].

3.3 BONE LAYERS DETECTION METHODS

Manual surgical drillings tools are not equipped with any means to estimate if the drill bit is continuously in contact with bone tissues or not. This is valid both for conventional and ultrasonic tools. Generally, the accuracy problem in automatic bone drilling consists of how to find the right drill termination moment guaranteeing that the rear hole will not be widened. The penetration depth can be checked through X-ray images for qualitative analysis and the decision if the hole has been completed completely depend upon surgeon experience and sensitivity. In fact, during drilling task the surgeon push on the drilling tool and the drill bit at the moment of breakthrough can further advance with the high risk of procedure failure, or worse causing irreversible damages to patients. Thus, the stop of the drill advancement completely depends upon the surgeon readiness. During surgical procedure the surgeon is obliged to take many X-Ray images to monitor the drill-bit advancement progress during drilling, which requires to interrupt the procedure. This practice compromises the health of medical staff and patients exposed to ionizing radiation. Many efforts were spent to evaluate the dose of exposure: despite in all the conducted studies it was found that the radiation was within the permitted limits, no long-term study about low-dose exposure for prolungated time has been conducted [223, 224].

In the past few years different approaches have been adopted to implement solutions to the described problem. On one side mechatronic systems for semi-automatic or automatic drilling procedure, using predefined penetration depth values, have been developed; on the other side using control algorithms to analyze the measurements of sensors coupled with the drill bit. Several authors proposed algorithms for the detection of the drill bit breakthrough when drilling into the bone as a tool for increasing the safety of drilling procedures. Using a drill pushed against the bone at constant feed rate, the thrust force and torque were acquired and processed [225, 226]. In fact, thrust force and torque rapidly raise and fall when the drill bit pierces different bone layers. Many algorithms are based on the detection of force/torque signals, which are compared given thresholds: when such thresholds have been reached, the algorithm assumes that the drill bit has penetrated the boundary of a bone layer (Figure 34). Some of the methods for de-

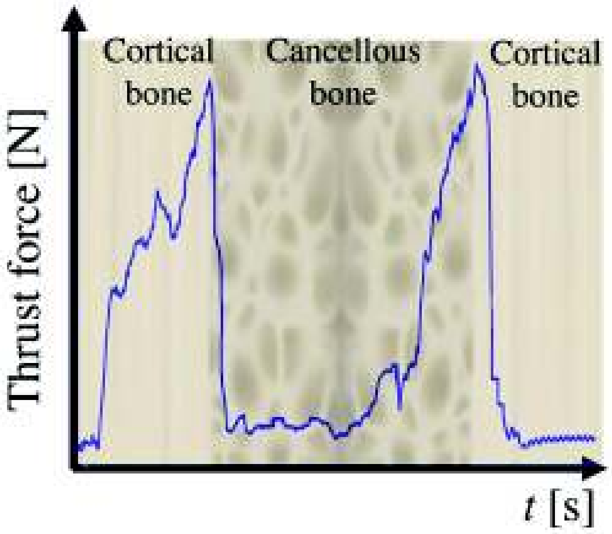

Figure 34: Trend of thrust force applied to the drill bit during drilling. Adapted from [10].

tecting bone breakthrough are shown in the Table 9. Generally, algorithms require that:

- the axial movement of the drill bit is velocity controlled;
- the penetration force, measured by a force sensor, is used as input the detection algorithm;
- layer transitions are identified by comparing force/torque values with assigned thresholds.

Table 9: Bone breakthrough detection methods.

Authors/ Reference	**Measured signals**	**Drill advancement method**	**Drilled tissues**	**Breakthrough detection method**
Brett, Taylor et al., [1995], [225, 227]	Torque/ thrust force	Constant feed rate	Flexible bone tissues (ear surgery)	Associated with increase of drilling torque and decrease of thrust force
Allotta et al., [1996], [228]	Torque/ thrust force	Constant feed rate	Long bones	Breakthrough is detected by an upper limit threshold on the derivative of the thrust force
Ong et al., [1995], [226]	Torque/ thrust force/ drill-bit angular speed	Constant feed rate	Long bones	Based on thresholds on the Kalman filtered signal of drilling force between successive samples and the drill bit rotational speed
Brett et al., [2000], [229]	Torque and thrust force in time and space	Constant feed rate	General bones	After characterization of tissue features (e.g. thickness and hardness) using feed force and torque data with respect to time and displacement, the breakthrough is detected using multiple sensory data.
Lee et al., [2004], [230]	Torque, thrust force and feed rate	Position and force control	General bones	According to the threshold information of the thrust force as well as the trend of both drilling torque and feed rate

While manual drilling tools are surely the most widely used in clinical practice some mechatronic hand-held drill, and its respectively control software for cutting depth monitoring, have been also developed and patented [231]. In [232] a depth controllable and measurable medical driver device and method of use is presented. The device and method involve driving rotating bit in an axial direction such that rotation and linear movement are controlled and measurable. The device has both the rotational drive and the axial drive, each one is controlled by the surgeon. The possibility of measuring and controlling separately the rotational and axial movements respectively allow: *i*) to reduce the risks related to heating bone tissues and *ii*) to prevent the penetrating injuries to distal structures. Generally the drilling task can be uncomfortable for the surgeon because the drilling direction can be difficult to maintain. The invention, presented in [233], can allow at the same time, even if handled manually: *i*) to get a reference support on the patient and thus a more precise control of the penetrating bit and *ii*) a control of drilling force providing a stop of the drill bit when the breakthrough is incipient. Other approaches, like the one reported in [234] for brain surgery, aim to providing an automatic bone drilling apparatus. This last invention includes a drilling hand tool, securely mounted on patient, controlled by a fuzzy logic software through a control box and manual-automatic mode switch box. Drilling robots for orthopaedic surgery have been also designed. A three-axis robotic system with a bone drilling manipulator was proposed in [235]. The system consists of an inner loop fuzzy controller for robot position control and an outer loop PD controller for force control of the feed unit. The drilling robot can select a penetration spot and regulate the drilling torque, thrust force, and feed rate. Other more complex system consisting of a 6 DoF robot manipulator equipped with a multi-axis force/torque sensor and an electrical drilling tool attached to the robot's end-effector was developed [236]. In recent year, in order to remove the subjective factor, and avoid the problems of manual bone drilling, ODRO system was developed. Its breakthrough detection is based on the evaluation of the resistant force in relation with the drilled tissue characteristics and the used drill bit. The control algorithm operates in two regimes: *i*) drilling up to a preliminary desired depth and *ii*) drilling through the whole bone. In the second regime, the control algorithm allows an automatic drilling break when the bit reaches the marrow. [237, 11, 238, 239].

Figure 35: Orthopedic Drilling Robot (ODRO) [11].

These systems and related breakthrough algorithm mainly suffer from:

- they are based on threshold values of the thickness of the different cortical layers of the bone, often preventing sensing capabilities during perforation in the case of encounter with a soft tissue.
- the need of a manual orientation which hinders the possibility of holding a specific trajectory during the bone drilling procedure.
- a completely automatic drilling procedure that precludes the surgeons of any control on the surgical procedure, while they prefer assisting device rather then a substituting one in performing surgical procedures [240].

3.4 OPEN CHALLENGES IN BONE DRILLING

Table 10 summarizes pros and cons of different technologies, in particular it points out how osteotome is performed.

Conventional bone drilling is the standard technique in clinical practice, and despite the large number of publications on this topic and the technological advances, this procedures can be still improved by:

- developing multiphysicis models (analytical or numerical) able to correlate different aspects of machining process, such as temperature rise, drilling force/energy and drill design specifications;

Table 10: Features of bone cutting technologies.

Parameters	**Ultrasonic chisel**	**High speed drill**	**Micro-saw**	**Osteotome**
Operating frequency	~ 20 kHz	80.000 rpm	20000 cpm	single stroke
Tip	blunt blade	abrasive surface or sharp edges	sharp teeth	sharp
Cutting mode	longitudinal	rotational	transverse	longitudinal
Impact force	very low	low	medium	very high
Tip displacement	very low	medium	medium	very high
Tip inertia	very low	very high	medium-high	n/a
Tip start/stop	very fast	delayed	minor delay	n/a
Mechanical effect on soft tissues	minimal	very aggressive (wrapping and tearing)	very aggressive (tearing)	very aggressive

- designing an automated drilling apparatus for minimizing human errors and improve bone drilling accuracy;
- further developing other machining methods such as the non-conventional one, or hybrid solutions.

The rising temperature and the high risk of damaging the surrounding tissues represent the major drawbacks linked to this technique. Among the non-conventional approaches the most promising to be adopted in clinical practice, in substitution of the rotative technique, is the ultrasonic cutting. As reported, the ultrasonic cutting of bone tissue attempts to solve the problems that rotary drill cutting involves. The complete substitution, however, will not take place until the ultrasonic cutting is not suitable for deep cuts.

In fact, no previous study describes a tool for the creation of deep holes into the bone using ultrasonic devices. Some authors have adopted for this specific task hybrid solutions, such as ultrasonically assisted rotative drill (Figure 36) [12, 241, 242]. This solution has been tested in bone and was found to allow for a reduction of thrust force, torque and temperature rise [218, 221]. This technique, as opposed to the ultrasonic one, despite the advantages listed, still suffers from the drawbacks due to the use of a rotative drill-bit, which is not able to preserve soft tissues from mechanical damages.

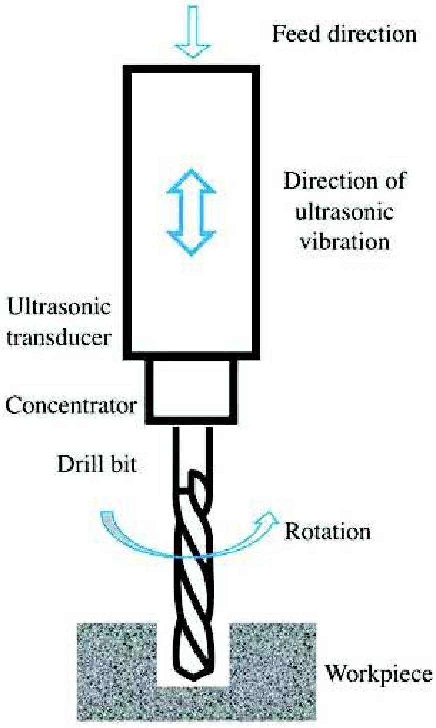

Figure 36: Principle scheme of ultrasonically assisted rotative drill, adapted from [12].

The design of an ultrasonic system for deep hole in bones can take inspiration by systems adopted by NASA or the jewelry industry for hard rocks drilling. In the early 2000s, in anticipation of planetary exploration programs, Cohen et al. developed an Ultrasonic/Sonic Driller/Corer (USDC) for in-situ rocks sampling [13, 14]. The USDC used a novel driving mechanism, based on a piezoelectric actuator oscillating at ultrasonic frequencies, that causes a free mass to resonate, at sonic frequencies, with a lager amplitude. The free mass oscillates against a drill bit where the impact creates a stress impulse at the drill tip where the rock interface is, causing it to break (refer to Figure 37). The removal of any rotating parts allows for smaller drill-bits. This feature makes such solution useful in the jewelry industry (Figure 38). A similar device was patented in 1989 [243].

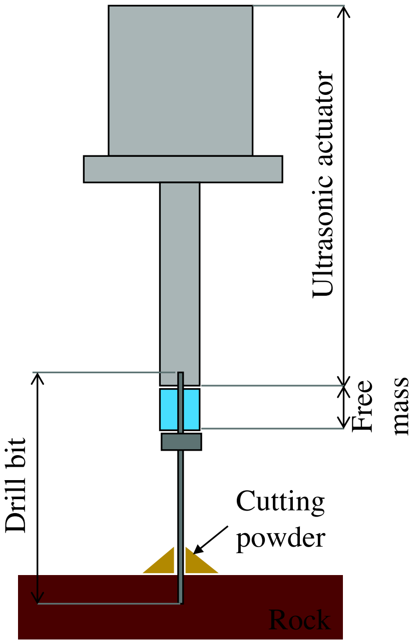

Figure 37: Principle scheme of USDC, adapted from [13, 14].

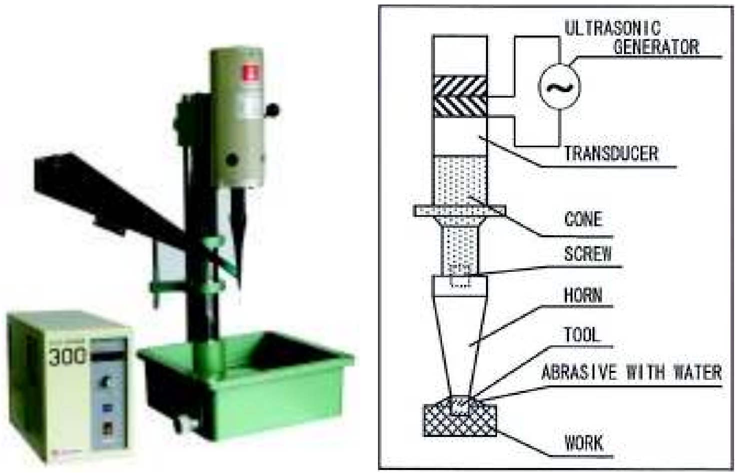

(a) (b)

Figure 38: 38a Lapidary ultrasonic drilling machine used for gemstones, glass, ceramics and others with abrasives past. Produced by *IMAHASHI MFG CO., LTD.* and 38b its working scheme.

4 ULTRASONIC SURGICAL DRILL

As shown in Chapter 3, the ultrasonic cutting of bone tissues represents with its advantages the best alternative for bone machining as alternative to the conventional techniques. Given the high reliability of this technique it is possible to suppose that it can also be used in high number of different surgical procedures, as the creation of transpedicular routes for intervertebral disc regeneration. Nowadays, the major limit of the adoption of piezoelectric surgery in standard orthopaedics procedure, e.g. for the bony housing of pedicular screws, is that it allows only shallow cuts on the bones. This is due, how it is reported in many previous investigation, to the higher temperature associated with ultrasonic cutting able to lead to irreversible damages to the bone and to the surrounding tissues. For those reasons, the manufactures of ultrasonic device for bone machining are only offering products for minimally invasive procedures in maxillofacial surgery and bone grafting. As results, together with the purpose of this research explained in Chapter 1, have led to further investigations about the possibility of developing a new ultrasonic drill for bony deep holes.

In this Chapter the essential components of an ultrasonic cutting device and the main principles regarding the design of resonant systems are described. Design tools currently used, as finite element simulations and methods for component validation, are also presented. Although ultrasonic cutting is an established technology, design processes are often poorly documented and rely heavily on the personal experience of technicians or on the business know-how of companies producing piezoelectric transducers and ultrasonic components. For these reasons in this work a new development process for ultrasonic transducer and mechanical resonators has been developed. The design process involves the use of a software for finite element multiphysics simulation and of tools for validating the simulated performance. In this way, it has been concurrently developed a new design strategy and the drill prototype. Finally, the final design of the ultrasonic drill is presented and the main results are discussed.

4.1 ULTRASONIC SURGICAL DRILL

An ultrasonic system for high power applications, e.g. for bone machining, comprises the key components represented in Figure 39. A power supply converts input voltage frequencies from $50/60$ Hz in $20-100$ kHz to feed a piezoelectric transducer, which represents the drill actuator. The ultrasonic drill is composed of three parts: *i*) the transducer, *ii*) the booster and *iii*) the sonotrode. The piezoelectric transducer converts the electrical energy into mechanical one assuring the vibrational motion of the whole system at ultrasonic frequencies. The produced mechanical motion is transmitted to the booster then to the sonotrode, that are a vibration amplitude-modifying mechanical concentrators. Finally, the sonotrode transfers the energy to the bone (or other materials) to be ultrasonically machined.

The vibration amplification chain must be designed taking into account various vibratory phenomena that develop within the ultrasonic apparatus. The successful application of ultrasonics largely relies on proper design of each single part for very specific vibration performance, specifically of the transducer. Each component is designed to resonate in a single

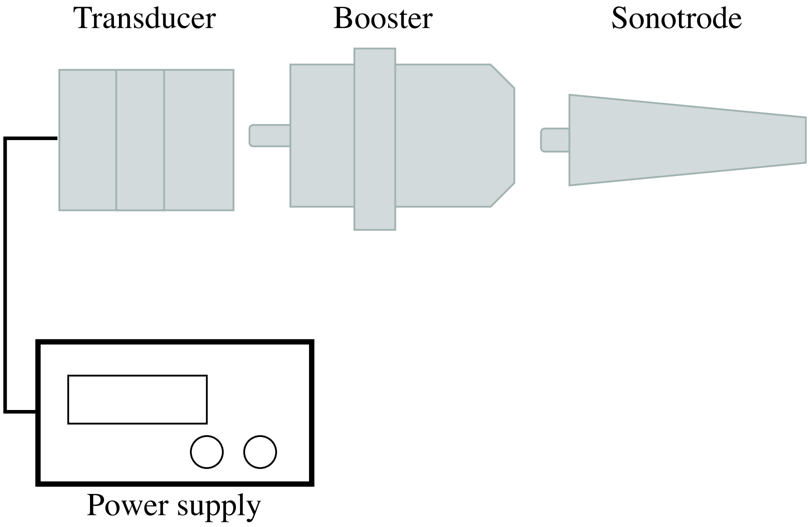

Figure 39: Schematic representation of ultrasonic system for high power application.

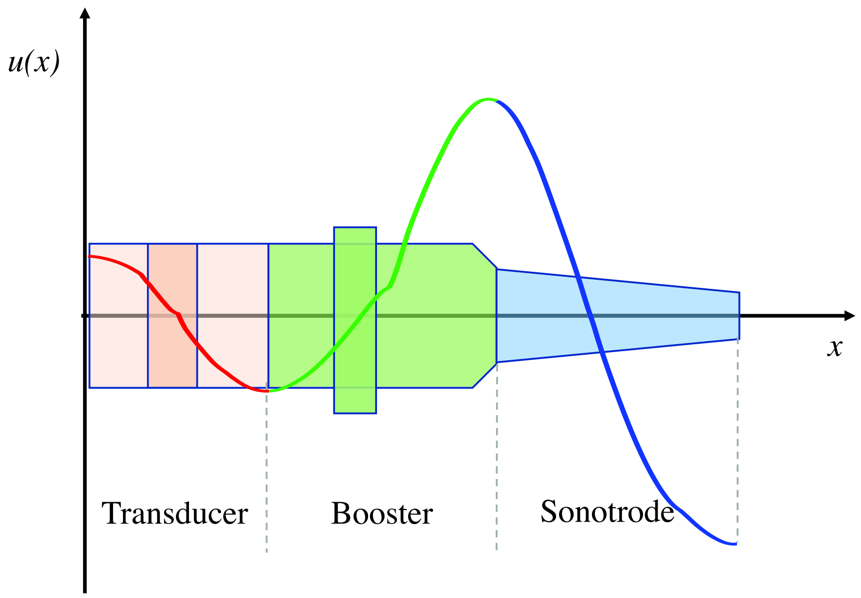

Figure 40: Displacement amplification chain.

mode with vibration frequency higher than 20 kHz: in particular, the booster and the sonotrode are designed to exactly resonate at the frequency f_{res} imposed by piezoelectric transducer. The frequency f_{res} coincides to the frequency of the voltage signal used for piezoelectric transducer feeding. In this way, the whole drill resonates at f_{res}.

If during operation each component has the same resonance frequency, the energy loss is minimized and consequently the transmitted vibrations amplitude are higher. Figure 40 shows a typical trend of vibration amplitude in different points of the ultrasonic drill.

When the transducer, booster and the sonotrode vibrate, they undergo a continuous contraction and expansion, similar to a spring. As show in Figure 40 there are points in which the vibration amplitude is zero. That points are called nodal points, and they are the points of greatest mechanical stress within the system. The nodal plane (the plane that contains the nodal points) is chosen as a mechanical link to connect the vibrating system to any moving carriage or robotic arm. In this way it is possible to handle the ultrasonic drill without interfering with the ultrasonic wave passing through, avoiding a dissipation of mechanical energy.

Due to the high mechanical stress to which they are subjected, the choice of appropriate materials allow a greater lifetime of the component within the materials endurance thresholds, allowing an efficient transmission of acoustic vibration.

The vibrational behavior of booster and sonotrode depends mainly on their length. Changing their length or shape, their natural resonance frequency also varies. A variation of 1 mm of the length can cause a variation of the resonance frequency up to 500 Hz. For this reason, the development phase of tuned elements require very narrow geometrical tolerance. The length of the sonotrode and booster are always the half, or a multiple, of the longitudinal acoustic wavelength that passes through them. The wavelength λ is determined from the speed of the acoustic wave c in the specific material used. Once the working frequency has been chosen, it can possible evaluate the wavelength as:

$$\lambda = \frac{c}{f_{res}} = \frac{1}{f_{ris}}\sqrt{\frac{E}{\rho}} \tag{1}$$

where E is the Young's module of material and ρ its density. This relation is derived solving the wave equation for a simple bar crossed by a vibrational wave: it is clear that for more complex geometries it is not always easy to find an analytical solution to the wave equation. For this, numerical methods are needed. In any case, the equation gives us a first tuned resonator design tool.

As already mentioned, the transducer allows the conversion of electrical energy into mechanical energy and comprises the following components (see Figure 41):

- ceramic **piezoelectric stack**, that is responsible for generating the ultrasound vibrations. The piezoelectric stack consists of up to six ceramic discs interconnected by electrodes for power supplying.

- the **front-mass**, that has the purpose of efficiently connecting the transducer with booster and sonotrode transmitting the ultrasonic waves, and the related energy, as efficiently as possible.

- the **back-mass** that reflects the mechanical wave towards the direction of the front-mass, attenuating it as little as possible.

- the **a prestress bolt** that holds sandwiched piezoelectric stack, between the front-mass and the back-mass, under a compressive load.

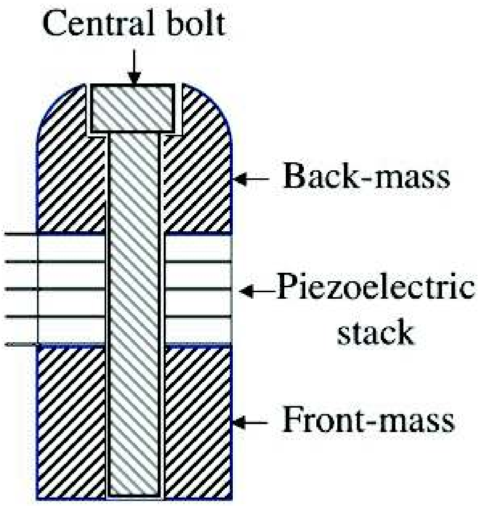

Figure 41: Main components of ultrasonic transducer.

4.1.1 Ultrasonic drill specifications

As mentioned, the transpedicular approach requires the creation a long bony tunnel into the vertebra using the mechanical arm described in Chapter 2, for this reasons the ultrasonic drill:

- must have a long chisel for hole creation (up to 50 mm, Chapter 1);
- must have a diameter in the range of $2 - 2.5$ mm;
- must longitudinally vibrate at resonance frequencies in range $24 - 26$ kHz (typical range for ultrasonic bone cutting);
- have an amplitude displacement (at the tip) in the range of $10 - 50$ µm;
- requires a flange that could connect the drill to the mechanical support.

4.2 DEVELOPMENT OVERVIEW

4.2.1 Principles for ultrasonic resonator design

In ultrasonic engineering tools are designed to vibrate in a resonance condition in the fundamental longitudinal mode. There are a number of design requirements to take into account. The desired frequency and the resonator material determine the overall dimension such as the length. To evaluate the tuned length it is possible to consider an isotropic and elastic slender rod with constant cross-section A and uniform density ρ as show in Figure 42. When the rod is longitudinally excited, a pressure wave produce a displacement u of a small volume of the bar with thickness dx. Under the P force, the element undergo a displacement equal to $u + \frac{\partial u}{\partial x} dx$ at $x + dx$, so it is possible evaluate the elongation ϵ:

$$\epsilon = \frac{u + \frac{\partial u}{\partial x} dx - u}{dx} = \frac{\partial u}{\partial x} \tag{2}$$

If E is the Young's module of the material, the strain σ in the elongated element can be written as follow:

$$\sigma = E\epsilon = E\frac{\partial u}{\partial x} \tag{3}$$

Applying the Newton's second law of motion to an element within the bar dx:

$$-\sigma A + (\sigma + \frac{\partial \sigma}{\partial x} dx)A = \rho A dx \frac{\partial^2 u}{\partial^2 t} \tag{4}$$

and substituting the Equation 3 into the Equation 4, is obtained the wave equation:

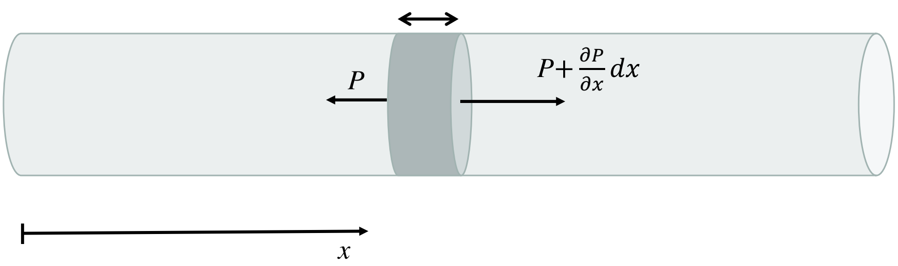

Figure 42: Longitudinal motion of a uniform rod.

$$E\frac{\partial^2 u}{\partial^2 x} = \rho\frac{\partial^2 u}{\partial^2 t} \tag{5}$$

Introducing the speed of sound c in the medium, defined as $\sqrt{\frac{E}{\rho}}$, the wave equation can be rewritten:

$$c^2\frac{\partial^2 u}{\partial^2 x} = \frac{\partial^2 u}{\partial^2 t} \tag{6}$$

To obtain the natural frequency of the slender rod, the Equation 6 must be solved using the method of separation of variables, thus finding the general solution. The general solution for Equation 6 is:

$$u(x,t) = (A\cos(kx) + B\sin(kx))(C\cos(\omega t) + D\sin(\omega t)) \tag{7}$$

where ω is the angular frequency ($2\pi f$) and k is a constant related to the material, equal to:

$$k = \frac{\omega}{c} \tag{8}$$

Boundaries condition is needed to solve the general solution finding the A, B, C and D constants. For a free-free ends rod the boundaries conditions are:

$$\left.\frac{du}{dx}\right|_{x=0} = 0, \quad \left.\frac{du}{dx}\right|_{x=L} = 0 \text{ and } (u)_{x=0} = 0 \tag{9}$$

and considering only time-indipendent solution of 7, the displacement is:

$$u(x) = u_0\cos(kx) \tag{10}$$

where u_0 is the maximum amplitude of displacement and the natural frequency is found to be:

$$f_n = \frac{n}{2l}\sqrt{\frac{E}{\rho}} \tag{11}$$

where n is the mode order and l is the tuned length. For a fixed resonant frequency, the tuned length l can be calculated from:

$$l = \frac{1}{2f_n}\sqrt{\frac{E}{\rho}} = \frac{\lambda}{2} \tag{12}$$

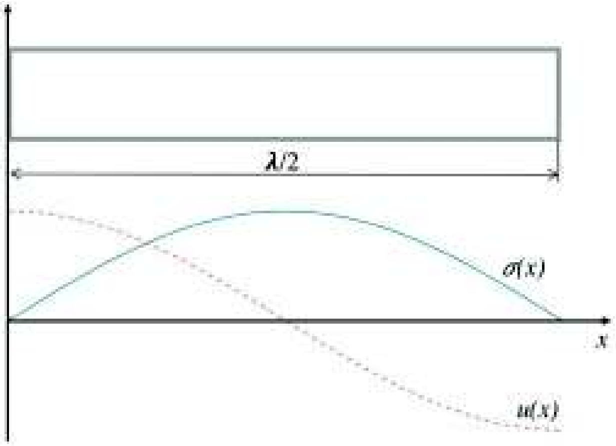

Figure 43: Displacement and strain distribution along a slender rod.

Generally this equation is valid only for rod with diameter $d < \frac{\lambda}{4}$. Finally, using the Equation 3 it can be possible to evaluate the strain distribution along the axis of rod:

$$\sigma(x) = -\omega \rho\, c\, u_0 \sin(kx) \tag{13}$$

The Figure 43 shows the displacement and the strain distribution along a slender rod. It is worth noting that in the nodal point (where $u(x) = 0$), clearly the strain σ has maximum value.

4.2.2 Principles for ultrasonic transducer design

The simplest concept of ultrasonic transducer is the Langevin's model (Figure 44), that involves a piezoceramic stack sandwiched between two metallic masses and a bolt that tightens them [244, 245]. The total length of the Langevin transducer is equal to $\frac{\lambda}{2}$, that allows it to operate in resonance. Under free-free ends boundary conditions the nodal plane divides the actuator in half (each $\frac{\lambda}{4}$ long). An extension of Equation 5 for longitudinal motion in a resonator with variable cross-section $A(x)$ can be written as follow [246]:

$$\frac{\partial^2 u(x)}{\partial^2 x} + \frac{1}{A(x)} \frac{\partial A(x)}{\partial x} \frac{\partial u(x)}{\partial x} + k^2 u(x) = 0 \tag{14}$$

Considering the boundary condition of continuity and force (Newton's third law) of the two contacting media, the following equation can be derived by solving the Equation 14 for $\frac{\lambda}{4}$:

$$\tan\left(\frac{\omega_s\, l_i}{c_i}\right) \tan\left(\frac{\omega_s\, l_c}{c_c}\right) = \frac{\rho_c\, c_c\, A_c}{\rho_i\, c_i\, A_i} \tag{15}$$

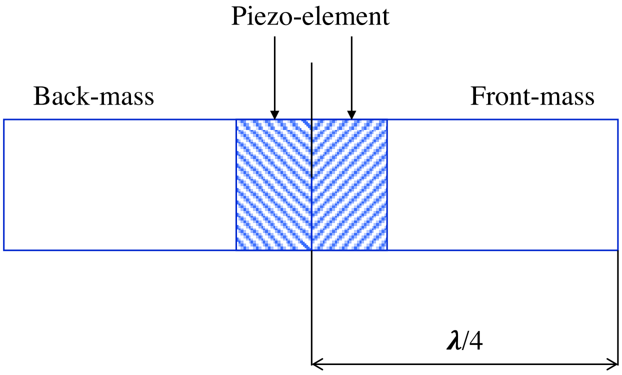

Figure 44: Scheme principle of Langevin transducer.

The quantities subscripted with *i* are associated to the front- or the back-mass, while those subscripted with *c* are associated with the piezoelectric, ω_s is angular resonant frequency, l_c is the partial length of piezoelectric stack located between end or back mass and the nodal plane, A the cross-sectional area and c_c is sound speed in piezoceramics. The Equation 15 can be used to fix an unknown dimension such as cross-sectional area or length or to estimate the resonant frequency.

The acoustic matching between two components joined in series is an essential requirement for a proper working of ultrasonic transducer. When the vibratory wave meets the boundary between piezoceramics and back- or front-mass the wave will be transmitted as well as reflected back into the medium from which it comes. The most efficient transmission of acoustic energy is possible when two resonant elements placed in contact have the same acoustic impedance R, defined as the product $\rho\, c$. However, is not easy finding a material with the same R of piezoelectric disc [247]. For achieving maximum acoustic wave transmission, the following equation, proposed in [248], can be used to select the optimal material:

$$R_c = \sqrt{R_b\, R_f} \tag{16}$$

where R_b, R_f and R_c are the acoustic impedance of back-mass, front-mass and piezoelectric respectively. In according to this relationship, the most used configurations respectively for back-mass, piezoelectric stack and front-mass are *aluminium-PZT-stell* and *stell-PZT-titanium*. It can be useful to make some lateral incisions, like small holes into the front-mass to reduce its acoustic impedance. The diameter of that holes be, at least, of two orders less than the wavelength to prevent the wave propagation [249, 250].

As proposed in [248], the total length of transducer L_{tot} should satisfy the following relation:

$$\frac{1}{3}\left(\frac{c_c}{2f_{res}} + \frac{c_b}{2f_{res}} + \frac{c_f}{2f_{res}}\right) < L_{tot} \leqslant \min\left\{\frac{c_b}{2f_{res}}, \frac{c_f}{2f_{res}}\right\} \tag{17}$$

while for dimensioning the diameter of back- and front-mass, firstly it should be assured that their diameter is at least as equal to the piezoceramic stack one, and then the following relation should be fulfilled:

$$\frac{D_i}{\frac{\lambda}{4}} < 2 \tag{18}$$

where the subscript *i* indicates the *i*-th element of transducer (in this case front- or back-mass).

Also some indications can be considered about the central bolt. In particular in [248] it is suggested a length of the bolt nearly $\frac{\lambda}{4}$. In addition, the central bolt must be dimensioned taking into account the following relationship:

$$(\sigma_b)_{max} = \frac{A_c \sigma_{oc}}{A_b} + 2\sigma_{bmax} \leqslant \frac{\sigma_f}{SF} \tag{19}$$

where $(\sigma_b)_{max}$ is the maximum tensile stress in bolt, σ_{oc} is the prestress pressure on the piezoelectric, σ_{bmax} is the maximum amplitude of the dynamic stress in the bolt, σ_f is the fatigue stress limit and the SF is a safety factor. It is worth to notice that the pre-stress applied by the bolt allows to the piezoelectric stack to achieve higher maximum tensile strength before exceeding its dynamic fatigue limit (Figure 45) [248, 251].

4.2.3 Material selection

The choice of a *good* material to develop components for ultrasonic applications does not depend only on the considerations made concerning the acoustic impedance of the chosen material. The attenuation of a vibratory wave inside a metal body is due to a progressive loss of energy associated with it. This energy decrease is mainly due to two types of effects: the *scattering* and the *absorption*. The first is related to deviation from the longitudinal propagation direction of the wave (reflection), and the second is due to internal friction with resulting heat

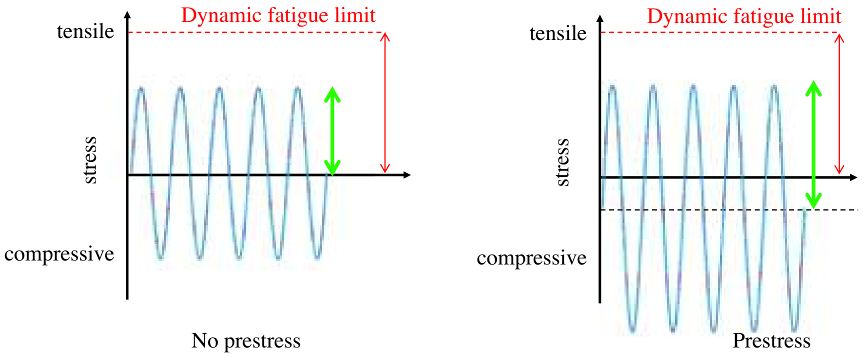

Figure 45: Fatigue stress limit in piezoceramic. Green narrows) maximum tensile strength; Red narrows) dynamic fatigue limit.

generation. The attenuation phenomenon can be described by the following law:

$$A = A_0 e^{-\alpha x} \tag{20}$$

where A_0 is the maximum amplitude of wave and α is the attenuation coefficient. Generally, the energy losses associated with the vibrating system can be calculated as [246]:

$$\delta = \frac{D}{2\pi \times H} \tag{21}$$

where D is the dissipated energy in a period and H is the stored energy. The reciprocal of δ is well know as the mechanical quality factor Q (Q-factor), thus the mechanical quality factor Q is a measure of the energy stored in a periodically vibrating system respect to the energy dissipated per cycle [252]. Ideally, a zero acoustic energy loss (no energy losses due to heat or noise) is the desired condition thus all energy supplied will be transformed into mechanical vibration.

Considering the impedance module curve, the quality factor Q can be calculated experimentally as follows (Figure 46):

$$Q = \frac{1}{\delta} = \frac{f_{res}}{f_2 - f_1} \tag{22}$$

where f_2 and f_1 are the frequency where a 50% decrement of the maximum amplitude occurred (*Full Width at Half Maximum* method) [253]. Generally a high Q-factor, that characterizes the sharpness of the electromechanical resonance spectrum, is required since it implies a lower δ value. In fact it is related to the power dissipation per unit volume P_{loss} by the relation:

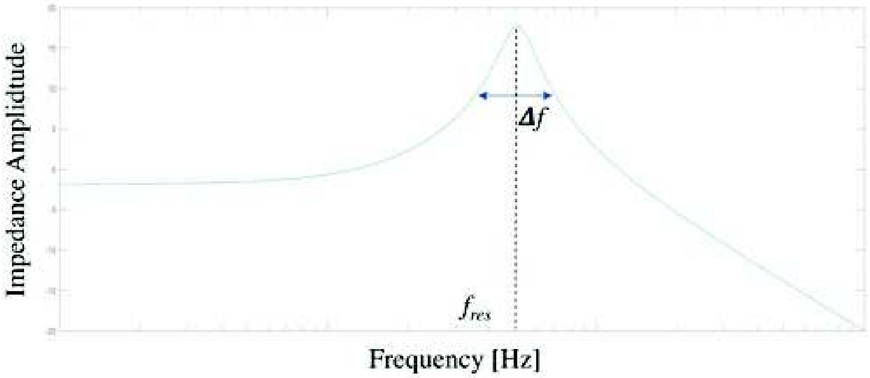

Figure 46: Evaluation of Q-factor.

$$P_{loss}(x) = \frac{\omega}{2E}\sigma^2(x)\delta \tag{23}$$

It is worth noticing that the power dissipation in a resonant element is concentrated in the nodal plane, where the displacement is null and strain assumes its maximum value. Furthermore, considering the acoustic impedance as the ratio between the force that the pressure wave exerts on a particle and the speed of the wave itself, it will assume infinite values in the nodal plane. In order to decrease the power loss, alluminium, titanium or steel alloys are widely used in ultrasonic engineering.

Other considerations must be made about the materials choice taking into account the operational conditions of ultrasonic components. In particular, it is necessary to consider the cyclical tensile stresses to which each ultrasonic component is exposed. For that reason the ultimate tensile strength of the material should be at least 30% higher than the maximum stress experienced within the ultrasonic component during its operation [254, 255]. Using the Huber-Hencky-Von Mises criterion:

$$(\sigma_1 - \sigma_2)^2 + (\sigma_1 - \sigma_3)^2 + (\sigma_2 - \sigma_3)^2 \leqslant 2\,\sigma_0^2 \tag{24}$$

where σ_1, σ_2 and σ_3 are the principal stresses and σ_0 is the yield stress, it is possibile define the general multiaxial stress states of each component. The Equation 24 allows to define the maximum allowable stress in an ultrasonic component, in fact supposing the stress distribution lies along the axial direction (*z(3)*-direction) of the tuned component where no traverse movement exists, the Equation 24 can be rewritten considering $\sigma_1 = \sigma_2 = 0$:

$$\sigma_3 \leqslant \sigma_0 \tag{25}$$

In this way, during the design process it is possible to select the material of ultrasonic components considering a Safety Factor (SF), such that the maximum (yield) stress must lie in the elastic region of the material, according to the following relation:

$$\sigma_{max} \leqslant \frac{\sigma_0}{SF} \tag{26}$$

Typically, SF assumes values greater or equal to 4 for operational safety. In Table 11 are reported the materials often used in manufacturing of ultrasonic component.

Table 11: Mechanical properties of materials used for manufacturing ultrasonic components.

Material	**Density [Kg/m^3]**	**Young's modulus [GPa]**	**Yield strength [MPa]**	**Ultimate tensile strength [MPa]**
$Ti_{6\%Al4\%V}$	4430	113.8	880	950
Stainless steel 316L	7970	193	290	580
Stainless steel AISI 4340	7850	205	470	745
Duraluminium	2700	72.4	276	427

The generation of high frequency vibratory motion is demanded to the piezoelectric materials, that require a *careful* choice based on the specific application. Piezoelectric materials convert electrical energy into mechanical motion, and the vibrations amplitude is dependent on the intensity of the applied field. The most important material parameters that affect the performance of ultrasonic transducers are [256, 257]:

- **electromechanical coupling factor (k_{33})** that represents the efficiency of the piezoelectric material to convert applied electrical energy into its equivalent mechanical energy and vice versa. A higher electromechanical coupling factor is desirable for all piezoelectric applications.
- **mechanical quality factor (Q_m)**, as described above, a high Q_m factor implies low damping and lower power loss.

- **electrical quality factor (Q_e)** it describes the conversion capacity of the electric power to acoustical power.

For high power application, such as for bone machining, it is required that the piezoelectric materials have chemical stability, strong piezoelectric effect and high Curie points. Moreover, a piezolectric actuator used for this application, due to its driving conditions, requires high electrical field and high strain as well as low losses. For these reasons hard piezoceramics, such as PZT-4 and PZT-8, are often adopted. The piezoceramic PZT-4 has high resistance to depolarization, high coupling factor (defined as the ratio of the mechanical energy accumulated in response to an electrical input), high permittivity and low dielectric losses under high voltage drive condition. PZT-8 has lower dielectric and mechanical losses under high voltage drive condition. Furthermore, PZT-8 is also considered a *"harder"* material compared to PZT-4, since it has better stability at higher preloads [258, 259, 260]. The Table 12 shows the characteristics of the two different piezoceramics.

Table 12: Properties of PZT-4 and PZT-8 materials [21, 22].

Property	Symbol	Units	PZT-4	PZT-8
Density	ρ	kg/m^3	7500-7800	7500-7800
Young's modulus	E_{33}^E	GPa	58.9	80.0
	E_{33}^D	GPa	118.80	135.50
Poisson ratio	ν		0.31	0.31
Quality factor	Q_m		500-750	1000-1600
	Q_e		250	250
Dissipation factor	$\tan(\delta)$		0.0030	0.0017
Coupling factor	k_{33}		0.68-071	0.64-0.71
	k_{31}		0.33-0.35	0.29-0.31
	k_p		0.56-0.62	0.51-0.55
Piezoelectric costant	d_{33}	pC/N	285-350	225-280
Coercive field	E_c	V/mm	1500	1600
Curie point	T_c	°C	300-330	300

4.2.4 Driving conditions for ultrasonic transducer

Ultrasonic power transducers are generally driven at a tuned frequency and, exploiting the inverse piezoelectric effect, mechanical motion is induced. The most used electrical signal is a sine wave with fixed frequency (tuned with the resonant frequency of the drill) and constant amplitude. The frequency and amplitude of the feed signal will determine the frequency and amplitude the drill vibrates at. The electrical feed signal can be generally controlled in two different ways: amplitude constant voltage or constant current. Using the electromechanical analogy, it is possible to state that the output force of transducer, when it is powered with constant current, is indirectly controlled. While, when it is powered with constant amplitude voltage it is possible to act on the output vibratory velocity. Generally, the power supplies for ultrasonic applications are produced in such a way to provide two different feed modalities for different applications. Specifically, for bone drilling task current control is preferred, as high output force is required to machining bone. It is worth to notice that the resonant conditions which the piezoelectric devices can be driven at can also be different. In particular it is possible to drive ultrasonic transducer in electrical resonance and anti-resonance ways. In the first case (short circuit condition), the transducer requires an electrical signal with high current and low voltage: this implies high heating within the piezoelectric elements, inducing piezoelectric aging for a long working time. In the second one (open circuit condition) electrical signal with low current and a high voltage is required. Driving under open circuit condition implies lower losses (less heat generation) as well as a higher mechanical quality factor [261, 262].

When piezoelectric transducers are driven at high electric field, frequency softening effect is observed. In particular, resonant frequency shift and electrical impedance variation are common phenomena in the application of high power ultrasonic transducers with high Q, because the performance reduces rapidly at frequencies near the resonance [263, 264]. That fact depends on a variation of elastic compliance of the piezoceramic rings increased with temperature [265]. They result in low power efficiency and unstable vibration amplitude. To prevent low power efficiency and unstable vibration amplitude different driving and measurement system has been developed to track the resonance of high power transducers, and consequently feed the transducer at the desired resonance frequency [266, 263, 267]. This results in low heat generation due to minimum acoustic losses in the system. Modern generators also have built-in safety features such as automatic switch off in case of fracture in the horn or failure in the connections.

4.2.5 Simulation and validation

Design of ultrasonic systems is a complex task, as from the electric, so from the mechanical side. At the end of 60's, numerous scientific papers appear in which are treated different aspects of power ultrasonic technique. Determination of the resonant frequencies of the metal resonator longitudinal oscillations, which have very complex geometry, was done experimentally. In those first experimental investigations certain conclusions were obtained. The most important is connected with transducer and mechanical resonator length. Mathematical treatment of a model of ultrasonic transducer is difficult, because of its complexity. Some important design considerations can be made considering the equations proposed in Section 4.2.2, but they cannot be considered exhaustive for such a complex problem. It should include several equations implying consideration of different mediums that compose the transducer. Not least, the piezoelectric effects should be described and coupled with the mechanical equations that describe the vibratory behavior of the problem. Furthermore, for a precise analysis of transducer motion an ideal model would be three-dimensional, in which is taken into account coupling of oscillations in radial and thickness direction. In general case the complete three-dimensional analysis leads to a very complex set of nonlinear equations, which are practically impossible to solve. However, some one-dimensional mathematical model was developed for studying ultrasonic transducer. Such models, as Mason's and the KLM model, use equivalent electric circuit models for a piezoelectric elements. These models are computationally very cheap and help to accelerate the product design cycles thanks to an effective prediction of transducer performance. Clearly, being a one-dimensional models and related only to the prediction of transducer vibrational motion, those methods have limitations:

- only a one-dimensional pressure field can be investigated;

- they are made for a thin (lateral dimensions much larger than the thickness), loss-less, disc shaped piezoelectric element and they are not valid for a lossy piezoceramic and polymer based piezo element.

- the models are made to simulate an ultrasonic transducer and cannot simulate the interactions of other objects (i.e. booster and sonotrode) with the transducer.

Around the 70's, Courant established the finite element (FE) method for practical use and it was being used by large industries. The FE method works by modeling a structure using a mesh of elements connected together using nodes. To those elements can be assigned simple or complex material properties applied to describe the performance of the analyzed structure. It is possible also take into consideration boundary and loading conditions and a variety of analytical results can be calculated depending on the type of analysis requested by the user. 1D, 2D or 3D modeling is possible and complex problems can be solved quickly and accurately. Nowadays, FE method is considered to be an essential tool in the design or troubleshooting of engineering issues. Also for the study and design of ultrasonic device the FE method proves to be of great use, particularly for the study of the vibration modes of the resonant parts. The computing advances in the development of software for finite element (FE) analysis has led to the development of FE-based software able to simulate problems belonging to different physic domains. It is the well-known case of COMSOL Multiphysics ® software [268]. COMSOL Multiphysics ® can solve multiphysics problems based on coupled systems of partial differential equations (PDEs) allowing the quick and relatively cost effective analysis of ultrasonic components. COMSOL allows to easily create a mesh, subdividing a continuous geometric space into discrete geometric and topological cells in which the solver equations will be applied. An important strength of COMSOL Multiphysics is the ability to couple simulations of different physics. Using this functionality it is possible to couple a mechanical vibration problem to an acoustical problem, or to a piezoelectric effects, and simulate them together, also including the interaction between the acoustical field and the mechanical system.

However, despite FE analysis have enabled more accurate and efficient components to be manufactured, the optimal working conditions for the ultrasonic devices do not depend only by a good design process based on FE analysis, rather also depend on the experimental validation of each developed component, or partial assemblies of them. Experimental modal analysis (EMA) is an experimental process which accurately estimates modal parameters of vibrating structures (e.g. natural frequency, mode shapes and damping factors), and generally for validation and revising of FE models, giving rise to an iterative process reported in Figure 47. It is not only a validation tool but can also be a useful troubleshooting tool. The acquisition of experimental data can be done with two different techniques: i) measuring the response of the free natural vibration of the structure without any applied excitation, or ii) applying forced vibration. Experimental set-up often comprises a signal generator, which feeds the excitation signal into a power amplifier, which is used to vibrate the test structure. Then, the transmitted vibration to test structure is measured by using an accelerometer or laser vibrometer. The acquired signals are often amplified through conditioning amplifiers before being collected and analyzed through data acquisition hardware interfaced to a PC [269, 270]. Although EMA is a reliable and widely used technique, other methods can also be employed to test the results of finite element method of resonant structures. In fact, for this purpose it can be used a measurement of the transducer electrical impedance using impedance analyzer. This method is certainly simpler both from the computational point of view and from the number of tools needed for calculating the resonance frequency of the vibrating system. This measure gives the possibility to verify, on the one hand the FEM simulation and on the other to verify that the assembly of the system has been done correctly.

4.3 DEVELOPMENT PROCESS FOR A NOVEL ULTRASONIC DRILL

This section describes the development process of the ultrasonic drill for the specific application described in Chapter 1. This process takes into account the considerations made previously and introduces the use of COMSOL as a powerful design tool. In addition, it offers a faster and cheaper method of testing simulation and manufacturing/assembly results than those reported in literature. The process workflow is outlined in Fig-

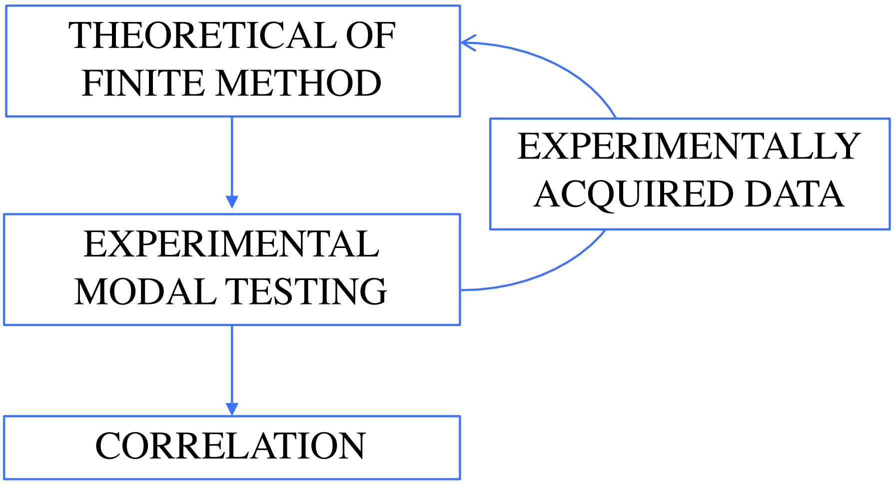

Figure 47: Revision of FE models with experimentally acquired properties.

ure 49. The development of the ultrasonic drill involves the design and manufacture of the three main components of the drill: the transducer, the booster and the sonotrode. Their realization cannot be parallelized, rather it must occur sequentially. The development of each component requires four steps:

- **Rough dimensioning**: in this step a first dimensioning of the components is performed using the analytical tools presented in the previous section (Equations 12, 17, 16, 18). It is worth to notice that in this phase some parameters are fixed due to the project specifications and to the kind of applications. This applies especially to the resonance frequency that is fixed for the application (Subsection 4.1.1). Also the materials are chosen on the basis of the application and for their transmission and reflection properties of the vibratory wave too (Subsection 4.2.3). For the design of the transducer, the choice of the piezoelectric material and its shape (generally ring shape), is crucial. This choice is generally based on the availability of piezoelement (ceramic) on the market. Consequently, the dimensions of the piezoelectric dictate the dimensions of the back-mass and front-mass diameter. Furthermore, when the front mass material is chosen, generally this will be used for booster and sonotrode too.

- **FE optimization**: in this second step, the components of the drill are modeled in COMSOL. In order to define the geometry, the mode shape at predefined natural frequency and performance different studies, and several iterations, are used. In particular, COMSOL offers different tools to model system of different physic nature. In this phase it is important to find the optimal geometry, allowing the component longitudinally vibrates. For this, the resonance frequency is fixed: *i*) for the transducer, by the rough dimensioning, while *ii*) for the booster and the sonotrode, by the tests results conducted on manufactured transducer (see the arrows in Figure 49). Furthermore, it is possible to outline a sub-workflow during the FE simulations (Figure 48): step A) the single component is modeled and modal analysis (eigenfrequency study) is performed to find the vibration mode at desired resonance frequency; step B) the designed component is modeled with the previous component (e.g. booster with transducer or sonotrode with booster and trasducer) and a frequency study is conducted to verify the amplitude displacement and the stress. Step B is valid for transducer modeling too, though there are no previous components. In fact, the frequency study is conducted to analyze the transducer components assembly. Geometrical refinements can be required for the resonance frequency matching of components.

- **Manufacturing and assembly**: after checking that the components are tuned, in this phase they can be detailed in an engineering drawing and manufactured by a mechanical shop. The assembly requires some practical actions, those can be taken in order to enhance the ultrasonic drill performance.

- **Testing**: in this phase, the partially or completely assembled drill is tested using a digital generator for powering and measuring. In particular, the electric impedance curve for resonance frequency and quality factor Q check can be acquired.

4.3.1 FE optimization

In the ultrasonic drill design process physic problems of different nature must be solved. In particular, for a clear comprehension of the problem electrical and mechanical factors

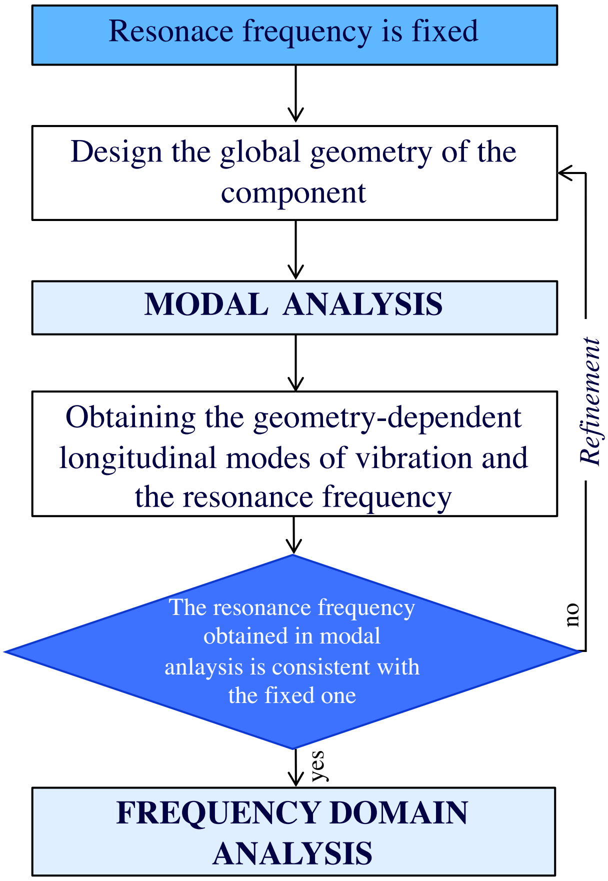

Figure 48: Sub-workflow during the FE simulation.

must be investigate. COMSOL Multiphysics offers the possibility trough different modules to study them singularly or in a coupling way. This is possible thanks to Structural Mechanics Module and AC/DC Module.

The Structural Mechanics Module can be used for simulating applications and designs in the fields of structural and solid mechanics to design new systems and their performances. In this domain it is possible to model several materials comprising the piezoelectric ones. Piezoelectric materials are fully supported inside the module through special multiphysics couplings solving for both the electric potential and displacements. With Structural Mechanics Module static, eigenfrequency and frequency domain study can be implemented.

The AC/DC Module is used to design electric and magnetic fields in static, low-frequency and transient applications in two-dimensional and three-dimensional spaces. The AC/DC Module is necessary, in this case, to evaluate the piezoelectric effect through the Electrostatic interface. This interface is used to

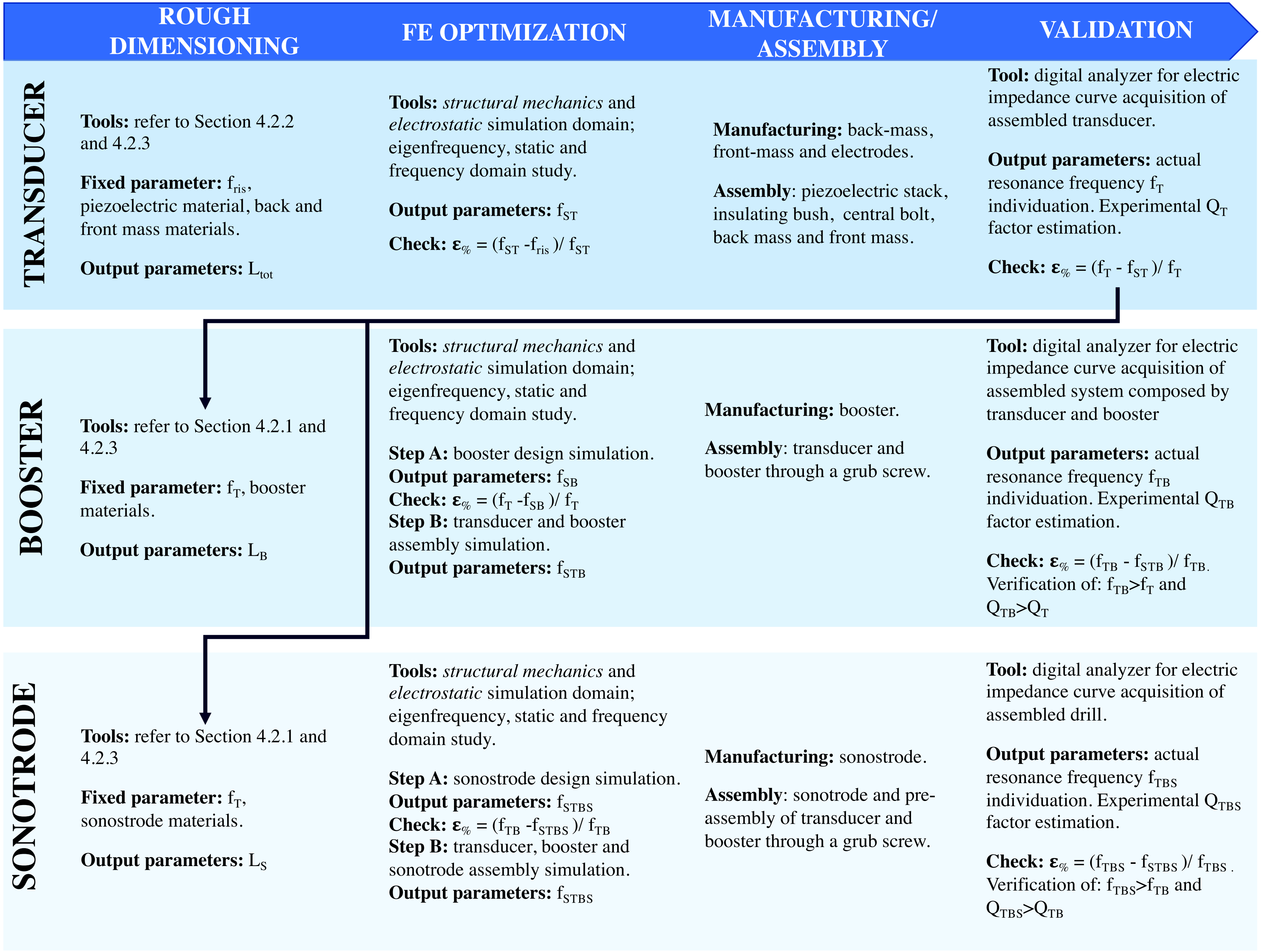

	ROUGH DIMENSIONING	FE OPTIMIZATION	MANUFACTURING/ ASSEMBLY	VALIDATION
TRANSDUCER	**Tools:** refer to Section 4.2.2 and 4.2.3 **Fixed parameter:** f_{ris}, piezoelectric material, back and front mass materials. **Output parameters:** L_{tot}	**Tools:** *structural mechanics* and *electrostatic* simulation domain; eigenfrequency, static and frequency domain study. **Output parameters:** f_{ST} **Check:** $\varepsilon_{\%} = (f_{ST} - f_{ris})/ f_{ST}$	**Manufacturing:** back-mass, front-mass and electrodes. **Assembly**: piezoelectric stack, insulating bush, central bolt, back mass and front mass.	**Tool:** digital analyzer for electric impedance curve acquisition of assembled transducer. **Output parameters:** actual resonance frequency f_T individuation. Experimental Q_T factor estimation. **Check:** $\varepsilon_{\%} = (f_T - f_{ST})/ f_T$
BOOSTER	**Tools:** refer to Section 4.2.1 and 4.2.3 **Fixed parameter:** f_T, booster materials. **Output parameters:** L_B	**Tools:** *structural mechanics* and *electrostatic* simulation domain; eigenfrequency, static and frequency domain study. **Step A:** booster design simulation. **Output parameters:** f_{SB} **Check:** $\varepsilon_{\%} = (f_T - f_{SB})/ f_T$ **Step B:** transducer and booster assembly simulation. **Output parameters:** f_{STB}	**Manufacturing:** booster. **Assembly**: transducer and booster through a grub screw.	**Tool:** digital analyzer for electric impedance curve acquisition of assembled system composed by transducer and booster **Output parameters:** actual resonance frequency f_{TB} individuation. Experimental Q_{TB} factor estimation. **Check:** $\varepsilon_{\%} = (f_{TB} - f_{STB})/ f_{TB}$. Verification of: $f_{TB}>f_T$ and $Q_{TB}>Q_T$
SONOTRODE	**Tools:** refer to Section 4.2.1 and 4.2.3 **Fixed parameter:** f_T, sonostrode materials. **Output parameters:** L_S	**Tools:** *structural mechanics* and *electrostatic* simulation domain; eigenfrequency, static and frequency domain study. **Step A:** sonostrode design simulation. **Output parameters:** f_{STBS} **Check:** $\varepsilon_{\%} = (f_{TB} - f_{STBS})/ f_{TB}$ **Step B:** transducer, booster and sonotrode assembly simulation. **Output parameters:** f_{STBS}	**Manufacturing:** sonostrode. **Assembly**: sonotrode and pre-assembly of transducer and booster through a grub screw.	**Tool:** digital analyzer for electric impedance curve acquisition of assembled drill. **Output parameters:** actual resonance frequency f_{TBS} individuation. Experimental Q_{TBS} factor estimation. **Check:** $\varepsilon_{\%} = (f_{TBS} - f_{STBS})/ f_{TBS}$. Verification of: $f_{TBS}>f_{TB}$ and $Q_{TBS}>Q_{TB}$

Figure 49: Design and development process workflow.

compute the electric field, electric displacement field, and potential distributions in dielectrics under conditions where the electric charge distribution is explicitly prescribed. Eigenfrequency and frequency-domain studies are supported.

Eigenfrequency study

Eigenfrequencies, also called natural frequencies, are discrete frequencies at which a system vibrates depending on its structural properties. The eigenfrequencies are related to the eigenmode, namely the shape in which it deforms.

An eigenfrequency study finds the eigenfrequencies and modes of deformation of a component. The eigenfrequencies f in the structural mechanics field are related to the eigenvalues ν returned by the solvers through:

$$f = -\frac{\nu}{2\pi i} \tag{27}$$

An eigenfrequency analysis can only provide the shape of the mode, not the amplitude of any physical vibrations. In eigenfrequency simulations, COMSOL finds a user defined number of resonant frequencies for the defined geometry. This is done trough eigenfrequency equations predefined within the COMSOL software. When solving for eigenfrequencies COMSOL includes the geometry or interaction constraints, but any loads present in the model are default ignored. It is also possible to include effects from pre-stress. In order to study the pressure/force fields and evaluate the displacement in a simulation model a frequency domain simulations is needed. In Figure 50 it is possible to see an example of the eigenmode for a cylindrical stainless steel free-free ends rod (316 L, refer to Table 11 for material specification) with a diameter of 10 mm and length of 123 mm. It is possible to notice how the longitudinal vibrations appear at a specific frequency of 20 kHz, that is its resonance frequencies (in fact the length is just equal to half the vibratory wavelength in the specific material, refer to Equation 1).

Frequencies domain study

The frequency analysis of a system allows to study the properties of a system as a function of excitation frequency. The frequency analysis in COMSOL Multiphysics produces a frequency response curve, of the linearized response due to a

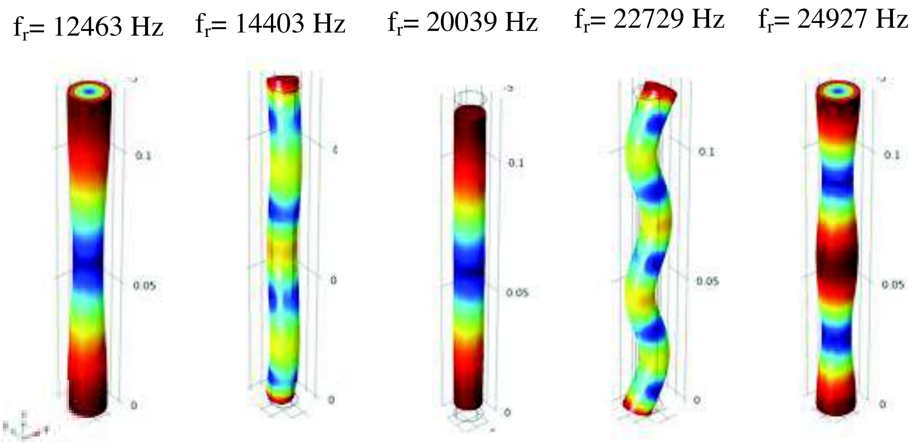

Figure 50: Different vibrating modes for cylindrical stainless steel bar.

harmonic excitation, for a number of different frequencies. A frequency response curve will, in general, exhibit a number of distinct peaks located at the natural frequencies of the system. In the frequency domain simulations, COMSOL solves stress-strain wave equations numerically with the given boundary conditions. It is possible to perform a frequency response analysis of a structure under harmonic load, but also under a prestress load. The loads can have amplitudes and phase shifts that may depend on the excitation frequency f:

$$F_{freq} = F(f) \cdot \cos\left(s\pi f \cdot t \; F_{Ph}(f) \cdot \frac{\pi}{180} \right) \tag{28}$$

where $F(f)$ is the amplitude and $F_{Ph}(f)$ is the phase shift of the load. The result of a frequency response analysis is a complex time-dependent displacement field, which can be interpreted as an amplitude, u_{amp}, and a phase angle, u_{phase}:

$$u = u_{amp} \cos(s\pi f \cdot t \; + \; u_{phase}) \tag{29}$$

In Figures 51 and 52 it is possible to see the result of frequency domain analysis in the range of $7-32$ kHz for 316 L cylindrical rod with a fixed base and a load of $(10;0;10)\frac{N}{m^2}$ applied on the other base. In Figure 51 the amplitude of displacement as a function of excitation frequency, at a point on the face where load is applied, is shown. The peaks in these curves correspond to the the natural frequencies, whose values are reported in Table 13. For a longitudinal vibration analysis is necessary to locate only the longitudinal resonance frequency,

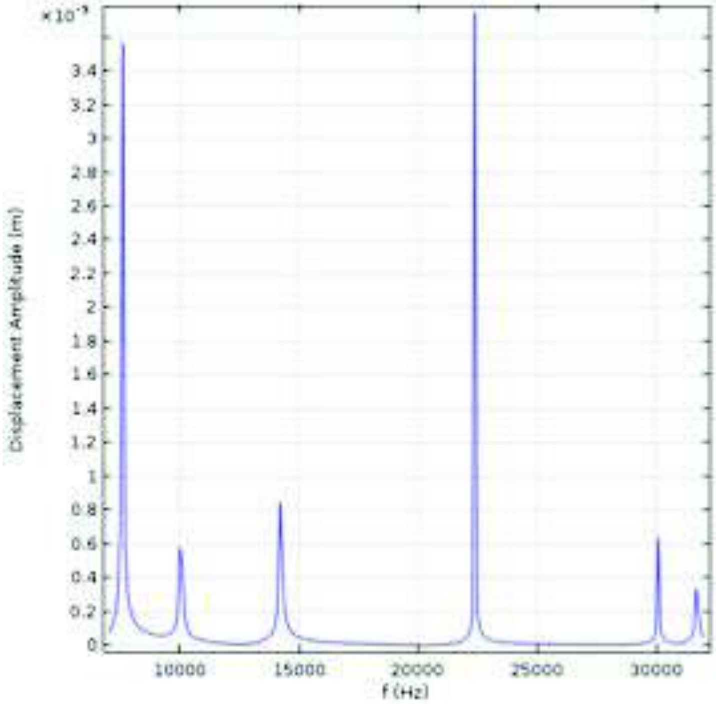

Figure 51: Displacement amplitude vs. excitation frequency.

so in Figure 52 the $x-$, $y-$ and $z-$ amplitude displacements are individually plotted.

In this way it is possible to isolate only the longitudinal frequency for a right vibration mode requested in ultrasonic drill: Figure 53 shows the $z-$ component of displacement. The two peaks correspond to the longitudinal vibration modes at 10045 Hz and 30113 Hz respectively: Figure 54 and 55, finally, show the deformed configuration of amplitude displacement and the Von Mises stress.

Static study

A static analysis has no time dependencies. It is referred to the steady state with constant boundary conditions and material properties in time. The static analysis allows to find the maximum stress level, to compare it with the material's yield strength, and to check that the deformation of the component

Table 13: Natural frequencies (eigenfrequency) of a 316 L cylindrical rod with a fixed base.

Eigenfrequency	f_1	f_2	f_3	f_4	f_5	f_6	f_7	f_8	f_9
Frequency [Hz]	7852	7852.2	10045	14237	18965	22404	22405	30113	31160

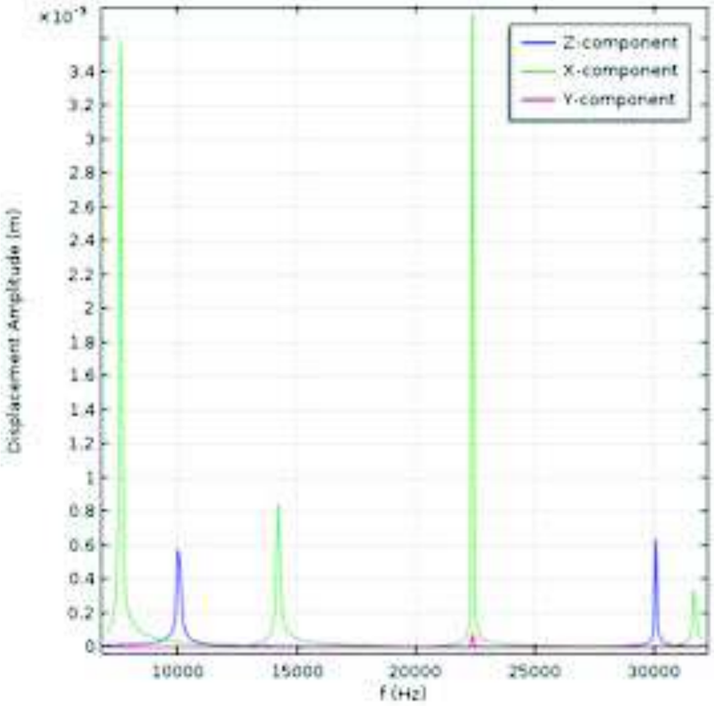

Figure 52: $x-$, $y-$ and $z-$ components of displacement amplitude.

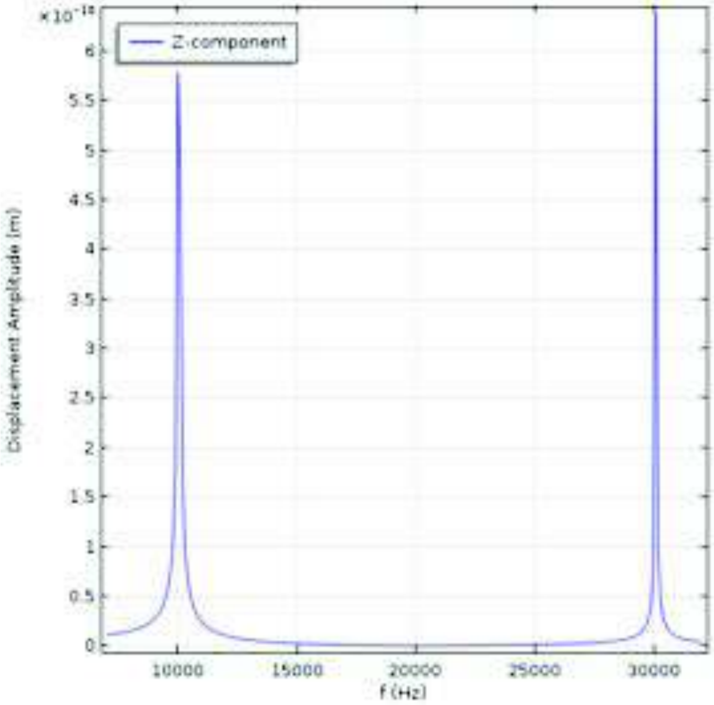

Figure 53: $z-$ component of displacement amplitude.

is within the limits of the design criteria. This study is an essential step for studying the static stress distribution caused by a pretension bolt in a system. The solution from this step

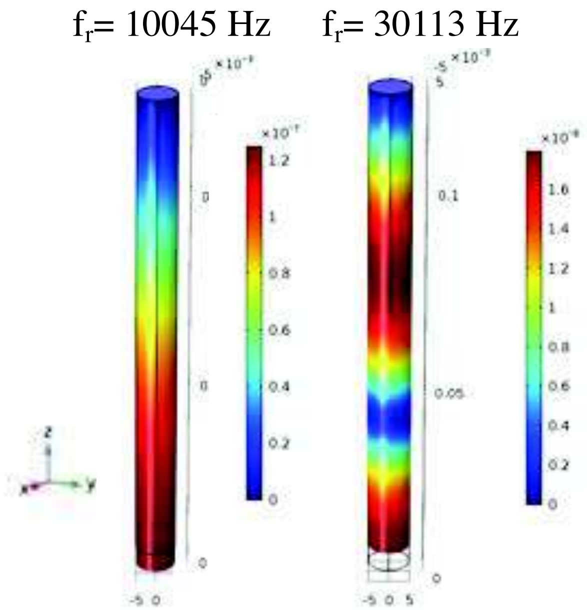

Figure 54: Displacement amplitude at 10045 Hz and 30113 Hz excitation frequency.

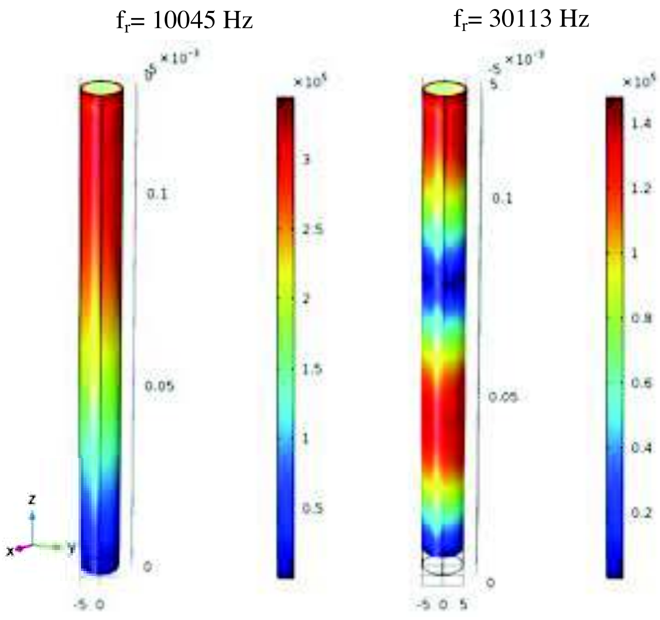

Figure 55: Von Mises stress of the cylindrical rod at 10045 Hz and 30113 Hz excitation frequency.

is then used as a linearization point for solving the vibration problem in Frequency Domain Perturbation study step. This workflow is valid only for small perturbations about the static solution, namely the magnitude of the stress and other physical quantities from the frequency domain problem are significantly smaller than the magnitude of the same quantities obtained from the static problem.

4.3.2 Manufacturing

The tuned components of ultrasonic drill need precision engineering equipment to accurately manufacture the ultrasonic components to the required size, ensuring precise tuning. The components were manufactured using a four axis CNC machine using computer aided manufacture (CAM) technology. In particular, for the manufacturing of the sonostrode a mobile headstock lathe has been necessary due to its shape and dimension (lenght higher than diameter). This kind of lathe allows the front and rear faces of the piece to be processed simultaneously. The material flows through a guiding bush and it is rotated by a second mandrel that helps to push the material through the guiding bush. In this way, lengths much higher than the diameters do not create problems of deformation and vibration.

4.3.3 Assembly

The assembly process of ultrasonic device requires more steps: the first one is the assembly of transducer composed by more element as presented in 4.1; and the second one requires the fastening of booster and sonotrode to transducer through the use of grub screws. Moreover, in order to enhance the ultrasonic drill performance, some practical actions can be taken:

- in order to maximize the energy transfer associated with the propagation of the acoustic waves it is necessary that the surfaces that will be in contact (for example the front mass section facing the booster and those of the booster facing the front mass and the sonotrode) are treated to reduce surface roughness. High surface roughness can cause heat generation and high power loss under operating conditions. A lapping treatment on these surfaces is strongly recommended before assembling the entire instrument.
- it is necessary to make use of isolating bushes placed around the bolt shank to avoid short-circuit by a probable contact between central bolt and the electrodes and to keep back and front mass connected to ground.

- the central bolt must have the specifications of DIN 912, class 12.9.

- threaded body and head of a central bolt, that is fastening piezoceramics and metal masses, should be slightly lubricated with (high temperature stable) molybdenum disulphide grease, before transducer fastening, in order to minimize unnecessary friction during fastening. Sometimes, 30% to 60% of applied fastening torque/pressure is lost in metal-to-metal friction, if central bolt is not properly lubricated.

- after assembly, the transducer is subjected to a heating process to redistribute the accumulated mechanical stresses in a non-isotropic manner during the preload phase. The transducer is placed in the oven for 8 hours at a temperature in the range of $80 - 120°C$ and it is allowed to cool naturally. During the warm up, the electrodes are short-circuited.

Transducer assembly

As described in Section 4.1 the transducer is composed by a piezoelectric stack, the front and back mass and the pre-stress screw. The task of the central screw is the fastening of the system, applying a compressive load to piezoelectric stack. The piezoelectric stack is composed of PZT disks between which electrodes are interposed. The electrodes are interposed between oppositely poled PZT disc and connected in parallel to the power source (see Figure 56). These electrodes are of copper–beryllium discs alloy of 200–250μm thickness with very high fatigue strength. Their surface is finished with nickel-plating treatment for minimizing the roughness.

The pre-stress torque T_{ps} that must be applied to central bolt, can be evaluated by the following relation:

$$T_{ps} = (d_o^2 - d_i^2)\, k\, d_{bolt}\, P_{ps}\, \frac{\pi}{4} \tag{30}$$

where, d_o and d_i are respectively the outer and the inner diameter of piezo-rings, d_{bolt} is the nominal diameter of bolt, k is a lubrication coefficient (it ranges between $0.15 - 0.18$ for lubricated bolt) and P_{ps} is the pre-load pressure. The pre-load pressure can be evaluated as the mean between tensile and compressive yield loads. The torque value can be imposed to the

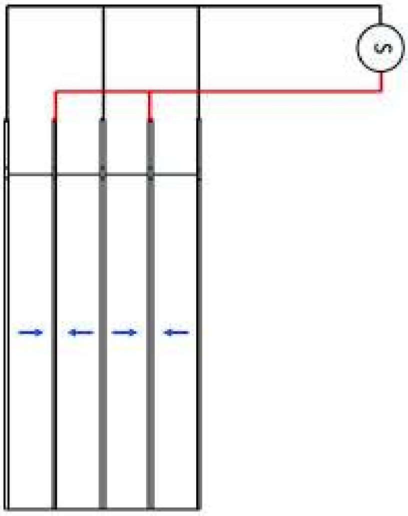

Figure 56: Poling direction of piezoceramic rings (blue narrow) within a piezoceramic stack containing four active elements.

bolt by using a torque meter. At the same time, it can be implemented a measuring set-up using a oscilloscope for measuring the produced charge on electrodes resulted from pre-stress. It is possible to dimension an external capacitance on which it will be possible measure the imposed voltage corresponding to fastening torque required (refer to Figure 57). In particular, the amount of charge accumulated in the electrodes is:

$$Q_{tot} = (d_o^2 - d_i^2)\, n_{PZT}\, d_{33}\, P_{ps}\, \frac{\pi}{4} \tag{31}$$

where n_{PZT} is the number of PZT rings and d_{33} is the piezoelectric constant. The value of the external capacitance C_{ext} can be evaluated as follow:

$$C_{ext} = \frac{Q_{tot}}{V_0} - n_{PZT} \frac{(d_o^2 - d_i^2)\, \epsilon_{33}^T \, \frac{\pi}{4}}{h_{PZT}} \tag{32}$$

where V_0 is the imposed potential with values up to 10V.

Booster and sonotrode assembly

Booster and sonotrode are fastened to transducer in series through a grub screws, as shown in Figure 58. The grub screws are chosen taking into account the dynamic stresses to which they are subjected under the operating conditions. The dynamic stress amplitude in the coupling bolt will be:

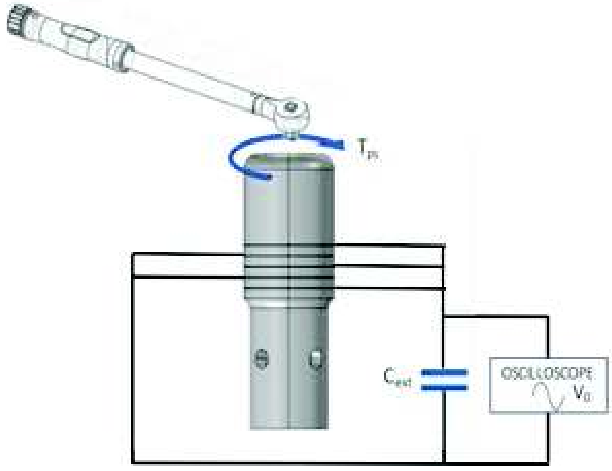

Figure 57: Scheme of transducer assembly set-up.

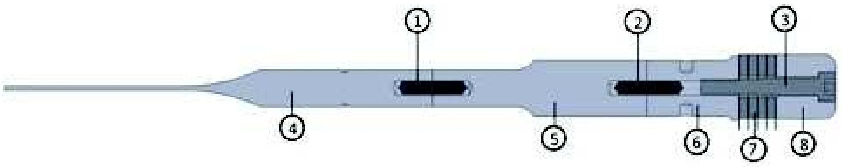

Figure 58: Section view of ultrasonic device: 1) and 2) coupling grub screws; 3) central bolt; 4) sonotrode; 5) booster; 6) front mass; 7) PZT stack; 8) back mass.

$$\sigma_{GS} = \frac{\frac{\pi}{4}\, d^2\, l\, \rho\, (2\pi f_{ris})^2\, u}{A_b} \tag{33}$$

where d is the diameter of the cross-sections fastened by the grub screw, l is the length of the component (booster or sonotrode) that must be fastened at the surface where the output vibration displacement is equal to u. For example, $sigma_{GS}$ for coupling screw between transducer and booster will be evaluated with the booster length.

It is important to notice that when a chain of ultrasonic resonators connected axially to each other (such as transducer and booster or transducer, booster and sonotrode) the resulting impedance-phase characteristic, after adding every new element, will become more and more narrow and sharp. This implies an increase of mechanical quality factors.

4.3.4 Driver

For the power supplying of the ultrasonic drill a digital generator has been used. The adopted generator, Silence Scope (Figure 59), is produced by Itacna s.r.l. (BG, Italy) and its specification is reported in Table 14. This generator offers the possibility to:

- choose three different control strategies: *i*) constant voltage, *ii*) constant current and *iii*) constant active power.
- feed the ultrasonic transducer with fixed frequency signal, imposed by the user.
- feed the ultrasonic transducer with signal whose frequency is evaluated after the identification of ultrasonic device resonance frequency (frequency tracking). This is assured thanks to a controller that analyses the electric impedance of the transducer after a frequency ultrasonic transducer (or entire system: transducer, booster and sonostrode) scanning. In fact, the physical conditions in an ultrasonic application (temperature, pressure, density, viscosity, mass, geometries, materials used, etc.) can change for different reasons, thus inducing a change in the electromechanical response of the ultrasonic system. Ultimately, the behavior of the generator is changed. For this reason, the main parameters that constitute the operating conditions of the generator, and therefore of the entire electromechanical system, are controlled by the generator at each system launch in order to ensure the best working conditions depending on the chemical-physical conditions of the system.
- acquire the electric impedance curve for evaluating the resonance frequency (corresponding to the mimimum peak) and the quality factor Q (Equation22).

The operating conditions of the driver and of the ultrasonic transducer (that can be considered as an electromechanical system) are checked at each system start using an impedance analysis algorithm of the electromechanical system.

This algorithm, thanks to an initial phase where the resonance frequency of the system is found (as the frequency in which minimum peak of impedance curve occurs), ensures the

Figure 59: Silence Scope, Itacna s.r.l., BG, Italy.

Table 14: Silence Scope (Itacna s.r.l., BG, Italy) specifications.

Parameter	Value
Power supply	230 V (±5%),50/60$ Hz
Power output	2000 W
Nominal current	15 A
Nominal voltage	1500 V
Frequency bandwidth	$18 - 120$ kHz
General control strategies	Constant Voltage, constant Current or constant active power
Frequency control strategy	Fixed frequency or Frequency tracking

best working conditions. In particular, the users can set a frequency range in which the ultrasonic system must work. The drive feeds the electromechanical system with sine signal at different frequencies (that belong to the set range), and acquire the impedance curve, thus the algorithm searches the resonance frequency within it. At the end of this *"calibration"* phase, the driver feeds the ultrasonic system at the optimum frequency. Figure 60 shows the connection between the transducer and the driver. The acquisition of impedance curve is useful to estimate the Q-factor during the assembly phase of the ultrasonic drill.

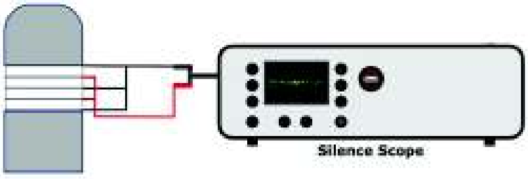

Figure 60: Ultrasonic transducer and Silence Scope interfacing.

4.4 DEVELOPMENT PROCESS RESULTS

4.4.1 Transducer

In order to model the transducer it was necessary to start by choosing the piezoceramic discs material. For this type of application, rings with an external and internal diameter respectively equal to 30 mm and 10 mm have been chosen. The ring thickness is 4 mm. The rings are of PZT-8 (SP8) material produced by CeramTec (Plochingen, Germany). The piezoelectric stack has been composed with four rings, coupling the opposite poled faces. For the back-mass stainless steel AISI 4340 has been choosen, while for the front-mass titanium $Ti6Al4V$. The working frequency has been fixed at 25 kHz.

The working principle involved in the operation of the transducer is that an AC electrical signal applied to the piezostack actuator produces vibrations in the entire transducer: these vibrations are reflected by the back-mass, while the front-mass in turn transmits vibrating waves to the booster. Thus modeling the operation of the transducer requires coupling electrical, structural and piezoelectric phenomena. It is necessary to implement the pre-tension in the central bolt of the transducer to model the effect of prestress on the frequency response characteristics of the transducer.

The final tuned design of the transducer is reported in Figure 61. It has been achieved after several trials in modifying the dimension of the back-mass and the front-mass. In order to reach this result has been necessary:

- to consider the reaction to the tightening process of the central bolt and the pre-tension force experienced by the bolt. This force produces a prestress that helps to hold the bolt in place during regular operation of the device. Note that the tightening of the bolt also produces stresses in materials that are touching the bolt.

- to include fixed constrains for modeling the tightening process during stationary study.

- to consider the poling direction of the piezoceramic, such that alternate disks are poled along opposite directions. This allows to use a single electrical terminal at the interface of each pair of disks and obtain the piezoelectric actuation effect in each disks along the same direction, thus

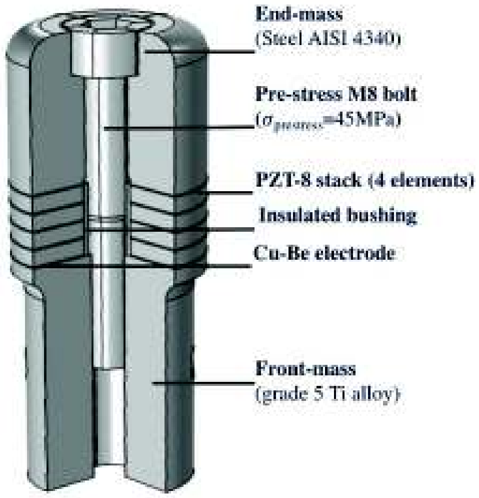

Figure 61: Ultrasonic transducer.

the piezoelectric strain is in-phase in all the disks and the displacement amplitude is maximized. In this model, the PZT-8 disks actuate in the d_{33}-mode. Hence two disks are poled along the +Z-direction while the other two are poled along the -Z-direction.

- to consider the effect of voltage application on the electrodes. Each piezo-ring is excited with 50 V_{RMS} electrical signal.

Following the workflow described in Section 4.3, a modal analysis has been conducted to find the longitudinal vibration mode at desired resonance frequency. For this purpose two study steps have been implemented (static and eigenfrequency). Figure 62 shows the eigenmode of transducer for different eigenfrequency. The longitudinal resonance frequency evaluated from simulation f_{ST} is equal to 25404 Hz. In this way, a frequency domain analysis has been conducted in frequency range of $24-26$ kHz. Amplitude displacement and Von Mises stress are shown respectively in Figure 63 and 64. The curves in Figure 65 shows the amplitude of x-, y- and z- displacement components measured at a point on the free face of front mass: it is clear that the x- and y- components are negligible respect to the z- one, confirming that the transducer vibrates longitudinally.

Furthermore, the Electrostatic Module allows to evaluate the electric impedance in the frequency range: this functionality is extremely useful for evaluating the goodness of the simulation comparing it with the electric impedance curve acquired

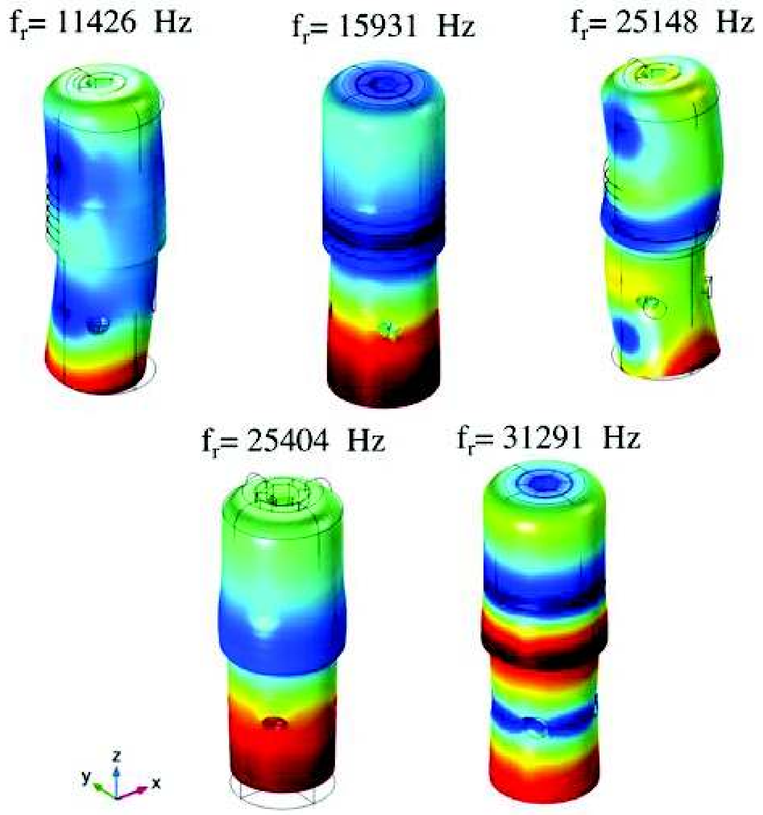

Figure 62: Modal analysis of ultrasonic transducer. The longitudinal vibration mode is obtained for 25404 Hz resonance frequency.

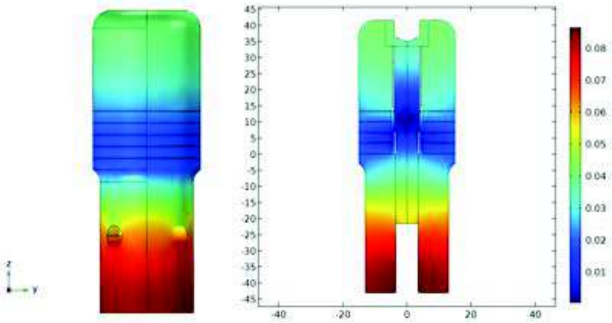

Displacement amplitude [mm]
(f_r = 25404 Hz)

Figure 63: Displacement amplitude of transducer at 25404 Hz. It is shown the amplitude on the outer surface and on a diameter section.

with the digital analyzer. Figure 66 shows the resonance peaks in simulated and acquired electric impedance curves. Further-

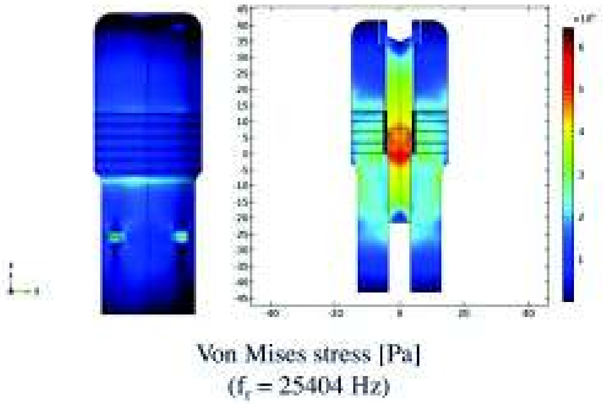

Figure 64: Von Mises stress of transducer at 25404 Hz. It is shown the amplitude on the outer surface and on a diameter section.

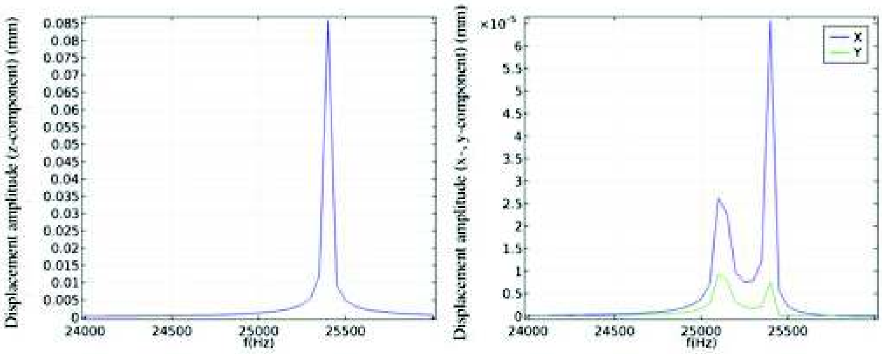

Figure 65: Amplitude displacement components measured at a point of front-mass free face.

more, it is possible to evaluate the resonance frequency for the model of the transducer identifying the frequency values in which occur the minimum peaks, and for the manufactured transducer. The acquired electrical impedance curve is the mean of twenty measuring test. The acquisition set-up is showed in Figure 60: it allows free vibration of free face of front-mass. The transducer was fixed at its nodal plane. From the acquired curve is possible to evaluate the actual resonance frequency f_T as:

$$f_T = 25865 \text{ Hz} \tag{34}$$

Finally, using the Equation 22 an estimation of Q factor for the transduce can be evaluated as (Figure 67):

$$Q_T = \frac{f_T}{\Delta f} \approx 48 \tag{35}$$

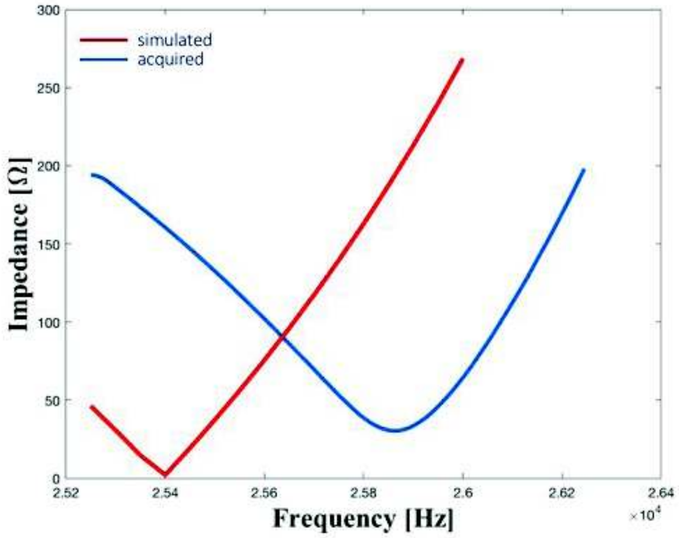

Figure 66: Electric impedance curve of transducer.

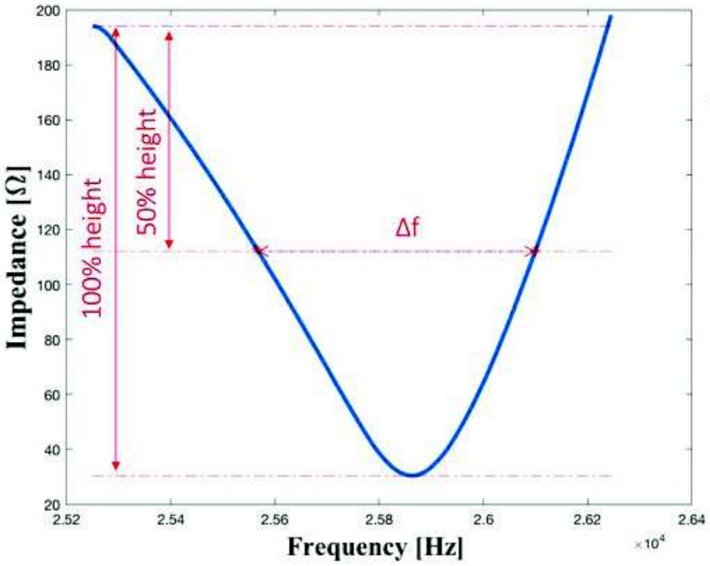

Figure 67: Identification of 50% decrement of the maximum impedance amplitude in acquired electric impedance curve.

4.4.2 Booster

The booster design process started with coping the constraints set by the transducer manufacturing. The constraints include:

- the resonance frequency equal to f_T (25865 Hz);
- booster outer diameter equal to that the front-mass end;
- material properties (Ti6Al4V);

The initial length L_B of the booster is evaluated thanks to Equation 12. In order to find the optimal shape that allows to the booster to vibrate at 25865 Hz longitudinally a modal analysis has been performed. The final tuned design of the booster is reported in Figure 68. The resulting eigenmodes are shown in Figure 69.

Having obtained the desired design for the booster, it was possible to model the assembly that couples transducer and booster. That model allowed to:

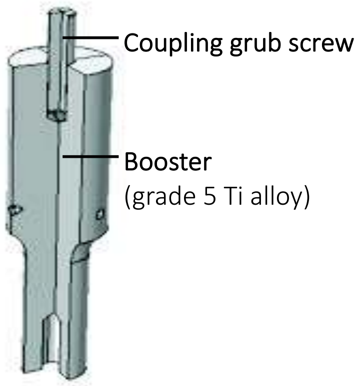

Figure 68: Final design of booster.

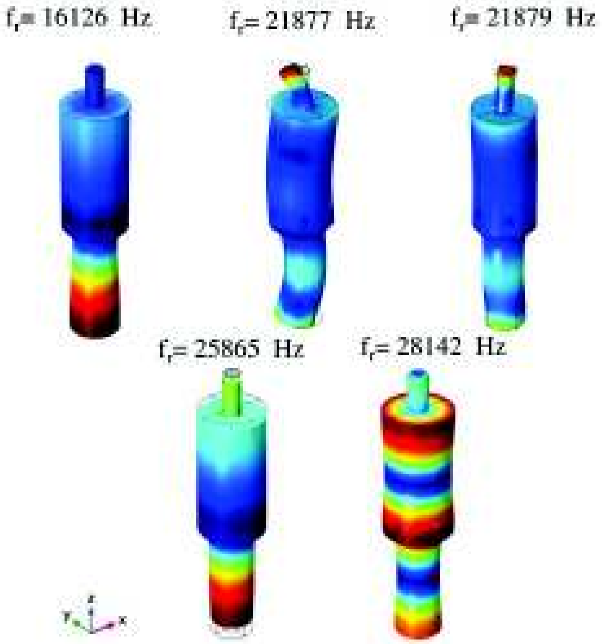

Figure 69: Modal analysis of booster. The longitudinal vibration mode is obtained for 25865 Hz resonance frequency.

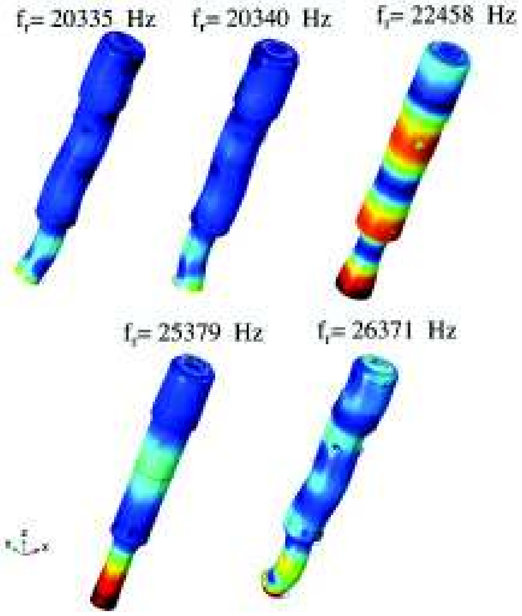

Figure 70: Eigenmodes of partial assembly composed by transducer and booster. Longitudinal vibration occurs at 25379 Hz.

- evaluate the resonance frequency trough the eigenmode assessment obtained by eigenfrequency study.
- conduct a frequency analysis for evaluating the amplitude of the displacements of partial assembly, and verifying the amplification chain had been well designed.
- estimate the Von Mises stress.

The longitudinal vibration mode has been found at f_{STB} equal to 25379 Hz (Figure 70).

The Figure 71 reveals the presence of transverse displacement components at 25379 Hz within the assembly in the $x-$ and $y-$ directions obtained in frequency domain study. However, these components are negligible compared to the displacement in the longitudinal direction.

The stress suffered by the materials does not exceed the limits of the elastic field of materials, as shown in the Figure 72.

Figure 73 shows the resonance peaks in simulated and acquired electric impedance curves. For the partial assembly of ultrasonic drill composed by transducer and booster the acquired resonance frequency occurred at:

$$f_{TB} = 25975 \text{ Hz} \tag{36}$$

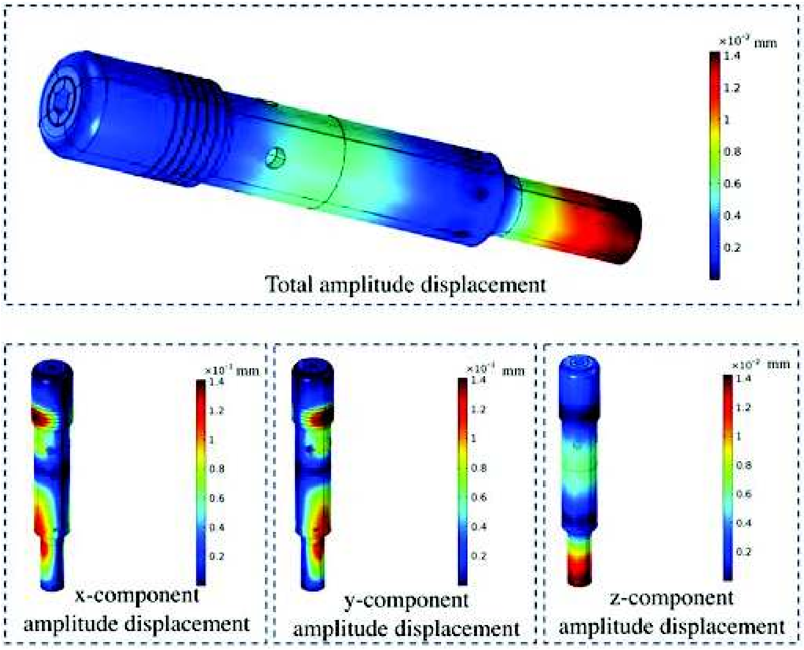

Figure 71: Top) Total displacement amplitude in partial assembly of the ultrasonic drill. Bottom) Cartesian components of displacement amplitude.

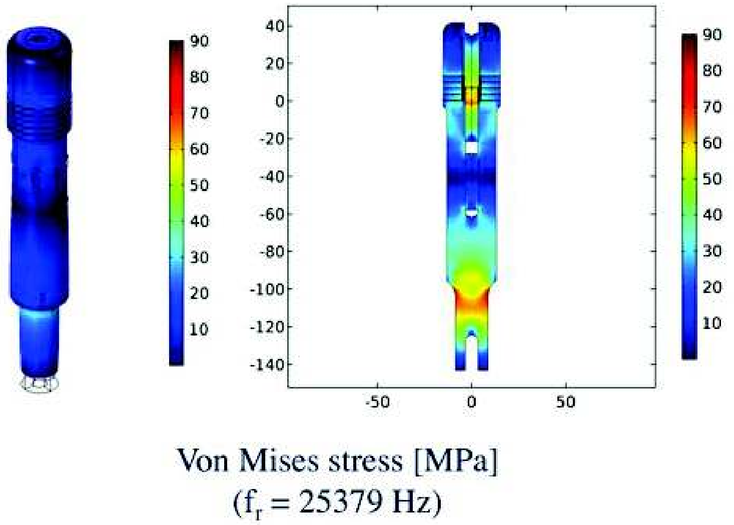

Figure 72: Von Mises stress of partial assembly of the ultrasonic drill at 25379 Hz. It is shown the amplitude on the outer surface and on a diameter section.

and the quality factor Q_{TB}, estimated in acquired electric impedance curve, was:

$$Q_{TB} = \frac{f_{TB}}{\Delta f} \approx 75 \tag{37}$$

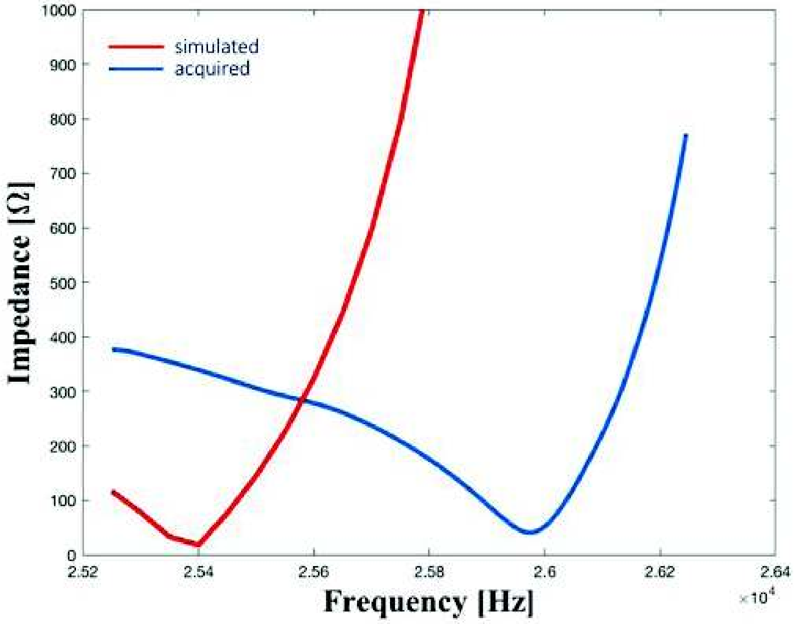

Figure 73: Electric impedance curve of partial assembly of transducer and booster.

4.4.3 Sonotrode

As for the booster, the sonotrode design must take into account:

- that the resonance frequency must be equal to f_{TB} (25875 Hz);
- an end must have outer diameter equal to the booster end;
- the material properties (Ti6Al4V);

The sonotrode length L_S has been set not to half-wave length, rather to the wave length. This is due to the geometrical constraints imposed by the surgery procedures and to the necessity of obtaining a long bony tunnel into the vertebras.

At first, modal analysis has been conducted to design the sonotrode shape for vibrating at 25865 Hz (Figure 75). The final tuned design of the sonotrode is reported in Figure 74.

Finally, after having fixed the geometric shape of the sonotrode, the whole ultrasonic drill has been modeled in COMSOL. As for the intermediate assembly (transducer and booster), the final model allowed to evaluate the resonance frequency trough the eigenmode assessment too, to evaluate the displacement at the tip of the drill and to estimate the Von Mises stress, which condition is verified.

The eigenmode assessment shows the resonance frequency for longitudinal vibration at 24850 Hz, Figure 76 shows the eigenmodes with frequencies close to the longitudinal resonance frequency. The displacement results, obtained in frequency domain analysis, at 24850 Hz are reported in Figure 77. As the

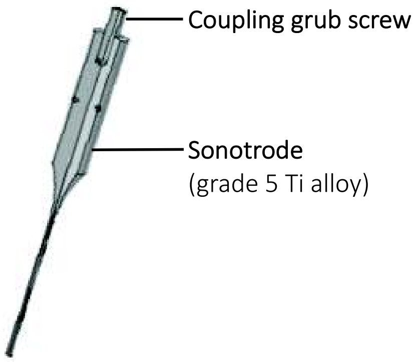

Figure 74: Final design of sonotrode.

partial assembly, the $x-$ and $y-$ components are negligible compared to the displacement in $z-$ direction.

The resistance of the materials is ensured by the results of the stress analysis shown in Figure 78.

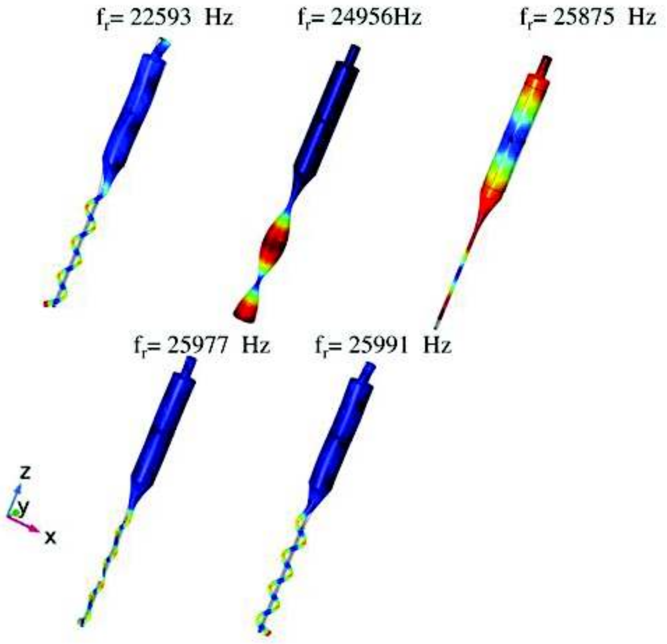

Figure 75: Modal analysis of sonostrode. The longitudinal vibration mode is obtained for 25865 Hz resonance frequency.

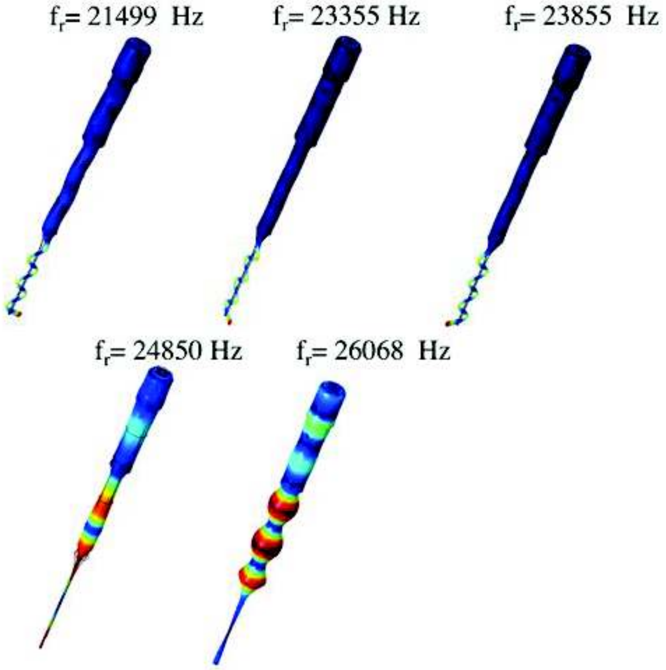

Figure 76: Longitudinal eigenmode at 24850 Hz of ultrasonic drill.

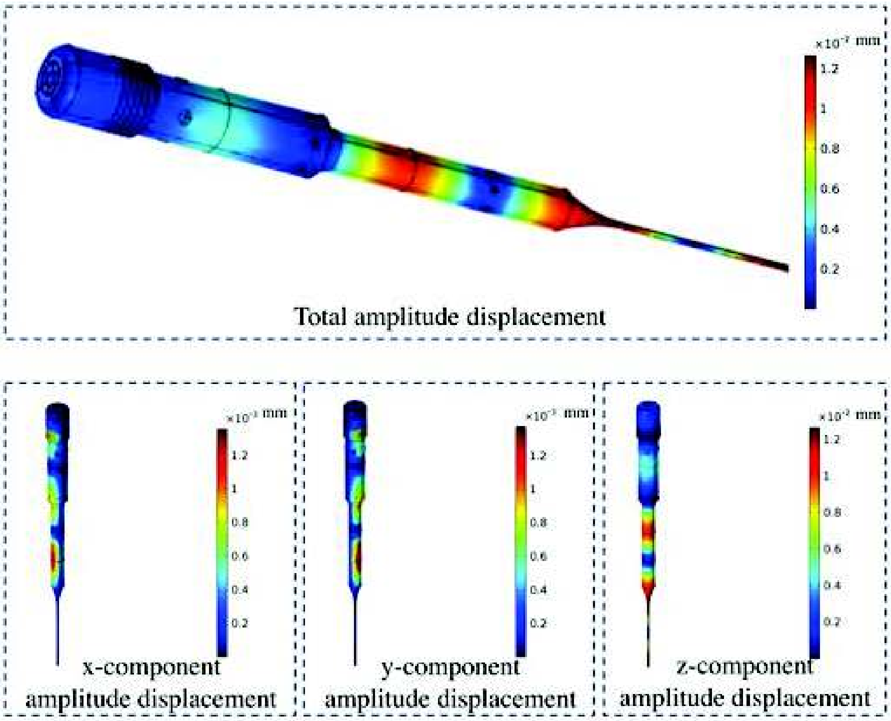

Figure 77: Top) Total displacement amplitude in the ultrasonic drill. Bottom) Cartesian components of displacement amplitude.

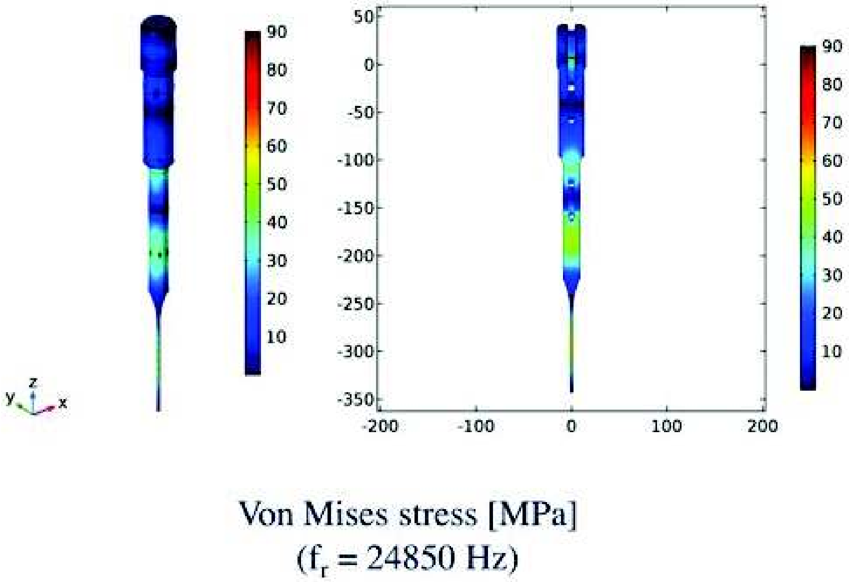

Figure 78: Von Mises stress of the ultrasonic drill at 24850 Hz. It is shown the amplitude on the outer surface and on a diameter section.

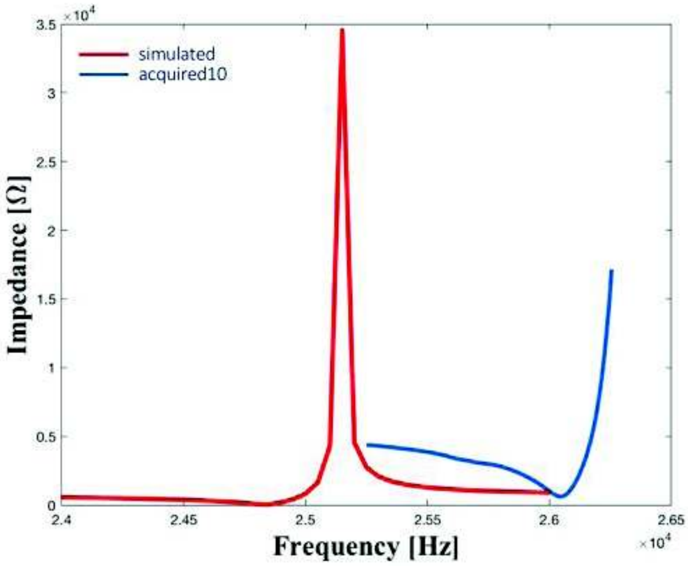

Figure 79: Electric impedance curve of ultrasonic drill.

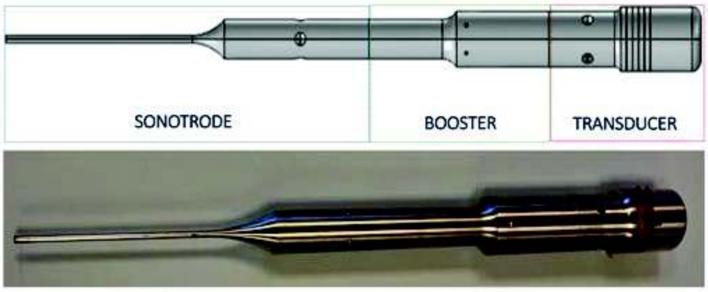

Figure 80: The ultrasonic drill.

After the sonotrode manufacturing, it was possible to complete the assembly and to conduct the acquisition tests for experimentally evaluation of the the resonance frequency by the electrical impedance curve. The Figure 79 shows the curves of the simulated and acquired electrical impedance. The first shows a resonance peak at the 24850 Hz frequency. The resonance frequency occurred at:

$$f_{TBS} = 26042 \text{ Hz} \tag{38}$$

From the curve of the acquired electrical impedance it was finally possible to evaluate the quality factor Q_{TBS} of the whole system equal to:

$$Q_{TBS} = \frac{f_{TBS}}{\Delta f} \approx 96 \tag{39}$$

The final prototype is presented in Figure 80.

4.5 DISCUSSION AND CONCLUSIONS

In this Chapter the principles of ultrasonic system design have been reported. The main principles of wave propagation in simple shape media have been presented. Useful tools for the rough design of ultrasound systems have been obtained from the main theoretical results. Nevertheless, given the intrinsic complexity of ultrasonic systems, these tools are not sufficient for an accurate design. More sophisticated tools for design, such as the finite element method, were presented. Finite element method is a numerical method for solving problems of engineering, typically used for structural analysis, heat transfer, fluid flow, mass transport, and electromagnetic potential. Generally in ultrasonic engineering, the FE method is used only for modal analysis purpose for studying the resonators. The resonators, after being manufactured, are analyzed with experimental systems (e.g. EMA) to measure their performance and to compare the acquired data with the simulated ones, thus measuring the goodness of the simulation. This procedure is widely used and exploited in many literature works. However, it is a design and verification method that requires a lot of instrumentation for the experimental analysis of vibrations, thus increasing the production time of ultrasonic systems. Furthermore, works concerning the design of ultrasonic transducers are very poor.

In this work a design process for ultrasonic systems has been proposed. This process exploits the potential of a simulation software such as COMSOL Multiphysics to design the whole ultrasonic systems, and subsequently to characterize their vibration properties through a single tool that allows the transducer to be powered and to make electric impedance measurements.

The proposed process involves four consequential phases: the first is a rough dimensioning that uses theoretical concepts and tools; the second uses the computational tools proposed by COMSOL Multiphysics for the design of the transducer and resonators (booster and sonotrode). In fact, the adopted software allows to simulate complex problems in which phenomena of different physical domains occur, such as mechanical, electromagnetic and piezoelectric. Thanks to the implementable studies it is possible to estimate the vibratory behavior of the ultrasound system. The third phase requires a lot of accuracy in the realization of the mechanical parts and in their assembly.

Finally, the testing phase is greatly simplified thanks to the use of an ad hoc generator.

The results reported in the previous section show a good agreement between the results of the simulations and the experimental tests. In fact the simulated and acquired resonance frequencies differ at most by 4.8% in case of the complete drill, while it drops to 2.3% in case of the partial assembly (booster and transducer) and to 1.8% in case of the transducer. Furthermore, the eigenfrquency studies conducted give the opportunity to draw operational considerations related for feeding the ultrasonic drill. In particular the results shown in the figures allow to understand the ultrasonic drill supplying frequency range: in fact all the vibrating modes different from the longitudinal ones can have disastrous effects on the drill causing it to break.

Thanks to the acquisition of the impedance curve through the Silence Scope generator it was possible to evaluate the quality factor Q as the ratio between the resonance frequency and the peak band of impedance at 50% of its maximum value. The quality factor Q is a measure of the *"sharpeness"* of the ultrasonic transducer (system) frequency response and it defines the sensitivity of the transducer to change in driving frequency. The vibrations of a transducer with a high Q -factor are "dampened" or significantly reduced when the driving frequency changes very slightly from its resonant frequency. Transducers with low Q-factor continue to vibrate with a considerable portion of their maximum amplitude even if the driving frequency deviates moderately from the resonant frequency, incurring a risk of varying the operating conditions (e.g. the transducer perceives a different load and the resonance frequency changes) thus being driven at harmful frequencies. Furthermore, the maximum ultrasonic output will be achieved when an ultrasonic transducer with high Q-factor is driven precisely at its resonant frequency (see Equation 22). For these reasons, it is useful to verify that the quality factor Q increases during the assembly phase. As shown in Figure 81 the condition has been verified.

It is useful to underline that the simulations from frequency domain studies offer important results for operative purposes. In fact, it is possible to consider the curve shown in Figure 82. That curve represents the absolute value of the longitudinal displacement into the ultrasonic drill. In green three nodal

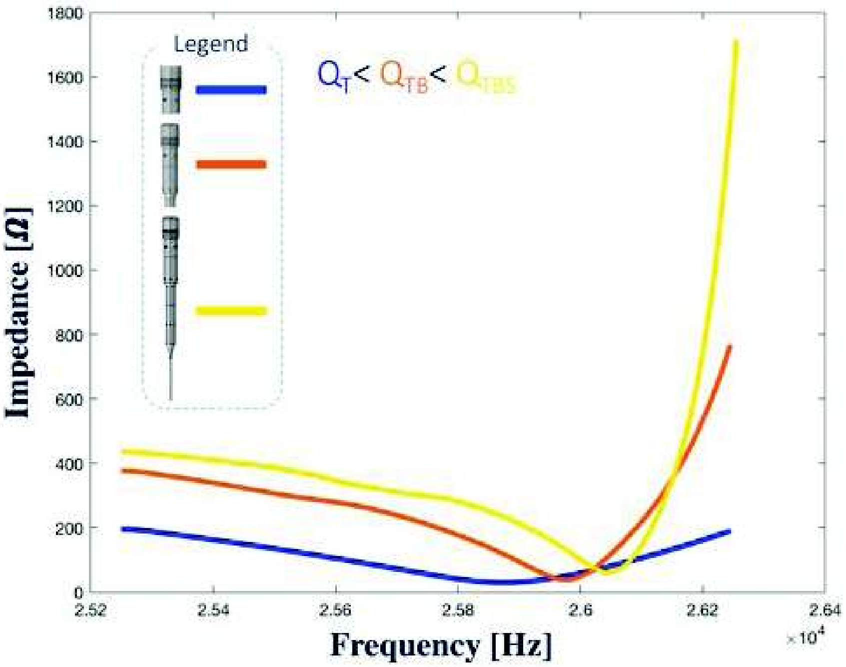

Figure 81: Impedance acquired curve for transducer, partial assembly and ultrasonic drill. It is highlighted the increase of quality factor Q.

points are highlighted. Such informations are essential to design flanges that keep fixed the ultrasonic drill.

The need to design an ultrasonic drill was risen from its intrinsic safety in selectively cutting of only mineralized biological tissues without damages on surrounding soft tissues. In Figure 83 there is a picture of a drilling test on the shell of a fresh egg: it is possible to notice that the soft membrane underneath the shell remains intact.

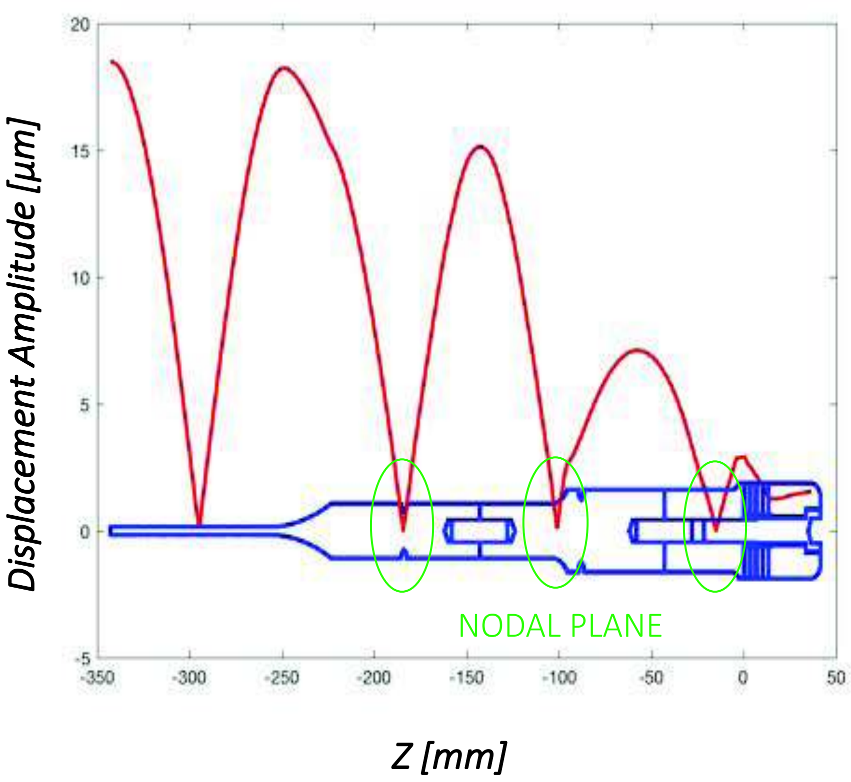

Figure 82: Displacement amplitude along the longitudinal direction of ultrasonic drill.

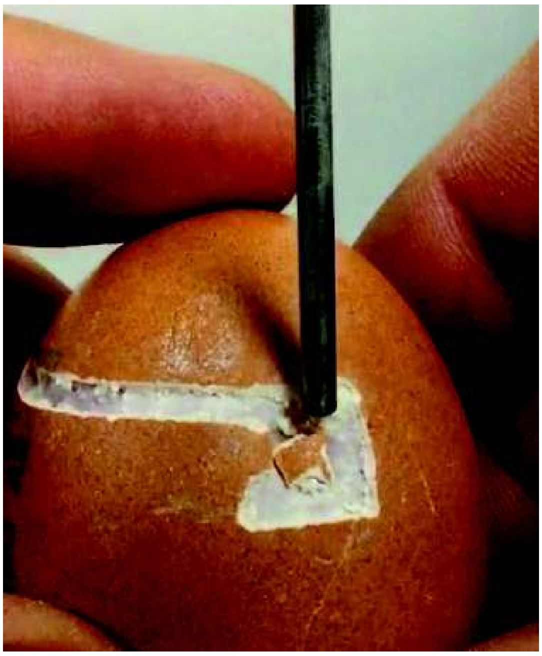

Figure 83: Drilling test on the shell of a fresh egg.

5 SMART DRILLING: BONE IMPEDANCE MEASUREMENTS

The technologies developed in this thesis work, and described in Chapter 2 and Chapter 4, allow the innovative procedure for the treatment of degenerative discopathy (described in Chapter 1) to be generally safer. The safety theme in spinal surgery procedures is of paramount importance and it can be analyzed from two different points of view. The first is about the positioning of the surgical tools in respect to the anatomical sites, for this purpose the surgical positioning system, described in Chapter 2, has been developed. While the second one is about the reduction of bone trauma after the drilling and the minimizing of healthy tissues damages that surround the bone to be treated. This goal can be achieved through the adoption of the ultrasonic drill proposed in Chapter 4.

However, the discussion regarding the safety in spinal procedure, more specifically in the transpedicular one, cannot be solely exhausted by taking these two solutions into account. In fact, different software and hardware solutions for monitoring the drill advancement during drilling has been developed as show in Section 3.3. These methods are based on the acquisition of the thrust force on the drill bit or of the torque exerted for drilling. Nevertheless, the main disadvantage of these techniques is the use of the pushing force generating drill bit advancement as effective signal to discriminate among different bone tissues when the feed rate is constant. In fact, at constant feed rate, the force signal sharply rises during the drilling of the cortical bone, while it falls to lower values as soon as the breakthrough with the medullary cavity occurs.

Therefore, the adoption of these methods is ineffective in the proposed surgical positioning system, where the surgeon can manually control the advancement of the drill bit, thus preserving the haptic feedback that she/he receives from the interaction between the tool and the bone tissues. In [271] a new parameter to address the problem of tissue characterization when neither the force or the feeding rate are constant, nor the force can be limited, as in the case of manual or partially assisted procedures has been proposed.

In order to test the effectiveness of this method based on the estimation of the new parameter, namely Average Impedance, a smart rotative drill, embedded whit force and position sensors, has been developed. The Average Impedance parameter can be used to determine the type of tissue being drilled (i.e. cortical or spongy) as well as to detect the breakthroughs from one bony layer to another.

In this Chapter the implemented bench test on porcine bone models for testing the smart rotative drill and the breakthrough algorithm are described. Then, the results of the estimation of the Average Impedance on vertebrae of human cadaver are discussed. The average impedance measurements on human vertebras are correlated to the bony density evaluated using CT scans.

Furthermore, in order to preserve the clear advantages of the ultrasonic drill in bone machining, the ultrasonic drill has been characterized to be able to be integrated in the average impedance strategy. In particular, the piezoelectric stack in ultrasonic transducer has been exploited for measuring the thrust force exerted by the surgeon during drilling, correlating the output voltage signal with the force signal of the load cell.

5.1 SMART SURGICAL ROTATIVE DRILL

In order to exploit the advantages of manual drillings and the surgeons skills, in addition to the positioning system, a new drilling system and breakthrough detection algorithm have been developed. The proposed breakthrough detection algorithm of drilled tissues is based on the measure of bony mechanical impedance defined by Equation 1:

$$I = \frac{F}{v} \tag{1}$$

where F is the pushing force applied by the surgeon to drill the bone and v is the feed rate of the drill bit crossing the drilled bone.

The drilling platform is comprised of three systems: *i*) a positioning system (PS); *ii*) an end-effector consisting of a custom-made sensorized drilling tool equipped with sensors and *iii*) the control and data processing unit.

5.1.1 End-effector design and sensorized drill

The PS system, described in Chapter 2, allows to mount an end-effector for the manual advancement of the drill, with stable spatial orientation of the drilling trajectory. The PS comprises three sub-modules (Figure 84):

- a 3-DoF mechanical module for rough positioning (MMP) (joints d_0, j_0 and d_1);
- a 2-DoF double planar parallelogram (joints j_{1-8}) that realizes a remote center of motion (RCM) centered on the tip of the surgical tool;
- an end-effector that supports a linear guide (joint d_4) on which the drilling tool can slide (1-DoF).

The end-effector, as shown in Figure 85, is composed by a DELRIN base (1), on which a pulley is mounted (2) (Misumi, Schaumburg, USA, ATP46MXL025-A-NK10). An open-ended belt (3) (Misumi, Schaumburg, USA, TBN-297-MXL-025) drives the pulley and connects two carriages (5) with 4 guide wheels (Shaeffler, Herzogenaurach, Germany, LFL20-SF) each one, which slides along two parallel linear guides (6) (Shaeffler, LFS20). Belt clamps (4) (Misumi, Schaumburg, USA, TBCS-MXL025) are used to lock the belt to the adapters mounted on

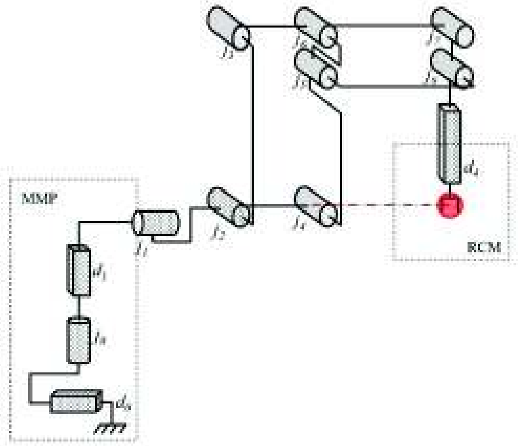

Figure 84: Kinematic structure of the positioning system. The double planar parallelogram realizes a RCM (red dot). Joints d_0, j_0, d_1 j_1, j_2 and d_4 are manually actuated.

the carriages. A 10 bit resolution encoder (8) (RLS, RM22SC10B-10A1B00) is coupled to the pulley in order to measure displacement and feed velocity of the carriages. The two carriages host the surgical tool and a counterweight that balances the weight of the surgical tool and partially of the sensors and power cables.

The coupling between surgical tool/counterweight and carriage has been ensured by the shape of the parts. Indeed an adapter for each carriage has been designed that houses a T-shape nut (10) matching with the complimentary T-shaped groove (7, Figure 86) located on the surgical tool/counterweight. In order to lock or unlock the surgical tool, an indexing plungers has been mounted on the adapter (9); the indexing plungers has a pin that can be retracted acting on an handle allowing the unlock, an easy and quick replacement of the operating tools during the surgical procedure is allowed.

The counterweight has been designed in two parts: a lightweight ABS base housing the T-shaped groove and an heavyweight CuZn39Pb3 brass top part. In this way, depending on the surgical tool mounted, it is possible to balance its weight substituting properly only the top part of the counterweight.

The rotative drill (Figure 86) is composed of an aluminium base (1) (EN AW 6060) with the T-shaped groove (7). The aluminium base houses the flat brushless DC motor (2) (Maxon EC 45, rated power: 50 W) and the bidirectional load cell (4) (Alemanno, TSAMP, measuring range $0-98$ N) on which it is mounted a knob (5). The whole system is covered by a custom

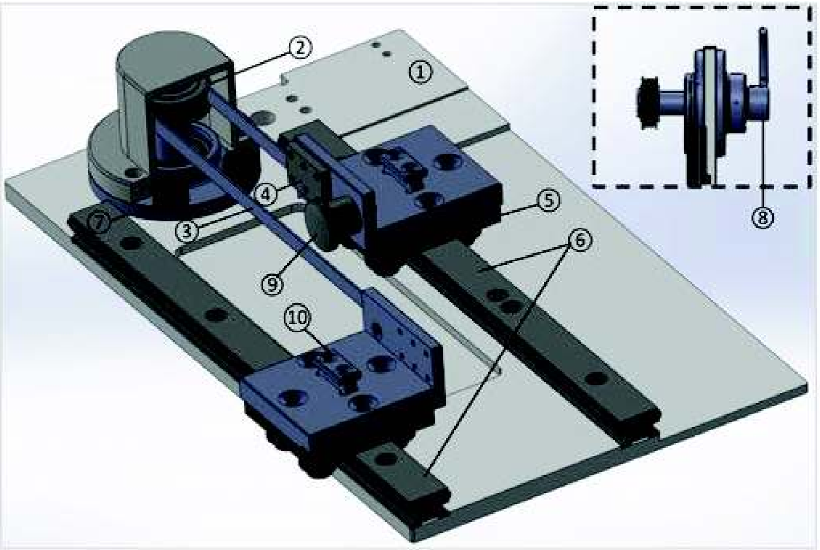

Figure 85: CAD of the end-effector: 1) Base; 2) Pulley; 3) Belt; 4) Belt clamps; 5) Carriage; 6) Linear guide; 7) Stopper bolt; 8) Resolution encoder; 9) Indexing plungers.

3D printed ABS housing case (6). To the motor shaft is attached a chuck (3) (Dremel 4486) that allows interchangeable housing of drill bits with diameters in the range $0.4 - 3.4$ mm. The surgeon can manually advance the driller along the linear guides pushing on the knob, in this way the thrust force is read by the load cell. The main specifications of the rotative drilling system are listed below:

- Feed range (axial direction): $0 - 165.5\,\mathrm{mm}$
- Feed displacement resolution (axial direction): $89.7\,\mu\mathrm{m}$
- Max pushing force (i.e. full scale of the load cell): $98\,\mathrm{N}$
- Rotational speed: $0 - 2360\,\mathrm{rpm}$

The rotative drill control and acquisition system is described in Figure 87. The motor is controlled via a Maxon EPOS2 50/5 unit running PI speed control (1 kHz) to drive the motor at a constant velocity, so that the drill-bit cuts the bone with constant angular speed. Thrust force and angular displacement of pulley are acquired through a National instruments CompactDAQ-9174 (cDAQ), in particular:

- encoder's data are acquired by the cDAQ through a NI9401 digital I/O module (SSI communication protocol). The digital output of the encoder is a 11 bits binary string.

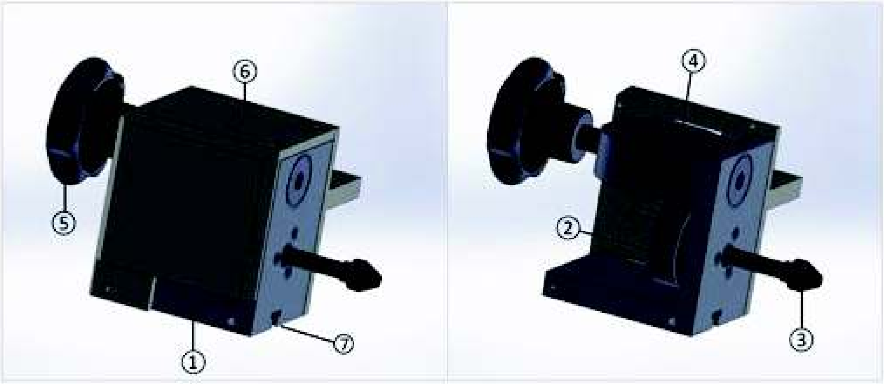

Figure 86: Rotative drill: 1) Base; 2) DC Brushless Motor; 3) Chunk; 4) Load Cell; 5) Knob; 6) 3D printed case; 7) T-shaped groove.

The bit values are acquired at a sampling frequency of 88kHz.

- load cell data are acquired through a NI 9205 16-bit analog input module simultaneously with the reading of the encoder output, therefore force data have a sampling frequency of 88kHz. The output of the load cell is a voltage value in the range ±5V, where positive voltages stand for compression and negative ones for tension. The pass band of the load cell is $[0 - 300]$Hz.

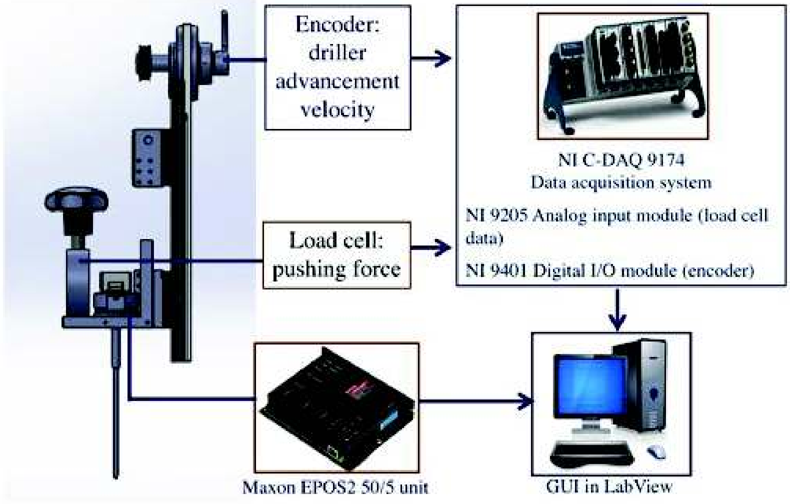

Figure 87: Rotative drill acquisition system.

Figure 88 shows an overall view of the end effector with the mounted drill.

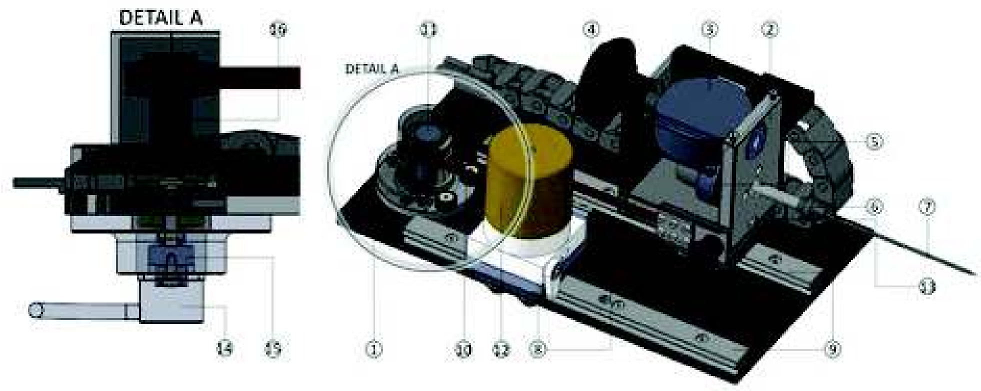

Figure 88: CAD model of the drilling device: 1) DELRIN support; 2) rotary drill EN-AW-6060 Al support; 3) load cell; 4) knob; 5) motor; 6) chuck; 7) Kirschner wire Φ= 2.5mm; 8) carriages; 9) linear guides; 10) belt; 11) pulley; 12) counterweight; 13) T-shaped groove; 14) magnetic encoder stator; 15) magnetic encoder rotor; 16) pulley shaft.

5.1.2 Experimental data acquisition

As shown in Figure 89, the test bench included: *i*) a bone holder and *ii*) the end-effector of the surgical platform clamped in a vertical position. Swine shinbones and ribs were used for the anatomical similarity with human long and short bones [228]. The bones were removed from the cold store 6 hours before the drilling tests and thawed at room temperature. Then the specimens were clamped rigidly into the bone holder. A 2 mm diameter Kirschner wire (rake angle of 12° and clearance angle of 60°), rotating at 2200 rpm was used to drill the bones. Except for the drilling trajectory, constrained by the guide, the drilling procedure has been performed by an expert surgeon at his will without any constraints on the duration of the procedure. Afterwards, in order to validate the results, cross-sections of the shinbones were cut with a cutting plane containing the axis of the cylindrical hole in the bone and the thicknesses of each bone layer was measured using a digital micrometer (Mitutoyo, Absolute Digimatic 500-196-20, Resolution: 10 μm). The linear displacement of the drill and the pushing force were measured during the drilling procedure. Force data are acquired simultaneously with the reading of the encoder output (sampling frequency of 88 kHz). The output of the load cell is a voltage value in the range ±5 V, where positive voltages stand for compression and negative ones for tension. The pass band of the load cell is $0 - 300$ Hz. A 16 bit analog to digital con-

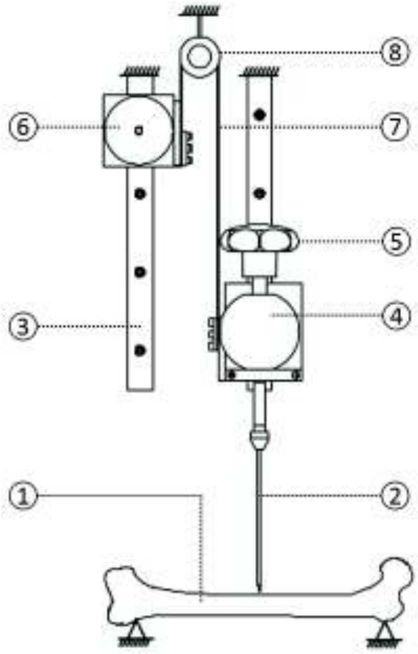

Figure 89: Wire-frame representation of the experimental setup: (1) bone; (2) Kirschner wire; (3) linear guide; (4) load cell; (5) knob; (6) counterweight; (7) belt; (8) pulley.

verter (NI9205, National Instrument, Austin, Texas, US) is used to acquire the force data. In Figure 90 the pushing force F_m measured during a manual drilling on a shinbone has been plotted with respect to the advancement of the drill bit along the linear guide. While drilling at variable velocity, the pushing force is poorly related to the bone layers being drilled. The pushing force during the crossing of the medullary cavity (see region A, Figure 90) may assume values comparable to those obtained in the cortical bone layers (see region B, Figure 90). Furthermore, a drop in the force signal might be due to either a transition from a harder tissue (i.e. cortical bone) to a softer one (e.g. medullary cavity of long bones or cancellous bone) or a momentary decrease in the force exerted by the surgeon during the drilling of the same bone layer. This decrement of the force is not related to the occurrence of a transition. Therefore, in case of manual procedures, the analysis cannot be limited to only the force signal in order to eliminate the risk of misinterpretation.

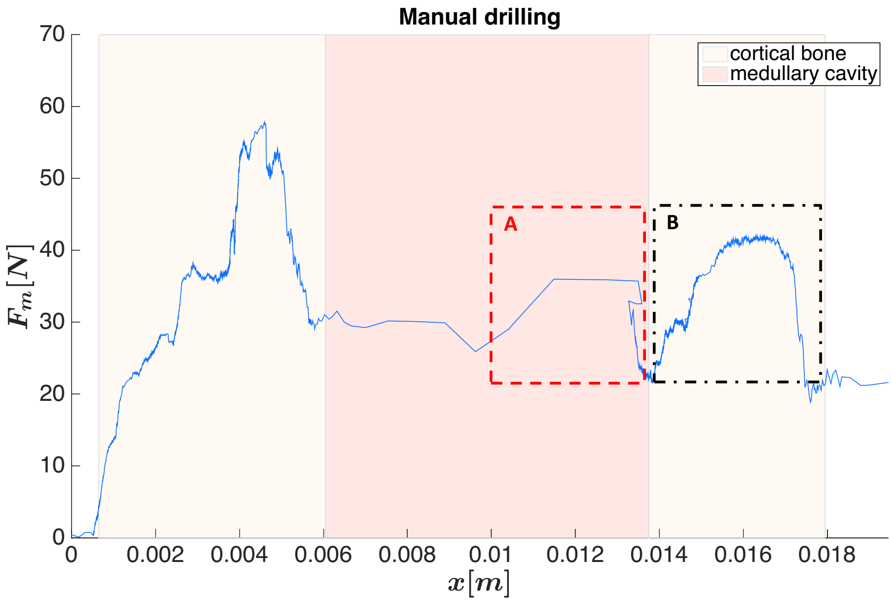

Figure 90: Pushing force characteristic (F_m) during manual drilling of cortical bone tissue and medullary cavity. The magnitude of the pushing force could reach comparable levels in both layers (compare region A with region B).

5.1.3 Average impedance

In view of the above considerations, a new parameter, referred to as Average Impedance (AI), that binds together force and velocity has been introduced. The mechanical impedance of a linear material is defined as (Equation 1)

$$I(f) = \frac{F_d(f)}{v(f)} = \frac{F_d(f)}{2\pi f j S(f)} \tag{2}$$

where $F_d(f)$, $S(f)$ and $v(f)$ respectively are the Fourier transforms of the contact force at the interface (drill bit-tissue), the displacement of the drill bit and its velocity. F_d can be estimated starting from the external (pushing) force F_m, which corresponds to the force read by the load-cell if the inertial effects associated to the motion of the knob are negligible. Denoting with F_f the friction force, m the equivalent translating mass, a the acceleration of the center of mass, δm the unbalanced mass of the assembled system, $\underline{g}$ gravity, and $\underline{\hat{u}}$ the unit vector corresponding to the orientation of the end-effector, the dynamics of the system can be written as:

$$F_m - F_f - F_d + (\delta m)\underline{g} \cdot \underline{\hat{u}} = ma \tag{3}$$

Equation 3 clearly shows that the force signal generated by the load cell is not representative of the actual drilling force: in fact the signal is being affected by both friction and gravitational effects, the latter ones being also pose dependent. To extract information about the pushing force from the measured force, it is necessary to define a parameter, based on the signal provided by the load cell, which is insensitive to both friction and pose-dependent effects.

In order to define new parameters, following the scheme represented in Figure 91, the force and velocity signal has been processed as follow:

- after the application of Fourier Transform to the force signal, it has been filtered with notch filter in order to eliminate the extraneous peaks at multiples of the rotation frequency of DC motor, as they are not associated to the pushing force.

- Both force and velocity signals should be low-pass filtered so that in the evaluation of the impedance only the relevant frequency components of the signals will be taken into consideration while the irrelevant components attributable to noise will be discarded.

- In order to filter out the constant but unknown terms in Equation 3 the DC content has been removed; in this way, F_m can be considered as a valid estimate of F_d insofar the acceleration is sufficiently small.

- Force signal and position signals, from which the velocity is derived in the frequency domain, have been filtered with a 5^{th} order low pass Butterworth filter with cutting frequency $f_c = 50$ Hz.

- Both signals have been resampled at the sampling frequency of $F_s = 4f_c = 200$ Hz.

- At each time instant $\overset{*}{t}$, a causal time window T_w is defined. This time window corresponds to the acquisition of N samples at the sampling frequency F_s;

- Force and displacement data acquired during T_w are Fourier-transformed and $I(f)$ is calculated. $I(f)$ is a function of the frequency. The frequency ranges from $\frac{F_s}{2}$ to $\frac{F_s}{2}$).

- The module $\hat{I}(f)$ of the spectrum is computed: $\hat{I}(f) = \|I(f)\|$.
- $AI(\overset{*}{t})$ is the average of the frequency components of the amplitude $\hat{I}(f)$ taking into account only the positive side of the spectrum up to f_c (i.e. $0 - f_c$) and removing the DC component (i.e. $f = 0$).
- two representations of AI have been considered: $AI(t)$ (Time Referenced Average Impedance: TAI) and AI(x) (Position Referenced Average Impedance: PAI). The last one has been found to be the most significative.

A comparison between the force signal and the PAI signal is shown in Figure 92. It is possible to observe a sudden increase in the force during crossing of the medullary cavity (region A, Figure 92). This increase is not related to changes in the tissues: the inspection of the cross sections of the specimen shows that the drill bit was in the medullary cavity when that increase happened. Therefore that variation of the force is caused by alterations introduced by the operator. Conversely, the corresponding PAI signal is not affected by operator-dependent alterations. Finally, a clear difference in the pattern of the signal is observable between cortical layers (regions B, Figure 92) and medullary cavity (region C, Fig. 92).

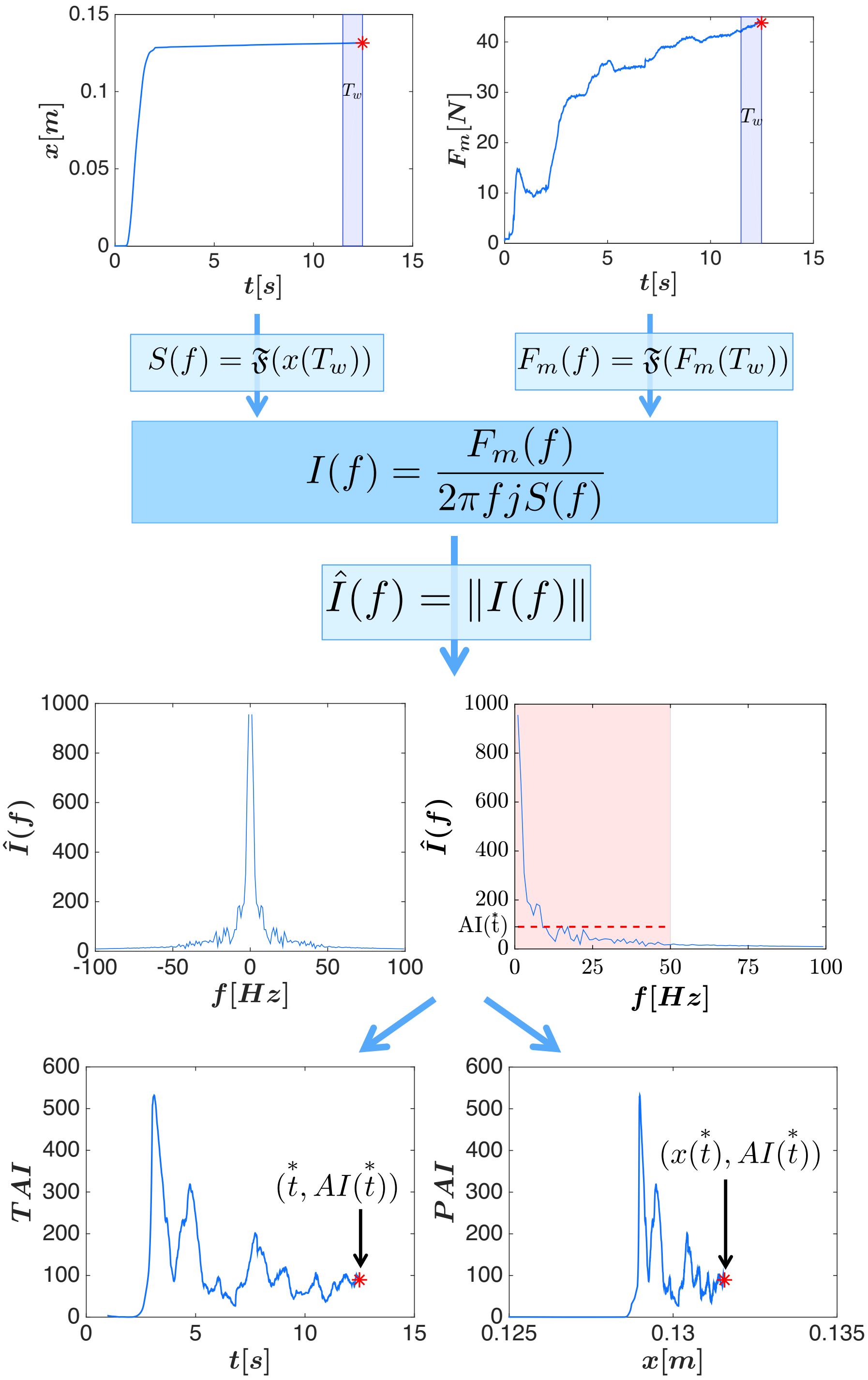

Figure 91: Schematic representation of the data processing through which the parameter AI has been obtained. The time instant t is marked by an asterisk

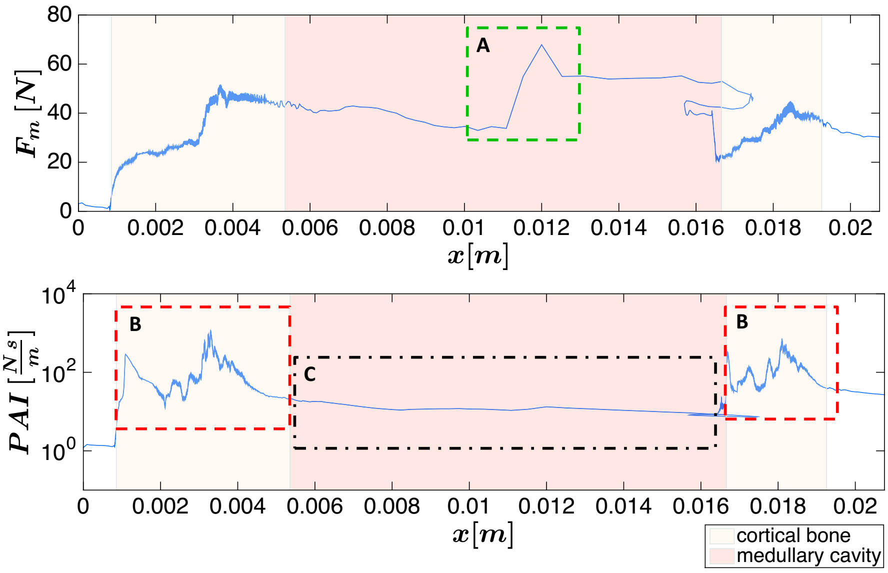

Figure 92: Comparison between PAI and pushing force acquired during a manual drilling in a shinbone.

5.1.4 Layer identification

An algorithm has been developed to inform the surgeon about the occurrence of transitions between layers. The algorithm is based on a sliding spatial window approach.

The following steps have been implemented:

1. once the driller has drilled a portion of cortical bone of length $\bar{L}$, a spatial window W of length $\bar{L}$ is defined;
2. the standard deviation (STD) of $\mathrm{PAI}(x)$ with $x \in W$ is calculated;
3. a new $\bar{L}$-length window is defined after a further driller advancement of $\hat{l}$, the new window is partially overlapped and translated of $\hat{l}$ with respect to the preceding one;
4. the standard deviation of AI on this new window is evaluated;
5. steps 3 and 4 are repeated until the completion of the drilling process.

Taking into account the linear resolution of the measuring system (89.7 μm), the length of the spatial window $\bar{L}$ has been set to 500 μm, while the localization of the drilling tool position is provided every $\hat{l} = 100\ \mu m$.

As a representative example, data obtained during the drilling of a hole in a shinbone specimen have been reported in Figure 93. The STD on each window has been plotted with respect to the advancement distance (Figure 94).

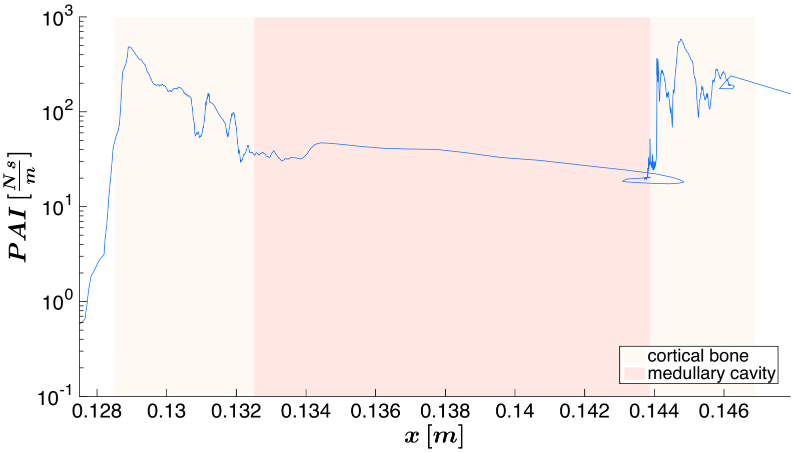

Figure 93: Plot of PAI for a representative drilling.

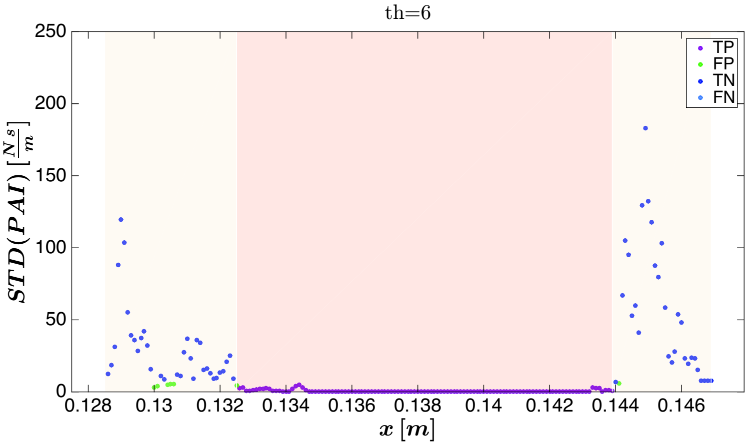

Figure 94: Standard deviation of PAI on sliding windows. Imposing a thresholds (Th = 6), the STD values have been classified taking as positive assumption the positioning in the marrow bone.

It can be noticed that the STD presents higher values during the drilling of the cortical bone, while it assumes lower values elsewhere. In order to discriminate among the bone layers (i.e. cortical bone, cancellous bone or marrow bone), different patterns of STD have been exploited. To this purpose a threshold-based algorithm has been defined. Once a STD threshold value has been chosen, it is possible to evaluate how many correct or incorrect bone portion classifications occur, validating the effectiveness of the algorithm on the base of measurements taken directly from a cross-sections of the shinbone.

It is worth noting that the choice of the right threshold is crucial. For example purposes, in Figure 94 it is shown the choice of the STD threshold Th = 6. This value value influences the number of correct and incorrect bone portion classifications. The PAI signal (Figure 93) is less affected by variable human motion components, which strongly affect the interaction force, and it is more representative of the bone mechanical properties. In fact, the sole force signal is subject to misinterpretations. If only the force is taken into account during a manual procedure, the force in the medullary cavity happens to assume values as high as those in the cortical bone layer. Sudden increases and decreases in the force signal have been found not to be always related to changes in the type of bone layer being drilled, but rather to be generated by non-smooth motions of the operator's hand. Conversely, the PAI signal exhibits the expected tissue-related behavior even in correspondence of force peaks.

The PAI signal appears smoother and with a lower variability in the medullary cavity than in the cortical bone (Figure 93). Exploiting this pattern, an algorithm based on the evaluation of the signal standard deviation on sliding windows has been developed. It is possible to observe (Figure 94) that the values of standard deviation are lower in the medullary cavity than in the cortical bone. The identification of a proper threshold value can allow the discrimination of the drilled tissue. The additional information (PAI) can enhance the bone drilling procedure in terms of accuracy and safety.

5.1.5 Drilling tests on human cadaver vertebrae

After the validation on bench tests, the drilling system has been used for drilling tests on human vertebrae to simulate the transpedicular procedure. In particular, the effectiveness of the drilling system in percutaneous conditions has been proved using a human torso model. The tests were carried out at AO Research Institute (Davos Platz, Switzerland). The experimental set-up comprised (Figure 95):

- the PS equipped with the drilling end-effector, as previously described;
- a C-arm fluoroscope for the pre-operative peduncle identification;
- a torso of a 88 years old male cadaver. Specifically, the human torso model comprised (Figure 96): *i*) the thoracic vertebrae T11-T12; *ii*) the lumbar vertebrae L1-L5 and *iii*) the sacrum. The cadaver was removed from the cold store 12 hours before the tests and thawed at room temperature.

The drilling tests were performed following the steps (Figure 97):

1. the surgeon manually inserted a Kirschner wire ($\Phi = 2.5$ mm) to locate the peduncle, then using C-arm fluoroscopy X-ray images were acquired to verify if the tip of the Kirschner wire was right positioned.
2. The Kirschner wire was attached to the drill chuck. Further images have been acquired to verify the orientation of Kirschner wire and to plan the drilling direction using the algorithm proposed in Chapter 2.

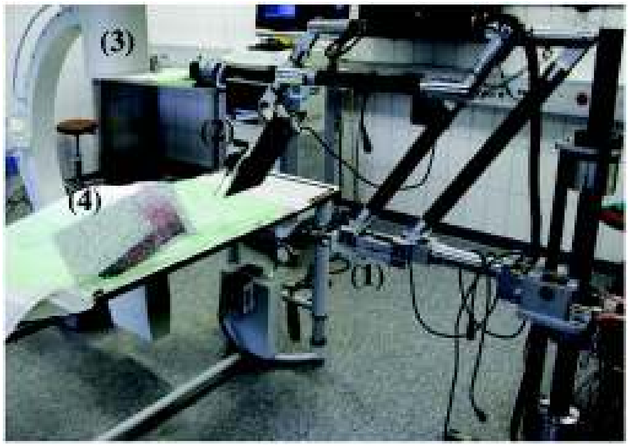

Figure 95: Experimental set up: (1) the positioning system; (2) the drilling end-effector; (3) the C-arm fluoroscope; (4) the human torso.

3. The surgeon drilled the bone applying force on the drill knob. The surgeon was free to perform the drilling procedure at his will without any constrain (regarding the thrust force or the feed rate) on the duration of the procedure. Simultaneously, the thrust force and velocity were acquired with the acquisition system described in Figure 87.

Figure 96: Computer Tomography (CT) of torso of a 88 years old male cadaver.

4. Post-operative CT scans (Siemens CT VA0 COAD, 120 kVp, 330 mA) of the human torso have been performed to evaluate the properties of the bony drilled tunnel. In particular, CT scans have been useful for bony layer identification and the thickness measurements of the different drilled layers (Figure 98).

5. Evaluation of PAI signals, as proposed in Section 5.1.3.

Six different holes were made in the L2-L4 lumbar vertebrae by drilling the right and left peduncles. Of these six acquisitions only four were significant: two tests were excluded from the analysis because during drilling the drill bit broke the medullary canal. Figure 99 shows the evaluated PAI for the drilling test on: *i*) right peduncle of L2; *ii*) right peduncle of L3; *iii*) left peduncle of L3 and *iv*) right peduncle of L4. The drill bit met three different bone layers during drilling perfomances: the cortical bone of the peduncle, the cancellous bone inside the peduncle and finally the cancellous bone that fills the vertebral body. These three different layers are highlighted in Figure 99.

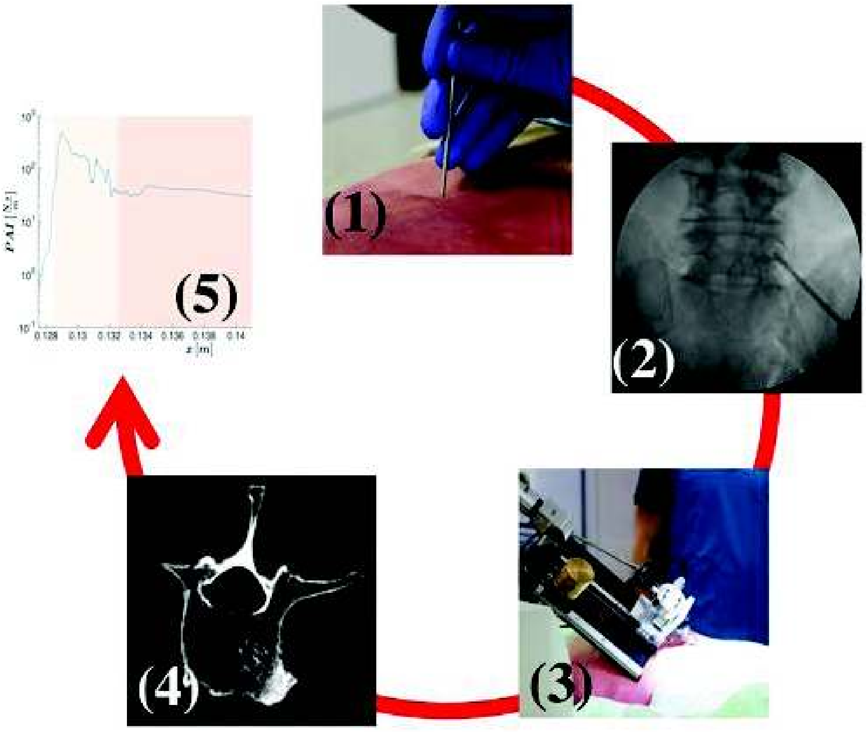

Figure 97: Experimental steps for drilling tests on human cadaver.

Figure 98: Example of length evaluation using OsiriX Lite Dicom Viewer (Pixmeo SARL, Geneva).

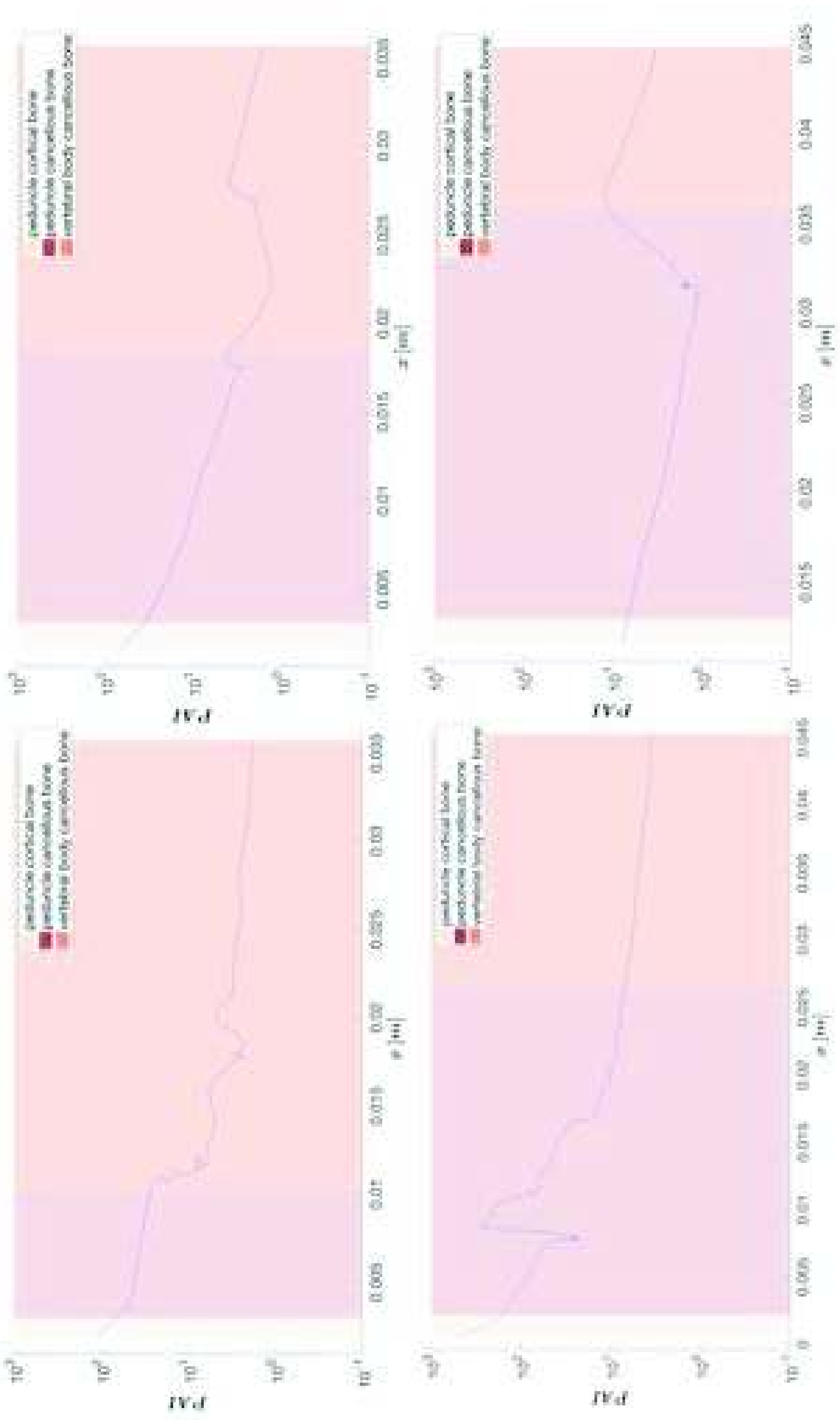

Figure 99: Plot of PAI for: top left) right peduncle of L2; top right) right peduncle of L3; bottom left) left peduncle of L3; bottom right) right peduncle of L4

5.2 BONE STRENGHT EVALUATION

The evaluation of bone strength is useful in a lot of orthopedic procedure, such as spinal fixation, hip, knee or shoulder replacement. In such procedures plates and screws are involved and a damaged bone tissue (e.g. if it is affected by disease such as osteoporosis) can compromises the surgical outcome.

Of huge interest in research is finding the most appropriate technique or method to estimate bone strength in order to enhance the post-operative outcome. In literature two general methods of evaluating bone strength are reported [272, 273]: *i*) the first is based on basic engineering principles which relate the material strength to mechanical properties (e.g. density, Young's modulus, etc) and to loading conditions; *ii*) the second non-invasive method is the bone densitometry through dual-energy X-ray absorptiometry (DXA). Generally, this methods are employed for evaluation of fracture risks.

The determination of the mechanical properties plays an important role in the evaluation of cancellous bone strength and a lot of experimental results are reported in literature. However, it depends on many factors related to the bony specimen and testing condition. Many investigations have been conducted in order to correlate mechanical properties to bone densitometry measurements through DXA method. In densitometry, bone strength can be determined through bone mineral density (BMD) [274, 275, 276].

Bone drilling has also been proposed for the evaluation of bone strength [277, 278]. The estimation of bone strength through drilling allows the surgeons to select appropriate treatment of fracture fixation or to suggest the need for more protective post-operative management [279]. Since bone drilling is largely adopted in different orthopedics procedures, the drilling data can be used for bone strength evaluation.

The use of Hounsfield Units (HUs) from CT scanning to assess regional bone mineral density of the spine has recently been described with several subsequent studies exploring its utility in assessing fracture risk and screening for osteoporosis [280, 281, 282, 283].

In [284] the authors correlate the HUs obtained from clinical CT scans with DXA scores as well as compressive strengths based on osseous models and potentially provide an alternative method for determining regional BMD at no additional cost to the patient.

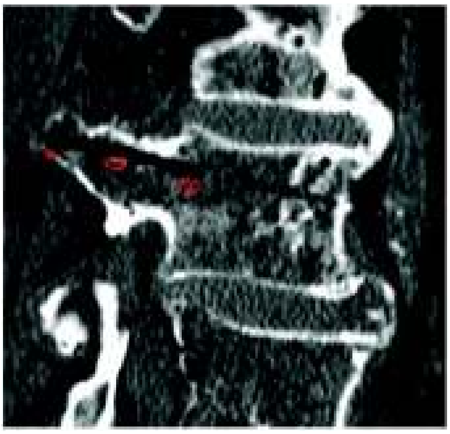

Figure 100: Example of selection of three different regions of interest for measuring Hounsfield units (HU) value. The red ellipses indicate (from left to right): cortical bone of the peduncle, cancellous bone inside the peduncle and vertebral cancellous bone.

In this work the BDM, expressed in the HU scale, evaluated through post-operative CT scans on human cadaver and PAI values, derived after the drilling operations, have been compared.

Hounsfield scale allows a measurement of the standardized linear attenuation coefficient of tissue: water has a null HU value, while air a value of -1000 HU; tissues denser than water have positive values, and tissues less dense than water have negative values [285, 286].

HU can be defined considering a voxel with average linear attenuation coefficient μ, as:

$$HU = 1000 \cdot \frac{\mu - \mu_{water}}{\mu_{water} - \mu_{air}} \tag{4}$$

where μ_{water} and μ_{air} are respectively the linear attenuation coefficients of water and air.

The technique for assessing regional bone mineral density of the bones is very simple using a DICOM images viewer software. In fact, it is possibile to draw a region of interest with simple sketch tools in which only the target bony region is encapsulated. The software calculates the average HU in the region of interest for each image.

The CT section images containing the longitudinal axis of the four significant hole, for which it was possible to evaluate the PAI, were analyzed. For each image it was possible to identify three different regions of interest, corresponding to the

Table 15: PAIs and HUs values of drilling tests on human cadaver.

Drilled tunnel	h_1 [HU]	h_2 [HU]	h_3 [HU]	p_1 (PAI)	p_2 (PAI)	p_3 (PAI)
L2 right	410,8	58,1	11,3	90,4	6,1	2,1
L4 right	439,4	230,92	142,2	7,3	4,4	2,4
L3 right	874,9	58,7	93,6	51,0	6,0	2,2
L3 left	1008,6	197,7	91,7	273,4	67,9	5,8

different type of drilled bone tissue (peduncle cortical bone, peduncle cancellous bone and vertebral cancellous bone) (Figure 100). For each region of interest the average value of HUs was assessed, respectively: h_1 is the HUs mean of cortical bone, h_2 of peduncle cancellous bone and h_3 is the vertebral cancellous bone (values reported in Table 15). Finally, the Δ_{HU} parameter has been defined as:

$$\Delta_{HU1} = 100 \cdot \frac{h_1 - h_2}{h_1} \tag{5}$$

$$\Delta_{HU2} = 100 \cdot \frac{h_1 - h_3}{h_1} \tag{6}$$

In the same way, the means of the PAI in different bone layer have been evaluated, and a new parameter Δ_{PAI}, similarly to Δ_{HU}, has been introduced:

$$\Delta_{PAI1} = 100 \cdot \frac{p_1 - p_2}{p_1} \tag{7}$$

$$\Delta_{PAI2} = 100 \cdot \frac{p_1 - p_3}{p_1} \tag{8}$$

where p_i $\{i = 1, 2, 3\}$ is the PAI means values respectively in peduncle cortical bone, peduncle cancellous bone and vertebral cancellous bone (values reported in Table 15).

The values referred to the same transitions were compared as shown in the histograms in Figures 101 and 102. This comparison was carried out on the four significant holes already specified. It is worth to notice that the difference between the two parameters is always less than 10%. This demonstrates a qualitative correlation between the measured data with the average impedance (PAI) method and the bone mineral density. The results suggest a good correlation between the BDM expressed in HU scale and PAI, and moreover emphasize the possibility of using the new mechatronic drilling system as an in vivo diagnostic tool for the evaluation of bone strength and for

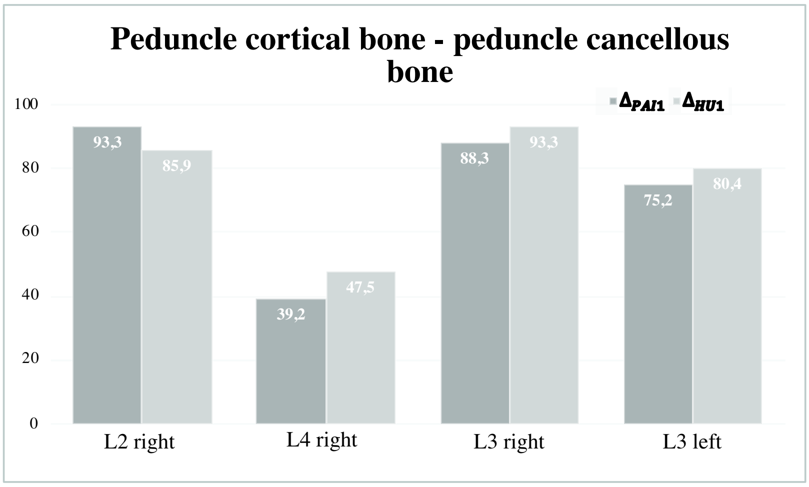

Figure 101: Histograms representing the Δ_{PAI1} and Δ_{HU1} values for different drilled holes.

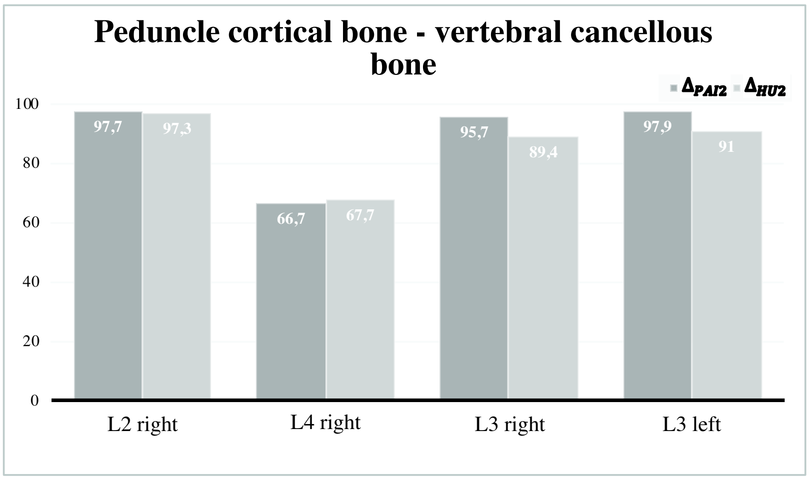

Figure 102: Histograms representing the Δ_{PAI2} and Δ_{HU2} values for different drilled holes.

assisting orthopaedic surgeons in the decision making related to the treatment of a fracture or other pathologies.

5.3 SMART SURGICAL ULTRASONIC DRILL

The new parameter (PAI) has been proposed in order to implement a new breakthrough algorithm for bone layers identification. Such parameter has been introduce considering the traditional bone machining method such as the drilling with rotative drill. As discussed in Chapter 3, this method suffers some disadvantages despite its largely adoption in clinical practice.

In this work a new ultrasonic drill for bony deep holes has been developed in order to reduce the trauma related to bone machining. In this Section, it is shown the feasibility to use the ultrasonic drill in the process for the bone layers breakthrough detection, thanks to its capability of sensing of the thrust force applied during bone drilling. This represents a huge advantage, since:

- all the advantages of the ultrasonic cutting, already described, are assured;
- a single device allows cutting and sensing features simultaneously.

5.3.1 Sensing capability

The active element of ultrasonic drill is the piezoelectric stack, that is composed by four PZT-8 discs. During its operation the ultrasonic drill uses the *inverse piezoelectric effect* to generate the ultrasonic vibration of the system. Such effect is due to the properties of the piezoelectric material that exhibiting a displacement when an electric field on its surface is applied. Generally, this behavior is exploited in the design of piezoelectric actuators. At the same time, piezoelectric sensors exploit the *direct piezoelectric effect*: when a piezoelectric element is subjected to a compressive load, an electrical charge, directly proportional to the applied force, is generated (Figure 103). The piezoelectric sensors have an advantages respect to other sensing techniques in that they are active sensing elements, so that no power supply is needed. Moreover, the necessary deformation to generate a signal is very small, enhancing the sensitivity of the force measures.

Considering the applications where the piezoelectric elements are used as transducer, it is possible to consider the piezoelectric stack as a capacitor, which capacitance is defined as:

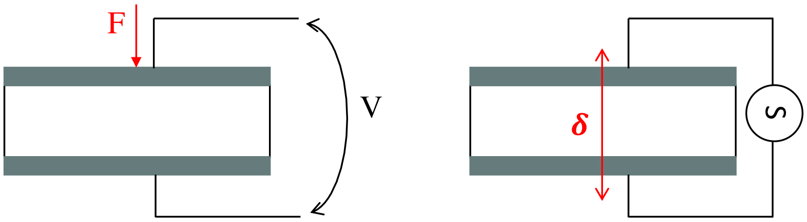

Figure 103: Schematic representation of: left) inverse piezoelectric effect and right) direct piezoelectric effect.

$$C = \frac{\epsilon A}{d} \tag{9}$$

where A is the area plates, that are separated by a uniform gap of thickness d filled with a dielectric with permittivity ϵ. If a force F is applied to the capacitor plates, its capacitance changes. In particular, assuming a force F, equal to $k \cdot x$ (assuming the material between plates is linear elastic), applied to the plates, the gap undergoes to a reduction respect to the nominal distance equal to $\frac{F}{k}$ where k is the spring constant. In this way it is possible re-write the capacitance C, after an applied force, as:

$$C = \frac{\epsilon A}{d - \frac{F}{k}} \tag{10}$$

The last relation can be rearranged as:

$$C = (\epsilon A d + \epsilon A \frac{F}{k}) \cdot \frac{1}{d^2 - \frac{F^2}{k^2}} \tag{11}$$

assuming $d >> x$ and so $d^2 >> \frac{F^2}{k^2}$ it is possible to simplify the last relation in

$$C \simeq (\frac{\epsilon A}{d} + \epsilon A \frac{F}{kd^2}) \tag{12}$$

where the first addendum $(\frac{\epsilon A}{d^2})$ is the nominal capacitance. The capacitance variation, thus can be written as:

$$\Delta C \simeq \frac{\epsilon A F}{kd^2} \tag{13}$$

and the relation with the voltage V is given by the following equation:

$$\Delta V \simeq q \frac{kd^2}{\epsilon A F} \tag{14}$$

where q is the charge on the plates and ΔV is the difference between the feed voltage V_0 and the output voltage V^* measured when a force F is applied to the piezoelectric stack. The measurement of V^* allows to obtain a indirect measure of force F, according to the following equation:

$$V^* \simeq V_0 - q\frac{kd^2}{\epsilon A F} \tag{15}$$

5.3.2 Experimental data acquisitions

The bench test for the characterization of the ultrasonic drill consisted of: *i*) the end-effector previously described with the load cell; *ii*) the ultrasonic drill, described in Chapter 4, anchored to the drill base. The ultrasonic drill was held at the base (1, Figure 86) through a flange designed to surround and tighten the drill in its nodal plane (Figure 104). In all tests performed, multiple masses (each corresponding to a force of 4.7 N) have been applied on the load cell causing advancement of the ultrasonic drill along the guide (Figure 105). The tip of the ultrasonic drill during these tests was pushed on a wood surface (not ultrasonically machinable).

The ultrasonic drill control and acquisition system is described in Figure 106. The piezoelectric drill was supplied by Silence Scope driver, and the signal V^* was measured by the digital multimeter (Agilent 34401A, Keysight Technology) at the ends of a capacitor (3μF, Figure 58). The output force data of the load cell was acquired as previously described (Section 5.1.2). The digital multimeter can read up to 500 readings/second of

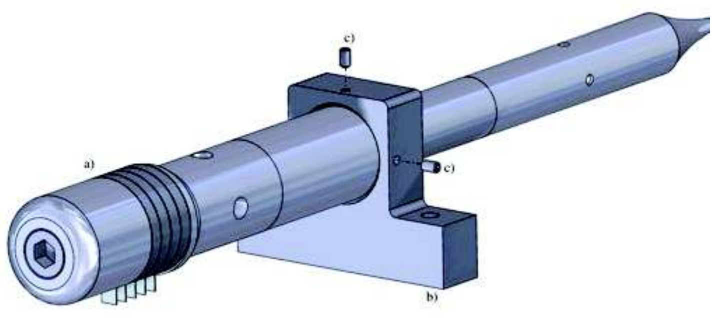

Figure 104: Ultrasonic drill (a) and flange support (b). The ultrasonic drill is assured to the flange through four grub screw (c) at its nodal plane.

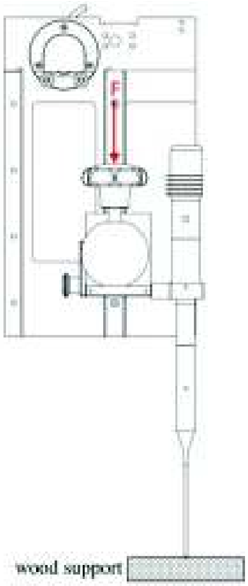

Figure 105: Schematic representation of force F application during tests.

AC input voltage with amplitude up to 1000 V and 3 A max current input.

In Figure 108 a representative voltage V^* curve and the corresponding force F applied to the drill during the acquisition are plotted. The ultrasonic drill was fed in constant current modalities, with current equal to 0.5 A. The two signals have

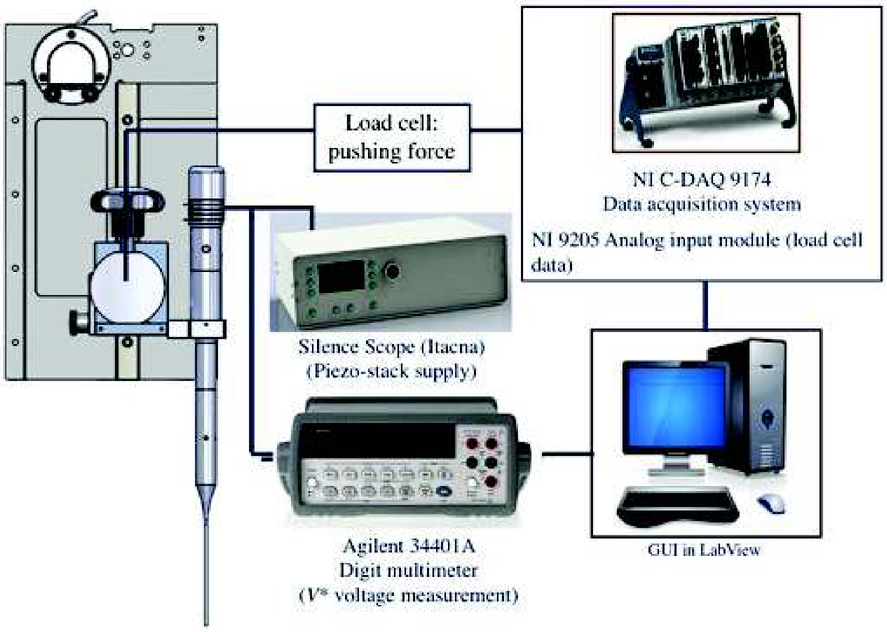

Figure 106: Ultrasonic drill supply and acquisition system.

a different number of sample each other because of different sample rate of their respective acquisition systems. In fact the digital multimeter sets the sample rate considering the input signal frequency. As highlighted in red and blue boxes the signal V^* decreases (A) when the force is applied (B), and it rapidly increases (C) when the load is removed (D). The minimum peaks on the descent front of the signals are caused by the load applied at the moment in which it is placed on the load cell (A and B). This happens especially when low weights are applied to the load cell which is affected by the inertia of the weight-laying gesture on it.

Furthermore, it is possible to notice that the voltage V^* rises during the acquisition. This phenomenon can be addressed to the increase in temperature of the ultrasonic drill and the consequent increase of energy loss (Chapter 4, Equation 21 and 23). In Figure 109 different voltage curves acquired in zero-load condition for different input currents are shown. The Figure

Figure 107: Overview of ultrasonic drill mounted on the end-effector.

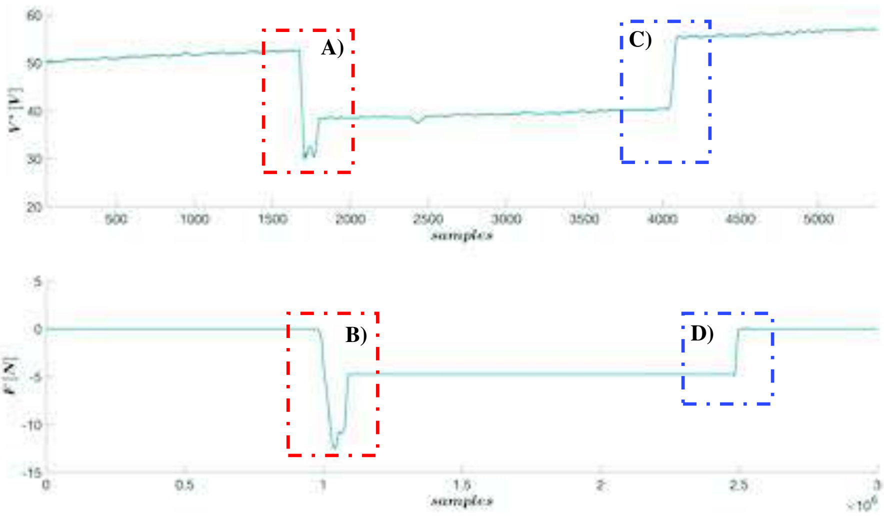

Figure 108: Ultrasonic drill supply and acquisition system.

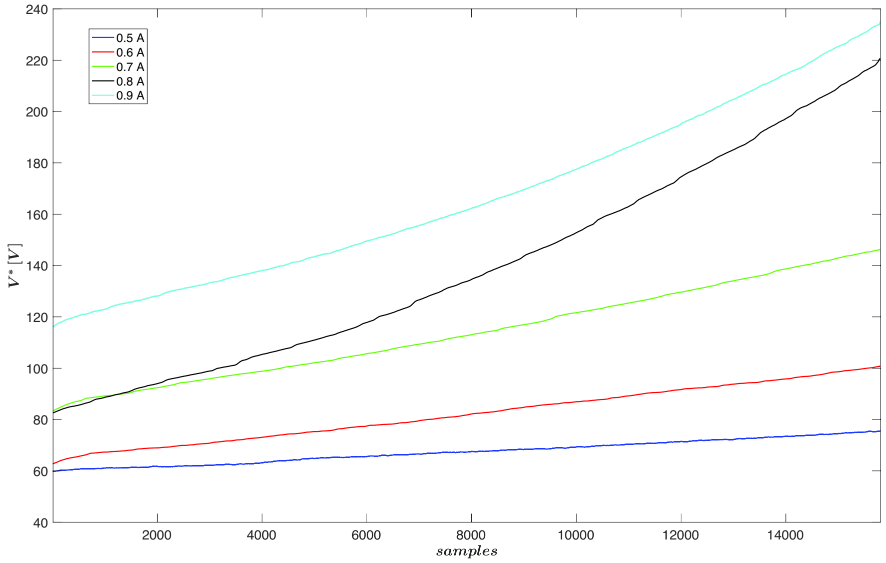

Figure 109: Voltage V* for different input currents.

109 clearly shows higher voltage values as the input current is raised.

5.3.3 Voltage and force signals correlation

In order to correlate the voltage and force signals different tests have been performed. Different loads (4.7 N, 9.4 N and 14.1 N) have been applied to the load cells and, consequently, to the tip of ultrasonic drill. Each test included seven different

Table 16: $\Delta\bar{V}$ values for different tests.

Measurement	$\Delta\bar{V}$ ($F = 4.7$ N) **[V]**	$\Delta\bar{V}$ ($F = 9.4$ N) **[V]**	$\Delta\bar{V}$ ($F = 14.1$ N) **[V]**	$\Delta\bar{V}$ ($F = 18.8$ N) **[V]**
1	3.76	4.67	5.81	6.50
2	4.02	5.06	5.98	7.22
3	4.14	5.16	5.94	7.06
Mean value $\Delta\bar{V}_m$	3.98	4.96	5.91	6.93
Standard deviation	0.19	0.26	0.09	0.38

loading conditions: the data acquisition started with null load and the tip of ultrasonic drill was free to vibrate. After 5 s, the load was applied on the load cell for 5 s and consequently the tip of the ultrasonic drill was pushed against the wood support. Then the load was removed from the load cell for another 5 s and simultaneously the tip of the ultrasonic drill was detached from the support sliding the carriages along the linear guides. In total, the load was applied for three times. The total time of the singe test was 40 s. Figure 110 shows significant curves (V^* for the corresponding F) during the acquisitions. The ultrasonic drill was powered at 0.5 A and a slight temperature-dependent drift occurred in all measurements.

In order to eliminate the dependence of the temperature and to correlate the V^* signal to the force one, a differential measurement was performed. This measure involved the evaluation of $\Delta\bar{V}$ between the average of the 100 samples of the volt signal before load-application and the 100 samples before the load-removal, as shown in Figure 111. For each signal it was possible to evaluate three different $\Delta\bar{V}_i$ $i = \{1, 2, 3\}$ related to the load condition. $\Delta\bar{V}_i$ evaluation was carried out on the four signals shown in the Figure 110. The evaluated values are reported in Table 16.

Figure 112 shows the linear calibration curve between the $\Delta\bar{V}_m$ (average of the three values obtained for each measurement) and the respectively applied force values. The error bars calculated as the standard deviation are also shown.

The coefficients of the linear regression are reported in Figure 112. The value p_1 indicates the sensitivity S of the system:

$$S = \frac{\Delta\bar{V}_m}{\Delta F} = p_1 = 0,21\,\frac{V}{N} \tag{16}$$

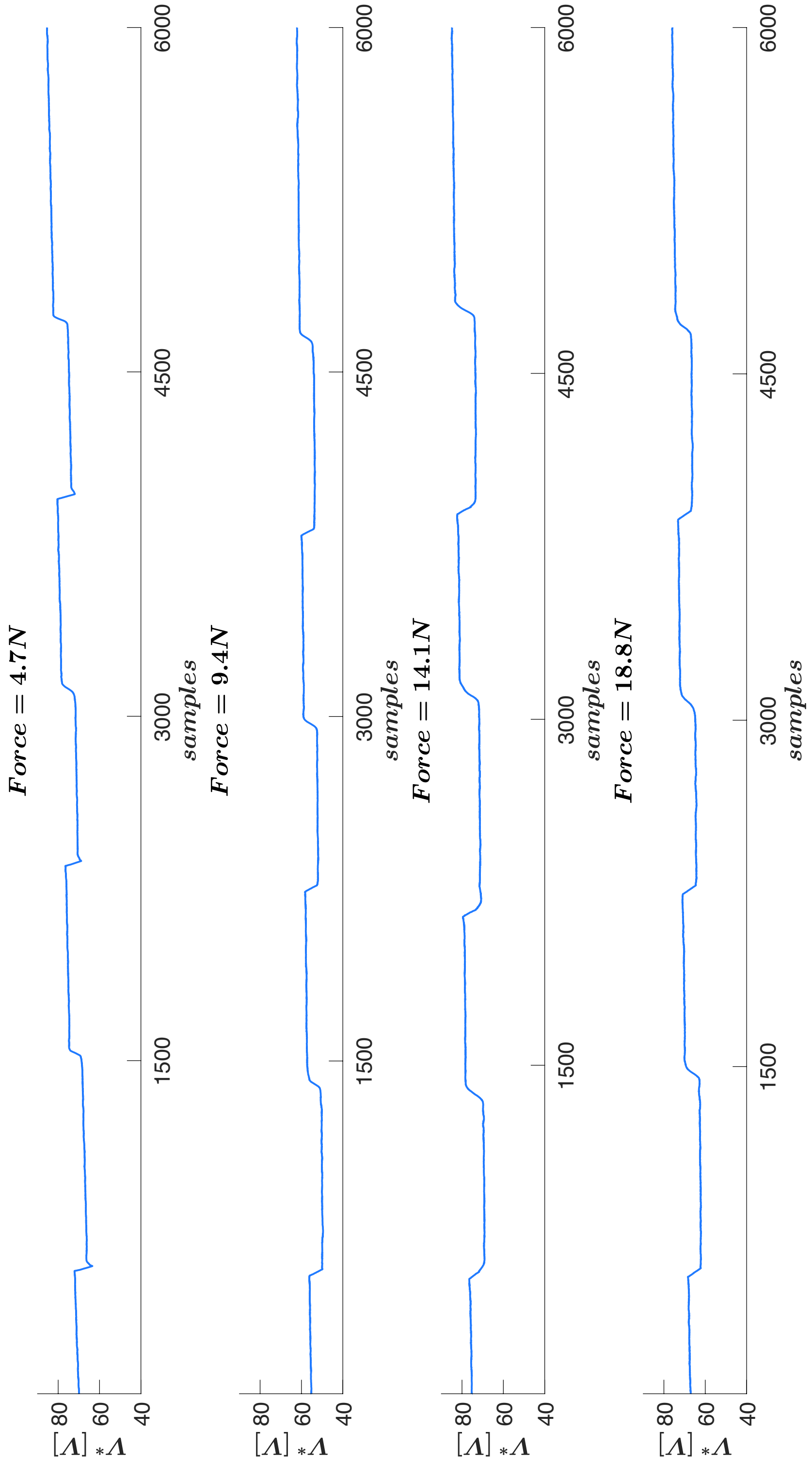

Figure 110: V^* signal for different applied loads.

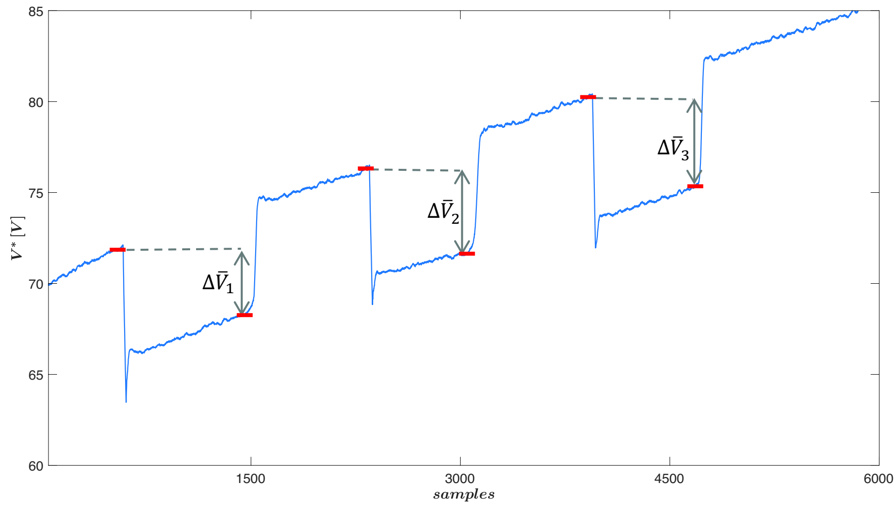

Figure 111: Evaluation of $\Delta\bar{V}$. Red segments are the mean values of 100 sample before the load was applied and than removed. The grey narrow indicate the amplitude of $\Delta\bar{V}$.

Reproducibility can be observed by the error bars and the fact that discrimination among the measured mean $\Delta\bar{V}_m$ values are not disturbed by overlapping standard deviation, being it smaller than the difference calculated between contiguous $\Delta\bar{V}_m$ levels. The good reproducibility of the system can be observed through the values reported in Table 16.

Furthermore, considering the resolution of the digital multimeter as 10^{-2} V it is possible to calculate the resolution R of the piezo-stack as:

$$R = \frac{10^{-2}[V]}{S} = 0,5\,N \tag{17}$$

In order to prove the reproducibility and the reliability of the system, tests with the application of different loads have been performed. Figure 113 shows the V^* signal of a significant test on which nine different loads have been arbitrarily applied to the ultrasonic drill. The loads have been applied for different duration intervals. After the load was removed, the system was allowed a short zero-load period of working. As for the previously described tests, different $\Delta\bar{V}$ have been evaluated. Values are reported in Table 17. It is easy to check that the values shown in the Table 17 fall within the ranges established during the system calibration phase (Table 16).

At the same time, the presence of a constant drift of the signal V^* during the acquisition is clear from the curve shown in the Figure 113. For piezoelectric force measuring devices, measure-

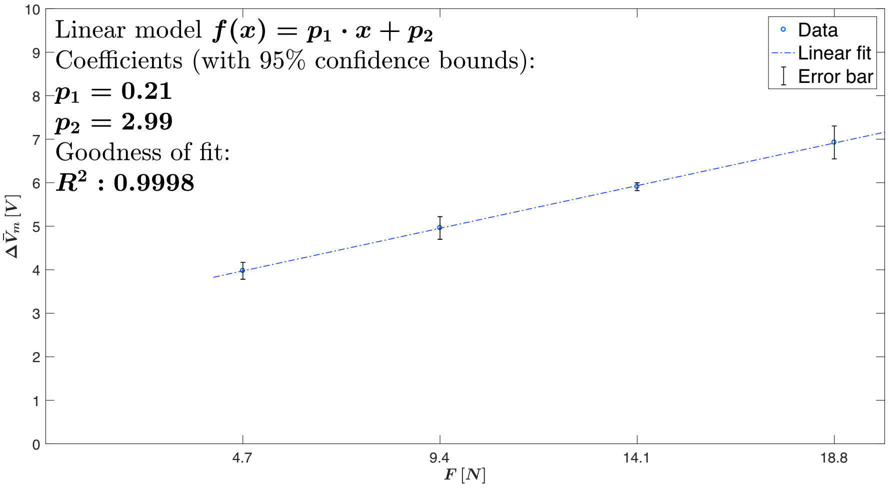

Figure 112: Linear correlation between $\Delta\bar{V}_m$ and F.

ment signal variations due to triboelectric effects and temperature gradients are inherently stochastic and significantly affect the drift. The linear drift, besides, can be caused by a charge accumulation on the piezoelectric stack electrodes, which can be compensated. Due to these stochastic effects a precise and reproducible prognosis of the drift at any time of a measurement is practically impossible.

Furthermore, during acquisition the ultrasonic drill undergoes significant temperature variations for prolonged use. All

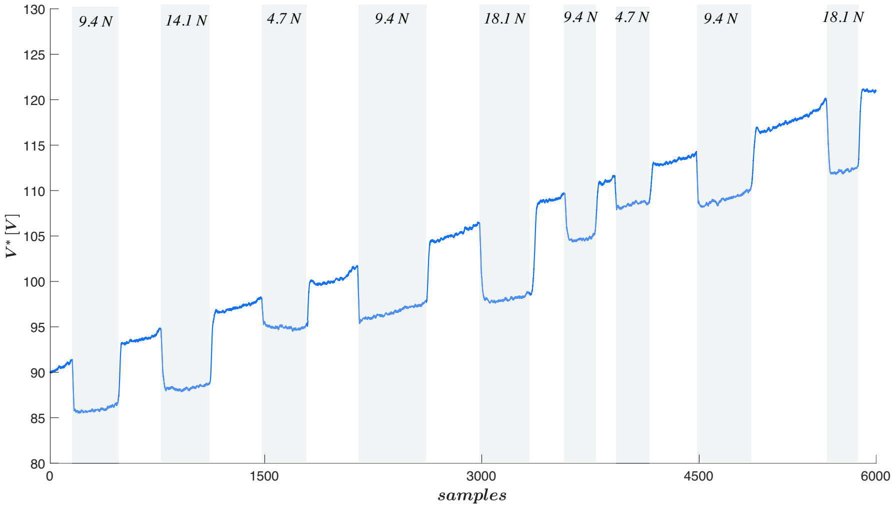

Figure 113: V^* signal acquisition during a test performed with application of different applied loads. The light-grey patches highlight the applications of different loads. The load values are reported.

Table 17: $\Delta\bar{V}$ values for arbitrarily load application test.

$\Delta\bar{V}_1$	4.66 V	$\Delta\bar{V}_4$	4.67 V	$\Delta\bar{V}_4$	3.86 V
$\Delta\bar{V}_2$	5.84 V	$\Delta\bar{V}_5$	7.33 V	$\Delta\bar{V}_4$	4.78 V
$\Delta\bar{V}_3$	3.81 V	$\Delta\bar{V}_6$	4.45 V	$\Delta\bar{V}_4$	7.03 V

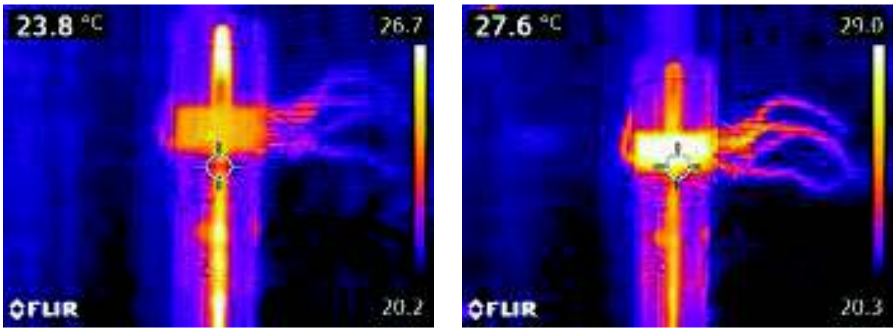

At the beginning of the acquisition. *After 30 s.*

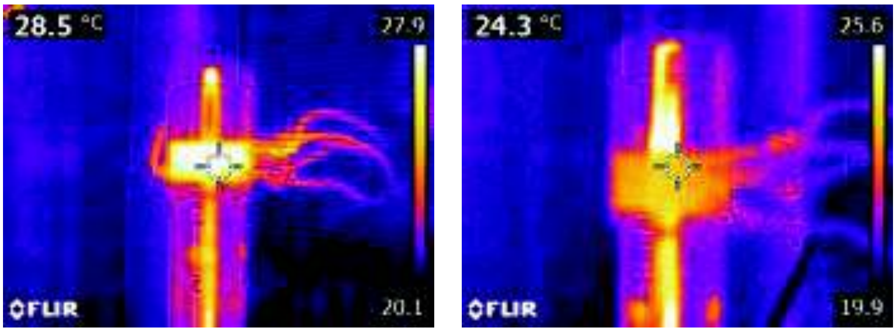

When the drill is switched off (45 s of use) *45 s after turning off the drill.*

Figure 114: Temperature increase during ultrasonic drill operation. These thermo-images have been acquired when 4.7 N load was applied to the ultrasonic drill.

the tests lasted 45 s, and during the acquisitions the temperature was measured using a thermal imaging camera. FLIR E5 (FLIR Systems, Inc., Oregon, US) thermal imaging camera has been used. In Figure 114 it is possibile to see the temperature increase during the operation. It has been proved that after 45 s from the turning off of the drill, the surface temperature returns to a value close to the starting one.

5.4 DISCUSSION AND CONCLUSIONS

In this Chapter two different systems have been proposed to increase safety during the bone drilling operations. As presented in Chapter 3, many efforts have been made to design hardware and software systems to be able to discriminate between the different bone layers during drilling operations. The detection methods described in the literature foresee hypotheses and operating conditions that cannot be adapted to manual drilling systems such as the one proposed in Chapter 2 and 5.

A new parameter, Average Impedance, for the evaluation of the mechanical impedance of the bone tissue has been defined. Based on the variation of the average impedance on a moving position window, an algorithm has been proposed to identify the different bone layers encountered during drilling. The proposed parameter is unaffected by friction variability and it changes in the end-effector orientation. The effectiveness of the proposed approach depends from the proper selection of the thresholds, which could be bone-tissue dependent. Nevertheless, this approach is not conceived to completely substitute the surgeon by means of an automatic drilling system but rather to assist the execution of manual procedures. In conclusion, the additional information (PAI) can enhance the bone drilling procedure in terms of accuracy and safety. Future works will be devoted to the implementation of the detecting algorithm on a real-time system and to the testing of the whole surgical platform on human anatomies.

Drilling tests on human cadaver vertebras have been conducted for the validation of the procedure proposed in Chapter 2 and concurrently for the evaluation of PAI signals on human bone tissues. The results, presented in Figure 99, were obtained thanks to the evaluation of bone thickness by post-operative CT. The evaluation of the thicknesses of the different layers was based on evaluating the bone mineral density of each. The layer identification on CT images has been conducted by expert spine surgeons. By analyzing the results of the PAI curves of the single hole and the corresponding CT images, it was also possible to verify that the new parameter is also able to detect phenomena of vertebral collapse during drilling (Figure 115).

Furthermore, through the CT images it was possible to find a good correlation between the PAI data and the data related to bone mineral density measured in HU. Dimensionless parameters have been built ad hoc to compare the two different

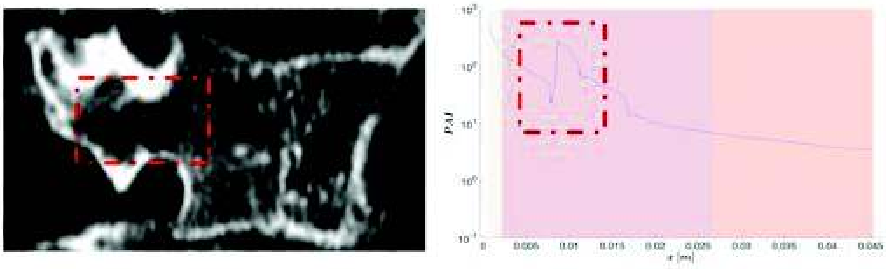

Figure 115: Vertebral collapse during drilling of left L3 peduncle.

types of information showing a difference that is always less than 10%.

Finally, the feasibility of using the ultrasonic drill not only as a drilling tool but also as a sensing tool has been demonstrated. The adoption of this technology would ensure the intrinsic safety respect to the soft tissues (as discussed in the two previous Chapters), but also, thanks to its sensing capability, it could also be used as a tool for evaluating the thrust force applied during drilling operations.

The ultrasonic drill was calibrated by applying known loads on it. The calibration curve shows a linear trend between applied loads and $\Delta\bar{V}$ values. It was also necessary to carry out a differential measurement since the V^* signal in any case shows a drift caused by intrinsic factors to the experimental set up. Temperature is an important parameter to consider when using ultrasound systems with high vibration frequency. A high temperature rise could irreversibly damage the piezoelectric discs, if the Curie temperature was exceeded. The effect of temperature on the treated bone and the surrounding ones should not be underestimated either. It is important to provide an irrigation system thanks to which the temperature of the ultrasonic drill does not increase. It is also important to emphasize that the increase in temperature of the drill during its use can be brought back to the initial value by switching off the system for a time equal to its use. The system as shown in Figure **??** has a good reproducibility. The obtained results confirm the hypothesis of being able to use the drill also as a measuring tool.

6 CONCLUSIONS

6.1 OVERVIEW

This research has demonstrated the significant contribution of mechatronics technology to orthopaedic surgery, in two key areas, associated with the drilling of bone. The two key areas of contribution have been identified as the enhancement of safety and the evaluation of bone characteristics. The enhancement of safety refers to the adoption of ultrasonic drill for creation of deep holes into the bone and the design of a surgical positioning system.

Starting from the engineering challenge of the accurate and safe creation of a single transpedicular bone hole to access to intervertebral disc space, the PhD objectives were design and development of a bone drilling system that enhance safety during drilling and creation of a specific software, as described in Chapter 1.

The proposed PS for orienting the insertion of a surgical cannula during a novel procedure for MISS, is characterized by an unique set of features, which is not exhibited by other solutions. Such features include: a low invasiveness, since no mechanical fixtures onto the bones are necessary; low cost; ease of installation, since the positioning system can be used in any standard or hybrid surgical room equipped with a C-arm. The insertion planning is simply based on the information coming from two perpendicular images (antero-posterior and medio-lateral views) acquired though a C-arm fluoroscope. This approach *i)* avoids the need for multiple landmarks since only the knowledge of the insertion point, identified by the surgeon, is requested thus greatly simplifying the surgical set-up; *ii)* minimizes the radiation dose administered to the subject. In the final prototype a dedicated position sensor will measure the advancement of the drill. In such configuration the couple of initial images is theoretically sufficient to assure the correct positioning of the cannula. Nonetheless, it is possible to expect that few additional images should be acquired for redundancy and safety reasons.

The adoption of the SPS could:

- exploiting technology to transcend human limitations in treating patients;
- improving the safety, consistency and overall quality of interventions;
- improving the efficiency and cost-effectiveness of patient care;

The development of a passive system for driving surgical instruments has been proposed. The choice to design a passive system arises from the fact that orthopaedic or neural surgeons may prefer an assisting device rather than a substituting one in performing surgical procedures. Passive systems preserve the skills of the surgeon, who remains the only supervisor of the surgical tool advancement along a drilling path. The introduction of PS allows a mitigation of tremor during the orientation of surgical drill enhancing the accuracy of drilling trajectory.

The safety enhancement has been gained also with the use of piezoelectric technology for bone drilling. Ultrasonic bone cutting has advantages in controlling tissue damages because it reduces the cutting temperature and associated detrimental after-effects to the bone and it selectively cuts only mineralized tissues, avoiding damages to soft tissues for frequencies in the range of 25 - 35 kHz. In fact, in that frequency range soft tissues can vibrate at the same tool tip frequency without trauma.

Despite its many advantages, piezoelectric surgery still has some drawbacks compared to conventional techniques: it is restricted to minimally invasive surface bone works and does not allow the creation of deep holes as requested in transpedicular approach. For this reason a new ultrasonic drill has been developed. To this aim, a design process for ultrasonic systems has been proposed. This process exploits the potential of a simulation software such as COMSOL Multiphysics to design the whole ultrasonic systems, and subsequently to characterize their vibration properties through a single tool that allows the transducer to be powered and to make electric impedance measurements. The results reported in the previous section show a good agreement between the results of the simulations and the experimental tests. In fact the simulated and acquired resonance frequencies differ at most by 4.8% in case of the complete drill, while it drops to 2.3% in case of the partial assembly (booster and transducer) and to 1.8% in case of the transducer. Furthermore, the proposed process can be clearly applied to the development of systems for different applications, such as welding, cleaning bath and cutting.

The discussion regarding the safety in spinal procedure, more specifically in the transpedicular one, cannot be solely exhausted by taking these two solutions into account. In fact, different software and hardware solutions for monitoring the drill advancement during drilling have been developed. A drilling tool embedded with force and position sensors has been designed and a parameter (named Average Impedance) for the evaluation of the mechanical impedance of the bone tissue has been defined. The end-effector of the surgical platform has been used to perform manual drillings in which the operator manually advances the driller along a predefined path pushing on a knob linked with a load cell. Based on the variation of the average impedance on a moving position window, an algorithm has been proposed to identify the different bone layers encountered during the drilling. It has been possible to conclude that this kind of analyses on the data of thrust force and feed rate can be useful to provide support informations to the surgeon during manual drillings. Nevertheless, this approach is not conceived to completely substitute the surgeon by means of an automatic drilling system but rather to assist the execution of manual procedures.

Tests of proposed surgical procedure and technologies on human cadaver have been performed. The correlation between PAI and HUs has been shown. Dual x-ray absorptiometry (DXA) is currently the standard for assessing bone mineral density and it has been correlated with fracture risk and treatment efficacy. The evaluation of bone strength is useful in a lot of orthopedic procedure, such as spinal fixation, hip, knee or shoulder replacement. In such procedures plates and screws are involved and a damaged bone tissue (e.g. if it is affected by disease such as osteoporosis) can compromises the surgical outcome. The rotative smart drilling system has proved useful to implement breakthrough detection method, and in addition it can provide the surgeon further informations about the the state of health of bones.

Finally, the feasibility of using the ultrasonic drill not only as a drilling tool but also as a sensing tool has been demonstrated. The adoption of this technology would ensure the intrinsic safety respect to the soft tissues, but also, thanks to its sensing capability, it could also be used as a tool for evaluating the thrust force applied during drilling operations. The implementation of a system for bone layers identification has never been proposed using piezoelectric technologies. This study opens new strategies for the drill advancement control.

6.2 FUTURE WORKS

Future works may include the following recommendations:

- Providing the PS with actuated joints in order to allow a quicker positioning, thus shortening the duration of the preoperative phase. In particular, the adoption of actuators with intrinsic elasticity would allow to safely cope with small vertebrae motion. The adoption of Series Elastic Actuators (SEA), such proposed in [287, 288, 289], which include an elastic element, e.g., a torsion spring, placed between the gearmotor and the load, can aid the breath motion issues. Moreover, the actuator was found to be intrinsically backdrivable: this contributes to cope safety aspects to be taken into consideration when designing robots for surgery.

- A system for controlling the temperature increase in ultrasonic drilling. In addition to the temperature raise of the ultrasonic drill, also the cutting site undergoes a significant increase in temperature which can lead to necrosis of the bone tissues. Nowadays, almost all of the orthopaedic instruments use cooling solutions which are pumped into the cut site to reduce temperature and aid debris removal. The application of cooling solution has not been investigated and would undoubtedly reduce cutting temperature even further. Furthermore, the same adopted cooling system could, for example, improve the performance of the drill avoiding voltage drift and allowing a direct correlation between the voltage and force signals after a proper calibration. The cooling system can be designed taking into account a proper fluid pathway, e.g. along the drill axis, with dual action: a continuous irrigation of surgical site and decreasing of the transducer temperature. Finally, also a redesign of the ultrasonic drill tip (sonotrode) in contact with the bone can be implemented in order to decrease the contact area with the bone after the first breakthrough into the cortical layer.

- An ultrasonic drill with coupled vibrating modes (e.g. longitudinal and bending) to optimize the drilling performance during bone cutting. Some authors proposed for bone drilling the combination of the ultrasonic technologies with traditional rotative drills. In this way the ultrasonic effect assisted the drilling procedure allowing some benefits to the biological tissues. However, the damages due to the rotative actions of the drill can not be avoided. New ultrasonic drill components can be designed for operating in a longitudinal-torsional composite mode. This approach has already been demonstrated in a different application, such as the rocks sampling as described in [290, 291, 292, 293].

- Experiments on different bones of different species to prove the correlation between bone mineral density with the PAI and developing a software for minimizing the user-dependant errors during the procedure proposed in Chapter 5, in particular during the identification of the region of interest in CT-scans. Moreover, the bone trabecular orientation can be considered in future work in order to characterize the drilling forces need.

- Acquisition of a large number of voltage and force data during bone drilling with the ultrasonic drill, in order to substitute the voltage signal into the Average Impedance calculation framework. Achieving this result would allow the development of a new mechatronic ultrasonic drilling system for orthopaedic surgery with a control algorithm, able to detect imminent drill bit breakthrough, to provide a controlled penetration.

LIST OF PUBLICATIONS

PUBLISHED

International peer-reviewed journals

Tagliamonte, N. L., Valentini, S., Sudano, A., **Portaccio, I.**, De Leonardis, C., Formica, D., Accoto, D. (2019). Switching Assistance for Exoskeletons during Cyclic Motions. Frontiers in Neurorobotics, 13, 41.

Accoto, D., Rossini, M., Valentini, S., **Portaccio, I.** (2018). A novel sensor for measuring the inner pressure of catheters for clinical use. IEEE Sensors Journal.

Vadalá, G., Russo, F., **Portaccio, I.**, Rossini, M., Valentini, S., Accoto, D., Papalia, R., Denaro, V. (2017). A new surgical positioning system for robotic assisted minimally invasive spine surgery and transpedicular approach to the disc. Journal of Biological Regulators and Homeostatic Agents, 31(4), 159-165.

Valentini, S., **Portaccio, I.**, Accoto, D. (2017). Studying the magnetic stimulation of nervous tissues: A calculation framework to investigate stimulation areas. Medical engineering & physics, 39, 38-48.

Peer-reviewed national and international conference proceedings

Portaccio, I., Valentini, S., Tagliamonte, N. L., Angiolari, A., Russo, F., Papalia, R., Denaro, V., Vadalá, G., Accoto, D. (2016). Design of a positioning system for orienting surgical cannulae during Minimally Invasive Spine Surgery. Biomedical Robotics and Biomechatronics (BioRob), 2016 6th IEEE International Conference on (pp. 476-481). IEEE.

Accoto, D., Valentini, S., **Portaccio, I.**, Guglielmelli, E. (2015). A theoretical frame- work for studying the electromagnetic stimulation of nervous tissue. Engineering in Medicine and Biology Society (EMBC), 2015 37th Annual International Conference of the IEEE (pp. 2079-2082). IEEE.

National and International Conferences/Workshop Abstracts

Portaccio, I., Valentini, S., Tagliamonte, N. L., Russo, F., Papalia, R., Denaro, V., Vadalá, G. and Accoto, D. A novel positioning system for surgical cannulae insertion procedure in spine surgery. Quinto congresso nazionale di Bioingegneria, GNB 2016, Napoli (Italy), June 20-22, 2016.

SUBMITTED

International peer-reviewed journals

Rossini, M., Valentini, S., **Portaccio, I.**, Fasano, A., Accoto, D. Bone tissues identification during surgical drilling. Submitted to Mechatronics.

IN PREPARATION FOR SUBMISSION

International peer-reviewed journals

Portaccio, I., Valentini, S., Rossini, M., Accoto, D. Perspectives on bone surgery: from machining techniques to ultrasonic drilling.

Portaccio, I., Valentini, S., Rossini, M., Accoto, D. A novel ultrasonic drill for spine surgery.

Portaccio, I., Valentini, S., Rossini, M., Accoto, D. Mechatronic surgical platform for spinal procedures.

BIBLIOGRAPHY

[1] Michael A Adams and Peter J Roughley. What is intervertebral disc degeneration, and what causes it? *Spine*, 31(18):2151–2161, 2006.

[2] Gianluca Vadalà, Fabrizio Russo, Girish Pattappa, Damiano Schiuma, Marianna Peroglio, Lorin M Benneker, Sibylle Grad, Mauro Alini, and Vincenzo Denaro. The transpedicular approach as an alternative route for intervertebral disc regeneration. *Spine*, 38(6):E319–E324, 2013.

[3] Kent M Ogden, Can Aslan, Nathaniel Ordway, Dalanda Diallo, Gwen Tillapaugh-Fay, and Pranav Soman. Factors affecting dimensional accuracy of 3-d printed anatomical structures derived from ct data. *Journal of digital imaging*, 28(6):654–663, 2015.

[4] W Korb, R Marmulla, J Raczkowsky, J Mühling, and S Hassfeld. Robots in the operating theatre—chances and challenges. *International journal of oral and maxillofacial surgery*, 33(8):721–732, 2004.

[5] Stephane Lavallee, Jocelyne Troccaz, L Gaborit, Philippe Cinquin, Alim-Louis Benabid, and Dominque Hoffmann. Image guided operating robot: a clinical application in stereotactic neurosurgery. In *Robotics and Automation, 1992. Proceedings., 1992 IEEE International Conference on*, pages 618–624. IEEE, 1992.

[6] Robert Rohling, Patrice Munger, John M Hollerbach, and Terry Peters. Comparison of relative accuracy between a mechanical and an optical position tracker for image-guided neurosurgery. *Journal of image guided surgery*, 1(1):30–34, 1995.

[7] Chin-Hsing Kuo and Jian S Dai. Robotics for minimally invasive surgery: a historical review from the perspective of kinematics. In *International symposium on history of machines and mechanisms*, pages 337–354. Springer, 2009.

[8] Gianluca Vadalà, Francesca De Strobel, Marco Bernardini, Luca Denaro, Domenico D'Avella, and Vincenzo Denaro.

The transpedicular approach for the study of intervertebral disc regeneration strategies: in vivo characterization. *European Spine Journal*, 22(6):972–978, 2013.

[9] Esha Agarwal, Sujata Surendra Masamatti, and Ashish Kumar. Escalating role of piezosurgery in dental therapeutics. *Journal of clinical and diagnostic research: JCDR*, 8(10):ZE08, 2014.

[10] Marcos Louredo, Iñaki Díaz, and Jorge Juan Gil. Dribon: A mechatronic bone drilling tool. *Mechatronics*, 22(8):1060–1066, 2012.

[11] Rumen Kastelov, George Boiadjiev, Tony Boiadjiev, Kamen Delchev, Kazimir Zagurski, and Boyko Gueorguiev. Automatic bone drilling using a novel robot in orthopedic trauma surgery. *Journal of Biomedical Engineering and Informatics*, 3(2):62, 2017.

[12] Kea Alam, AV Mitrofanov, and VV Silberschmidt. Measurements of surface roughness in conventional and ultrasonically assisted bone drilling. *American Journal of Biomedical Sciences*, 1(4):312–320, 2009.

[13] Zensheu Chang, Stewart Sherrit, Xiaoqi Bao, and Yoseph Bar-Cohen. Design and analysis of ultrasonic horn for usdc (ultrasonic/sonic driller/corer). In *Smart Structures and Materials 2004: Industrial and Commercial Applications of Smart Structures Technologies*, volume 5388, pages 320–327. International Society for Optics and Photonics, 2004.

[14] Yoseph Bar-Cohen, Stewart Sherrit, Benjamin P Dolgin, Xiaoqi Bao, Zensheu Chang, Dharmendra Sign Pal, Ron Krahe, Jason Kroh, Shu Du, and Thomas Peterson. Ultrasonic/sonic drilling/coring (usdc) for planetary applications. In *Smart Structures and Materials 2001: Smart Structures and Integrated Systems*, volume 4327, pages 441–449. International Society for Optics and Photonics, 2001.

[15] Yasufumi Hayashi. Classification, diagnosis, and treatment of low back pain. *JAPAN MEDICAL ASSOCIATION JOURNAL.*, 47(5):227–233, 2004.

[16] Richard A Deyo and James N Weinstein. Low back pain affects men and women equally, with onset most often

between the ages of 30 and 50 years. it is the most common cause of work-related disability in people under 45 years of age and the most expensive. *N Engl J Med*, 344(5), 2001.

[17] Anthony R Lanfranco, Andres E Castellanos, Jaydev P Desai, and William C Meyers. Robotic surgery: a current perspective. *Annals of surgery*, 239(1):14, 2004.

[18] Narendra B Dahotre and Sameehan Joshi. *Machining of bone and hard tissues*. Springer, 2016.

[19] Rupesh Kumar Pandey and SS Panda. Drilling of bone: A comprehensive review. *Journal of clinical orthopaedics and trauma*, 4(1):15–30, 2013.

[20] Margaret Lucas and Andrew Mathieson. Ultrasonic cutting for surgical applications. In *Power Ultrasonics*, pages 695–721. Elsevier, 2015.

[21] Dominick A DeAngelis and Gary W Schulze. Performance of pzt8 versus pzt4 piezoceramic materials in ultrasonic transducers. *Physics Procedia*, 87:85–92, 2016.

[22] Bernard Jaffe. *Piezoelectric ceramics*, volume 3. Elsevier, 2012.

[23] Matthew Smuck, Ming-Chih J Kao, Nikhraj Brar, Agnes Martinez-Ith, Jongwoo Choi, and Christy C Tomkins-Lane. Does physical activity influence the relationship between low back pain and obesity? *The Spine Journal*, 14(2):209–216, 2014.

[24] Gunnar BJ Andersson. Epidemiological features of chronic low-back pain. *The lancet*, 354(9178):581–585, 1999.

[25] Theo Vos, Abraham D Flaxman, Mohsen Naghavi, Rafael Lozano, Catherine Michaud, Majid Ezzati, Kenji Shibuya, Joshua A Salomon, Safa Abdalla, Victor Aboyans, et al. Years lived with disability (ylds) for 1160 sequelae of 289 diseases and injuries 1990–2010: a systematic analysis for the global burden of disease study 2010. *The lancet*, 380(9859):2163–2196, 2012.

[26] Jan Hartvigsen, Mark J Hancock, Alice Kongsted, Quinette Louw, Manuela L Ferreira, Stéphane Genevay,

Damian Hoy, Jaro Karppinen, Glenn Pransky, Joachim Sieper, et al. What low back pain is and why we need to pay attention. *The Lancet*, 2018.

[27] Katariina Luoma, Hilkka Riihimäki, Ritva Luukkonen, Raili Raininko, Eira Viikari-Juntura, and Antti Lamminen. Low back pain in relation to lumbar disc degeneration. *Spine*, 25(4):487–492, 2000.

[28] Jeffrey N Katz. Lumbar disc disorders and low-back pain: socioeconomic factors and consequences. *JBJS*, 88:21–24, 2006.

[29] B Peng, W Wu, S Hou, P Li, C Zhang, and Y Yang. The pathogenesis of discogenic low back pain. *The Journal of bone and joint surgery. British volume*, 87(1):62–67, 2005.

[30] Bao-Gan Peng. Pathophysiology, diagnosis, and treatment of discogenic low back pain. *World journal of orthopedics*, 4(2):42, 2013.

[31] James Dowdell, Mark Erwin, Theodoe Choma, Alexander Vaccaro, James Iatridis, and Samuel K Cho. Intervertebral disk degeneration and repair. *Neurosurgery*, 80(3S):S46–S54, 2017.

[32] Gail M Jensen. Biomechanics of the lumbar intervertebral disk: a review. *Physical therapy*, 60(6):765–773, 1980.

[33] Jeremy Simon, Matthew McAuliffe, Fehreen Shamim, Nancy Vuong, and Amir Tahaei. Discogenic low back pain. *Physical Medicine and Rehabilitation Clinics*, 25(2):305–317, 2014.

[34] V Denaro, R Papalia, L Denaro, A Di Martino, and N Maffulli. Cervical spinal disc replacement. *The Journal of bone and joint surgery. British volume*, 91(6):713–719, 2009.

[35] Sandra Reitmaier, Uwe Wolfram, Anita Ignatius, Hans-Joachim Wilke, Antonio Gloria, José M Martín-Martínez, Joana Silva-Correia, Joaquim Miguel Oliveira, Rui Luis Reis, and Hendrik Schmidt. Hydrogels for nucleus replacement—facing the biomechanical challenge. *journal of the mechanical behavior of biomedical materials*, 14:67–77, 2012.

[36] Alberto Di Martino, Alexander R Vaccaro, Joon Yung Lee, Vincenzo Denaro, and Moe R Lim. Nucleus pulposus replacement: basic science and indications for clinical use. *Spine*, 30(16S):S16–S22, 2005.

[37] Lluis Orozco, Robert Soler, Carles Morera, Mercedes Alberca, Ana Sánchez, and Javier García-Sancho. Intervertebral disc repair by autologous mesenchymal bone marrow cells: a pilot study. *Transplantation*, 92(7):822–828, 2011.

[38] Sebastião van Uden, Joana Silva-Correia, Joaquim Miguel Oliveira, and Rui Luís Reis. Current strategies for treatment of intervertebral disc degeneration: substitution and regeneration possibilities. *Biomaterials research*, 21(1):22, 2017.

[39] James C Iatridis, AJ Michalek, D Purmessur, and CL Korecki. Localized intervertebral disc injury leads to organ level changes in structure, cellularity, and biosynthesis. *Cellular and molecular bioengineering*, 2(3):437–447, 2009.

[40] Dawn M Elliott, Chandra S Yerramalli, Jesse C Beckstein, John I Boxberger, Wade Johannessen, and Edward J Vresilovic. The effect of relative needle diameter in puncture and sham injection animal models of degeneration. *Spine*, 33(6):588–596, 2008.

[41] Mauro Alini, Stephen M Eisenstein, Keita Ito, Christopher Little, A Annette Kettler, Koichi Masuda, James Melrose, Jim Ralphs, Ian Stokes, and Hans Joachim Wilke. Are animal models useful for studying human disc disorders/degeneration? *European Spine Journal*, 17(1):2–19, 2008.

[42] Casey L Korecki, John J Costi, and James C Iatridis. Needle puncture injury affects intervertebral disc mechanics and biology in an organ culture model. *Spine*, 33(3):235, 2008.

[43] Eugene Carragee, Angus Don, Eric L Hurwitz, Jason Cuellar, John Carrino, and Richard Herzog. Does discography cause accelerated progression of degeneration changes in the lumbar disc: A ten-year cohort-controlled study. *The Spine Journal*, 9(10):4S, 2009.

[44] Gianluca Vadalà, Gwendolyn Sowa, Mark Hubert, Lars G Gilbertson, Vincenzo Denaro, and James D Kang. Mesenchymal stem cells injection in degenerated intervertebral disc: cell leakage may induce osteophyte formation. *Journal of tissue engineering and regenerative medicine*, 6(5):348–355, 2012.

[45] GW Omlor, H Bertram, K Kleinschmidt, J Fischer, K Brohm, T Guehring, M Anton, and Wiltrud Richter. Methods to monitor distribution and metabolic activity of mesenchymal stem cells following in vivo injection into nucleotomized porcine intervertebral discs. *European Spine Journal*, 19(4):601–612, 2010.

[46] Gianluca Vadalà, Fabrizio Russo, Alberto Di Martino, and Vincenzo Denaro. Intervertebral disc regeneration: from the degenerative cascade to molecular therapy and tissue engineering. *Journal of tissue engineering and regenerative medicine*, 2013.

[47] David Eglin, Sibylle Grad, Sylwester Gogolewski, and Mauro Alini. Farsenol-modified biodegradable polyurethanes for cartilage tissue engineering. *Journal of Biomedical Materials Research Part A: An Official Journal of The Society for Biomaterials, The Japanese Society for Biomaterials, and The Australian Society for Biomaterials and the Korean Society for Biomaterials*, 92(1):393–408, 2010.

[48] MW Laschke, A Strohe, MD Menger, M Alini, and D Eglin. In vitro and in vivo evaluation of a novel nanosize hydroxyapatite particles/poly (ester-urethane) composite scaffold for bone tissue engineering. *Acta biomaterialia*, 6(6):2020–2027, 2010.

[49] Nicky Bertollo and William Robert Walsh. Drilling of bone: practicality, limitations and complications associated with surgical drill-bits. In *Biomechanics in Applications*. InTech, 2011.

[50] Peyman Pakzaban. Bonescalpel$^{\text{TM}}$ ultrasonic bone dissector: Applications in spine surgery and surgical technique guide. *Farmingdale, New York: Misonix*, 2014.

[51] Zoran Pandilov and Vladimir Dukovski. Comparison of the characteristics between serial and parallel robots. *Acta Technica Corvininesis-Bulletin of Engineering*, 7(1), 2014.

[52] Peter Kazanzides, Brent D Mittelstadt, Bela L Musits, William L Bargar, Joel F Zuhars, Bill Williamson, Phillip W Cain, and Emily J Carbone. An integrated system for cementless hip replacement. *IEEE Engineering in Medicine and Biology Magazine*, 14(3):307–313, 1995.

[53] Shimon Y Nof. *Handbook of industrial robotics*, volume 1. John Wiley & Sons, 1999.

[54] Yoram Koren and Yoram Koren. *Robotics for engineers*, volume 168. McGraw-Hill New York et al, 1985.

[55] Russell H Taylor, Arianna Menciassi, Gabor Fichtinger, Paolo Fiorini, and Paolo Dario. Medical robotics and computer-integrated surgery. In *Springer handbook of robotics*, pages 1657–1684. Springer, 2016.

[56] Russell H Taylor and Dan Stoianovici. Medical robotics in computer-integrated surgery. *Robotics and Automation, IEEE Transactions on*, 19(5):765–781, 2003.

[57] Mike Minh Nguyen and Sakti Das. The evolution of robotic urologic surgery. *Urologic Clinics*, 31(4):653–658, 2004.

[58] Garth H Ballantyne. Robotic surgery, telerobotic surgery, telepresence, and telementoring. *Surgical Endoscopy and Other Interventional Techniques*, 16(10):1389–1402, 2002.

[59] Anthony M DiGioia, Branislav Jaramaz, and Bruce D Colgan. Computer assisted orthopaedic surgery: Image guided and robotic assistive technologies. *Clinical orthopaedics and related research*, 354:8–16, 1998.

[60] Charlotte Tsui, Rachel Klein, and Matthew Garabrant. Minimally invasive surgery: national trends in adoption and future directions for hospital strategy. *Surgical endoscopy*, 27(7):2253–2257, 2013.

[61] Michael J Mack. Minimally invasive and robotic surgery. *Jama*, 285(5):568–572, 2001.

[62] Wen Wei Gerard Ee, Wen Liang Joel Lau, William Yeo, Yap Von Bing, and Wai Mun Yue. Does minimally invasive surgery have a lower risk of surgical site infections compared with open spinal surgery? *Clinical Orthopaedics and Related Research®*, 472(6):1718–1724, 2014.

[63] Hung-Jui Tan, J Stuart Wolf Jr, Zaojun Ye, Khaled S Hafez, and David C Miller. Population level assessment of hospital based outcomes following laparoscopic versus open partial nephrectomy during the adoption of minimally invasive surgery. *The Journal of urology*, 191(5):1231–1237, 2014.

[64] James D Luketich, Arjun Pennathur, Omar Awais, Ryan M Levy, Samuel Keeley, Manisha Shende, Neil A Christie, Benny Weksler, Rodney J Landreneau, Ghulam Abbas, et al. Outcomes after minimally invasive esophagectomy: review of over 1000 patients. *Annals of surgery*, 256(1):95, 2012.

[65] KH Fuchs. Minimally invasive surgery. *Endoscopy*, 34(02):154–159, 2002.

[66] R Smith, A Day, T Rockall, K Ballard, M Bailey, and I Jourdan. Advanced stereoscopic projection technology significantly improves novice performance of minimally invasive surgical skills. *Surgical endoscopy*, 26(6):1522–1527, 2012.

[67] Michele Tonutti, Daniel S Elson, Guang-Zhong Yang, Ara W Darzi, and Mikael H Sodergren. The role of technology in minimally invasive surgery: state of the art, recent developments and future directions. *Postgraduate medical journal*, 93(1097):159–167, 2017.

[68] Laura A Snyder, John O'Toole, Kurt M Eichholz, Mick J Perez-Cruet, and Richard Fessler. The technological development of minimally invasive spine surgery. *BioMed research international*, 2014, 2014.

[69] THEODORE G OBENCHAIN. Laparoscopic lumbar discectomy: case report. *Journal of laparoendoscopic surgery*, 1(3):145–149, 1991.

[70] Ryan A Beasley. Medical robots: current systems and research directions. *Journal of Robotics*, 2012, 2012.

[71] JE Lang, S Mannava, AJ Floyd, MS Goddard, BP Smith, A Mofidi, TM Seyler, and RH Jinnah. Robotic systems in orthopaedic surgery. *Journal of Bone & Joint Surgery, British Volume*, 93(10):1296–1299, 2011.

[72] Anthony Adili. Robot-assisted orthopedic surgery. *Surgical Innovation*, 11(2):89–98, 2004.

[73] Amr Nimer Amr, Alf Giese, and Sven R Kantelhardt. Navigation and robot-aided surgery in the spine: historical review and state of the art. *Robotic Surgery: Research and Reviews*, 1:19–26, 2014.

[74] Nobuhiko Sugano. Computer-assisted orthopedic surgery. *Journal of Orthopaedic Science*, 8(3):442–448, 2003.

[75] Uli Mezger, Claudia Jendrewski, and Michael Bartels. Navigation in surgery. *Langenbeck's archives of surgery*, 398(4):501–514, 2013.

[76] Frank Langlotz, Manfred Stucki, Richard Bächler, Carsten Scheer, Reinhold Ganz, Ulrich Berlemann, and Lutz-P Nolte. The first twelve cases of computer assisted periacetabular osteotomy. *Computer Aided Surgery: Official Journal of the International Society for Computer Aided Surgery (ISCAS)*, 2(6):317–326, 1997.

[77] Rolf Haaker and Werner Konermann. *Computer and template assisted orthopedic surgery*. Springer Science & Business Media, 2013.

[78] Rolf Haaker. History of computer-assisted surgery. In *Computer and Template Assisted Orthopedic Surgery*, pages 3–9. Springer, 2013.

[79] LP Nolte, MA Slomczykowski, Uirich Berlemann, Matthias J Strauss, Robert Hofstetter, Dietrich Schlenzka, Timo Laine, and Teija Lund. A new approach to computer-aided spine surgery: fluoroscopy-based surgical navigation. *European Spine Journal*, 9(1):S078–S088, 2000.

[80] K Bouazza-Marouf, I Browbank, and JR Hewit. Robot-assisted invasive orthopaedic surgery. *Mechatronics*, 6(4):381–397, 1996.

[81] Russell H Taylor. A perspective on medical robotics. *Proceedings of the IEEE*, 94(9):1652–1664, 2006.

[82] James M Drake, James T Rutka, and Harold J Hoffman. Isg viewing wand system. *Neurosurgery*, 34(6):1094–1097, 1994.

[83] Eric P Sipos, Scot A Tebo, S James Zinreich, Donlin M Long, and Henry Brem. In vivo accuracy testing and clinical experience with the isg viewing wand. *Neurosurgery*, 39(1):194–204, 1996.

[84] Chris S Karas and E Antonio Chiocca. Neurosurgical robotics: a review of brain and spine applications. *Journal of robotic surgery*, 1(1):39–43, 2007.

[85] Arpád Takács, Dénes Ákos Nagy, Imre Rudas, and Tamás Haidegger. Origins of surgical robotics: From space to the operating room. *Acta Polytechnica Hungarica*, 13(1):13–30, 2016.

[86] TRK Varma and P Eldridge. Use of the neuromate stereotactic robot in a frameless mode for functional neurosurgery. *The International Journal of Medical Robotics and Computer Assisted Surgery*, 2(2):107–113, 2006.

[87] Qing Hang Li, Lucia Zamorano, Abhilash Pandya, Ramiro Perez, Jianxing Gong, and Fernando Diaz. The application accuracy of the neuromate robot—a quantitative comparison with frameless and frame-based surgical localization systems. *Computer Aided Surgery*, 7(2):90–98, 2002.

[88] Robert D Howe and Yoky Matsuoka. Robotics for surgery. *Annual review of biomedical engineering*, 1(1):211–240, 1999.

[89] Baowei Fei, Wan Sing Ng, Sunita Chauhan, and Chee Keong Kwoh. The safety issues of medical robotics. *Reliability Engineering & System Safety*, 73(2):183–192, 2001.

[90] Paolo Dario, Blake Hannaford, and Arianna Menciassi. Smart surgical tools and augmenting devices. *IEEE transactions on robotics and automation*, 19(5):782–792, 2003.

[91] Andrew D Pearle, Padhraig F O'Loughlin, and Daniel O Kendoff. Robot-assisted unicompartmental knee arthroplasty. *The Journal of arthroplasty*, 25(2):230–237, 2010.

[92] William L Bargar, André Bauer, and Martin Börner. Primary and revision total hip replacement using the robodoc (r) system. *Clinical Orthopaedics and Related Research (1976-2007)*, 354:82–91, 1998.

[93] Peter Kazanzides, Joel Zuhars, Brent Mittelstadt, and Russell H Taylor. Force sensing and control for a surgical robot. In *Proceedings 1992 IEEE International Conference on Robotics and Automation*, pages 612–617. IEEE, 1992.

[94] Joanne Pransky. Robodoc-surgical robot success story. *Industrial Robot: An International Journal*, 24(3):231–233, 1997.

[95] Michael Nogler, Anne Polikeit, Cornelius Wimmer, Andreas Brückner, Stephen J Ferguson, and Martin Krismer. Primary stability of a robodoc® implanted anatomical stem versus manual implantation. *Clinical Biomechanics*, 19(2):123–129, 2004.

[96] Joerg Petermann, Rudolf Kober, Rudolf Heinze, Jens Jeorg Frölich, Peter F Heeckt, and Leo Gotzen. Computer-assisted planning and robot-assisted surgery in anterior cruciate ligament reconstruction. *Operative techniques in Orthopaedics*, 10(1):50–55, 2000.

[97] Ryan A Beasley. Medical robots: current systems and research directions. *Journal of Robotics*, 2012, 2012.

[98] Andrew D Pearle, Daniel Kendoff, Volker Stueber, Volker Musahl, and John A Repicci. Perioperative management of unicompartmental knee arthroplasty using the mako robotic arm system (makoplasty). *American Journal of Orthopedics*, 38(2):16–19, 2009.

[99] Jacob Rosen, Blake Hannaford, and Richard M Satava. *Surgical robotics: systems applications and visions*. Springer Science & Business Media, 2011.

[100] Benny Hagag, Rony Abovitz, Hyosig Kang, Brian Schmitz, and Michael Conditt. Rio: Robotic-arm interactive orthopedic system makoplasty: user interactive haptic orthopedic robotics. In *Surgical Robotics*, pages 219–246. Springer, 2011.

[101] Martin Roche. Robotic-assisted unicompartmental knee arthroplasty: The mako experience. *Clinics in sports medicine*, 33(1):123–132, 2014.

[102] W Sukovich, S Brink-Danan, and M Hardenbrook. Miniature robotic guidance for pedicle screw placement in posterior spinal fusion: early clinical experience with the

spineassist®. *The International Journal of Medical Robotics and Computer Assisted Surgery*, 2(2):114–122, 2006.

[103] Y Barzilay, L Kaplan, and M Libergall. Robotic assisted spine surgery—a breakthrough or a surgical toy? *The International Journal of Medical Robotics and Computer Assisted Surgery*, 4(3):195–196, 2008.

[104] Florian Roser, Marcos Tatagiba, and Gottlieb Maier. Spinal robotics: current applications and future perspectives. *Neurosurgery*, 72(suppl_1):A12–A18, 2013.

[105] M Shoham, IH Lieberman, EC Benzel, D Togawa, E Zehavi, B Zilberstein, M Roffman, A Bruskin, A Fridlander, L Joskowicz, et al. Robotic assisted spinal surgery-from concept to clinical practice. *Computer Aided Surgery*, 12(2):105–115, 2007.

[106] Isador H Lieberman, Mitchell A Hardenbrook, Jeffrey C Wang, and Richard D Guyer. Assessment of pedicle screw placement accuracy, procedure time, and radiation exposure using a miniature robotic guidance system. *Journal of spinal disorders & techniques*, 25(5):241–248, 2012.

[107] Alexander Bruskin. Robotic assisted spinal surgery-2 years of clinical experience-gains and disadvantages. In *Orthopaedic Proceedings*, volume 94, pages 19–19. The British Editorial Society of Bone & Joint Surgery, 2012.

[108] Alvaro Bertelsen, Javier Melo, Emilio Sánchez, and Diego Borro. A review of surgical robots for spinal interventions. *The International Journal of Medical Robotics and Computer Assisted Surgery*, 9(4):407–422, 2013.

[109] L Joskowicz, R Shamir, Z Israel, Y Shoshan, and M Shoham. Renaissance robotic system for keyhole cranial neurosurgery: in-vitro accuracy study. In *Proceedings of the Simposio Mexicano en Ciruga Asistida por Computadora y Procesamiento de Imgenes Mdicas (MexCAS'11)*, 2011.

[110] Dennis P Devito, Leon Kaplan, Rupert Dietl, Michael Pfeiffer, Dale Horne, Boris Silberstein, Mitchell Hardenbrook, George Kiriyanthan, Yair Barzilay, Alexander Bruskin, et al. Clinical acceptance and accuracy assessment of spinal implants guided with spineassist surgical robot: retrospective study. *Spine*, 35(24):2109–2115, 2010.

[111] ONEN Mehmet Resid, Mehmet SıMSEK, and Sait NADER. Robotic spine surgery: a preliminary report. *Turk Neurosurg*, 24(4):512–518, 2014.

[112] John YK Lee, Deb A Bhowmick, Daniel D Eun, and William C Welch. Minimally invasive, robot-assisted, anterior lumbar interbody fusion: a technical note. *Journal of Neurological Surgery Part A: Central European Neurosurgery*, 74(04):258–261, 2013.

[113] Florian Ringel, Carsten Stüer, Andreas Reinke, Alexander Preuss, Michael Behr, Florian Auer, Michael Stoffel, and Bernhard Meyer. Accuracy of robot-assisted placement of lumbar and sacral pedicle screws: a prospective randomized comparison to conventional freehand screw implantation. *Spine*, 37(8):E496–E501, 2012.

[114] HWR Schreuder and RHM Verheijen. Robotic surgery. *BJOG: An International Journal of Obstetrics & Gynaecology*, 116(2):198–213, 2009.

[115] Constantin SCHizAS, Eric THEin, Barbara KwiATKOwSKi, and Gerit KULiK. Pedicle screw insertion: robotic assistance versus conventional c-arm fluoroscopy. *Acta Orthop Belg*, 78(2):240–245, 2012.

[116] Sven Rainer Kantelhardt, Ramon Martinez, Stefan Baerwinkel, Ralf Burger, Alf Giese, and Veit Rohde. Perioperative course and accuracy of screw positioning in conventional, open robotic-guided and percutaneous robotic-guided, pedicle screw placement. *European Spine Journal*, 20(6):860–868, 2011.

[117] Spinal Cerrahide Robotik Sistemlerin Kullanılması. Robotic systems in spine surgery. *Turk Neurosurg*, 24(3):305–311, 2014.

[118] Victor B Kim, William HH Chapman Iii, Robert J Albrecht, B Marcus Bailey, James A Young, L Wiley Nifong, and W Randolph Chitwood Jr. Early experience with telemanipulative robot-assisted laparoscopic cholecystectomy using da vinci. *Surgical Laparoscopy Endoscopy & Percutaneous Techniques*, 12(1):33–40, 2002.

[119] Jacob R Joseph, Brandon W Smith, Xilin Liu, and Paul Park. Current applications of robotics in spine surgery:

a systematic review of the literature. *Neurosurgical focus*, 42(5):E2, 2017.

[120] Dan Stoianovici, Jeffrey A Cadeddu, Roger D Demaree, Stephen A Basile, Russell H Taylor, Louis L Whitcomb, William N Sharpe, and Louis R Kavoussi. An efficient needle injection technique and radiological guidance method for percutaneous procedures. In *CVRMed-MRCAS'97*, pages 295–298. Springer, 1997.

[121] Dan Stoianovici, Louis L Whitcomb, James H Anderson, Russell H Taylor, and Louis R Kavoussi. A modular surgical robotic system for image guided percutaneous procedures. In *international conference on medical image computing and computer-assisted intervention*, pages 404–410. Springer, 1998.

[122] R Taylor, J Funda, D LaRose, Y Kim, N Bruun, N Swarup, C Cutting, and M Treat. A passive/active manipulation system for surgical augmentation. In *Proc. 1st Int. Workshop on Mechatronics in Medicine*, 1992.

[123] Russell H Taylor, Yong-yil Kim, Alan D Kalvin, David Larose, Betsy Haddad, Deljou Khoramabadi, Marilyn Noz, Robert Olyha, Nils Bruun, Dieter Grimm, et al. A model-based optimal planning and execution system with active sensing and passive manipulation for augmentation of human precision in computer-integrated surgery. In *Experimental Robotics II*, pages 177–195. Springer, 1993.

[124] Chin-Hsing Kuo, Jian S Dai, and Prokar Dasgupta. Kinematic design considerations for minimally invasive surgical robots: an overview. *The International Journal of Medical Robotics and Computer Assisted Surgery*, 8(2):127–145, 2012.

[125] RH Taylor and D Stoiariovici. gmedical robotics in computerintegrated surgery,• h ieee trans. *Robot. Automat*, 19(5):922–926, 2003.

[126] Yik San Kwoh, Joahin Hou, Edmond A Jonckheere, and Samad Hayati. A robot with improved absolute positioning accuracy for ct guided stereotactic brain surgery. *IEEE Transactions on Biomedical Engineering*, 35(2):153–160, 1988.

[127] Nabli Simaan and Moshe Shoham. Robot construction for surgical applications. *IFAC Proceedings Volumes*, 33(26):521–526, 2000.

[128] T Arai. Development of parallel link manipulator for underground excavation task. *Proc.'91 ISART, Tokyo, Japan*, 1991.

[129] Lung-Wen Tsai and Sameer Joshi. Kinematic analysis of 3-dof position mechanisms for use in hybrid kinematic machines. *Journal of Mechanical Design*, 124(2):245–253, 2002.

[130] Doug Stewart. A platform with six degrees of freedom. *Proceedings of the institution of mechanical engineers*, 180(1):371–386, 1965.

[131] YD Patel and PM George. Parallel manipulators applications—a survey. *Modern Mechanical Engineering*, 2(03):57, 2012.

[132] Chin-Hsing Kuo and Jian S Dai. Robotics for minimally invasive surgery: a historical review from the perspective of kinematics. In *International symposium on history of machines and mechanisms*, pages 337–354. Springer, 2009.

[133] Jianmin Li, Guokai Zhang, Andreas Müller, and Shuxin Wang. A family of remote center of motion mechanisms based on intersecting motion planes. *Journal of Mechanical Design*, 135(9):091009, 2013.

[134] Sang-Eun Song, Junichi Tokuda, Kemal Tuncali, Akimasa Yamada, Meysam Torabi, and Nobuhiko Hata. Design evaluation of a double ring rcm mechanism for robotic needle guidance in mri-guided liver interventions. In *Intelligent Robots and Systems (IROS), 2013 IEEE/RSJ International Conference on*, pages 4078–4083. IEEE, 2013.

[135] Guanghua Zong, Xu Pei, Jingjun Yu, and Shusheng Bi. Classification and type synthesis of 1-dof remote center of motion mechanisms. *Mechanism and Machine Theory*, 43(12):1585–1595, 2008.

[136] Serhat Aksungur. Remote center of motion (rcm) mechanisms for surgical operations. *International Journal of Applied Mathematics, Electronics and Computers*, 3(2):119–126, 2015.

[137] Colin Natali, Paul Ingle, and John Dowell. Orthopaedic bone drills–can they be improved? temperature changes near the drilling face. *The Journal of bone and joint surgery. British volume*, 78(3):357–362, 1996.

[138] Baohua Ji and Huajian Gao. Mechanical principles of biological nanocomposites. *Annual Review of Materials Research*, 40:77–100, 2010.

[139] Zhirong Liao and Dragos A Axinte. On chip formation mechanism in orthogonal cutting of bone. *International Journal of Machine Tools and Manufacture*, 102:41–55, 2016.

[140] J-Y Giraud, S Villemin, R Darmana, J-Ph Cahuzac, A Autefage, and J-P Morucci. Bone cutting. *Clinical Physics and Physiological Measurement*, 12(1):1, 1991.

[141] Yael Eshet, Ronit Rachel Mann, Abby Anaton, Tomer Yacoby, Amit Gefen, and Eli Jerby. Microwave drilling of bones. *IEEE transactions on biomedical engineering*, 53(6):1174–1182, 2006.

[142] Arthorn Sanpamch, Kusol Petsarb, Watchara Sroykham, Wirasak Angkhananuwat, Chaaim Phairoh, Chainapat Apaiwong, Sumethee Thanangkul, Youngyuth Kajornpredanon, and Pattarapong Phasukki. An investigation of microwave ablation for bone thermal drilling. In *Microwave Workshop Series on RF and Wireless Technologies for Biomedical and Healthcare Applications (IMWS-BIO), 2013 IEEE MTT-S International*, pages 1–2. IEEE, 2013.

[143] Titto John George, Apurba Kumar Sharma, Pradeep Kumar, Rajesh Kumar, and Shantanu Das. Microwave drilling: Future possibilities and challenges based on experimental studies. In *International Conference on Emerging Trends in Manufacturing Technology Toc H Institute of Science & Technology Kerela*, 2012.

[144] S den Dunnen and GJM Tuijthof. The influence of water jet diameter and bone structural properties on the efficiency of pure water jet drilling in porcine bone. *Mechanical Sciences*, 5(2):53–58, 2014.

[145] Pavol Hreha, Sergej Hloch, D Magurovd, Jan Valicek, Dražan Kozak, M Harnicdrovd, and Marko Rakin. Water jet technology used in medicine. *Tehnicki Vjesnik*, 17(2):237–240, 2010.

[146] Umberto Romeo, Alessandro Del Vecchio, Gaspare Palata, Gianluca Tenore, Paolo Visca, and Claudia Maggiore. Bone damage induced by different cutting instruments: an in vitro study. *Brazilian dental journal*, 20(2):162–168, 2009.

[147] K-W Baek, W Deibel, D Marinov, Mathias Griessen, A Bruno, H-F Zeilhofer, Ph Cattin, and Ph Juergens. Clinical applicability of robot-guided contact-free laser osteotomy in cranio-maxillo-facial surgery: in-vitro simulation and in-vivo surgery in minipig mandibles. *British Journal of Oral and Maxillofacial Surgery*, 53(10):976–981, 2015.

[148] Michael T Hillery and I Shuaib. Temperature effects in the drilling of human and bovine bone. *Journal of Materials Processing Technology*, 92:302–308, 1999.

[149] Anders R Eriksson, Tomas Albrektsson, and BjÖRn Albrektsson. Heat caused by drilling cortical bone: temperature measured in vivo in patients and animals. *Acta Orthopaedica Scandinavica*, 55(6):629–631, 1984.

[150] F Karaca, B Aksakal, and MJME Kom. Influence of orthopaedic drilling parameters on temperature and histopathology of bovine tibia: an in vitro study. *Medical engineering & physics*, 33(10):1221–1227, 2011.

[151] JuEun Lee, Yoed Rabin, and O Burak Ozdoganlar. A new thermal model for bone drilling with applications to orthopaedic surgery. *Medical engineering & physics*, 33(10):1234–1244, 2011.

[152] Nicky Bertollo, Hadley RM Milne, Liam P Ellis, Paul C Stephens, Ronald M Gillies, and William R Walsh. A comparison of the thermal properties of 2-and 3-fluted drills and the effects on bone cell viability and screw pull-out strength in an ovine model. *Clinical biomechanics*, 25(6):613–617, 2010.

[153] Brendon Noble, M Alini, and RG Richards. Bone microdamage and cell apoptosis. *Eur Cell Mater*, 6:46–55, 2003.

[154] Bas BGM Franssen, Paul J Van Diest, Arnold H Schuurman, and Moshe Kon. Drilling k-wires, what about the osteocytes? an experimental study in rabbits. *Archives of orthopaedic and trauma surgery*, 128(1):83–87, 2008.

[155] AR Eriksson and T Albrektsson. Temperature threshold levels for heat-induced bone tissue injury: a vital-microscopic study in the rabbit. *Journal of prosthetic dentistry*, 50(1):101–107, 1983.

[156] W Bonfield and CH Li. The temperature dependence of the deformation of bone. *Journal of biomechanics*, 1(4):323–329, 1968.

[157] Arnold T Berman, J SPENCE Reid, Jr DR Yanicko, George C Sih, and MR Zimmerman. Thermally induced bone necrosis in rabbits. relation to implant failure in humans. *Clinical orthopaedics and related research*, 1(186):284–292, 1984.

[158] HC Thompson. Effect of drilling into bone. *Journal of oral surgery*, 16(1):22–30, 1958.

[159] RCt Vaughn and FA Peyton. The influence of rotational speed on temperature rise during cavity preparation. *Journal of dental research*, 30(5):737–744, 1951.

[160] Philip J Boyne. Histologic response of bone to sectioning by high-speed rotary instruments. *Journal of dental research*, 45(2):270–276, 1966.

[161] Richard W Moss. Histopathologic reaction of bone to surgical cutting. *Oral Surgery, Oral Medicine, Oral Pathology*, 17(3):405–414, 1964.

[162] Sherman Spatz. Early reaction in bone following the use of burs rotating at conventional and ultra speeds: A comparison study. *Oral Surgery, Oral Medicine, Oral Pathology*, 19(6):808–816, 1965.

[163] Larry S Matthews and Carl Hirsch. Temperatures measured in human cortical bone when drilling. *JBJS*, 54(2):297–308, 1972.

[164] CH Jacob, JT Berry, MH Pope, and FT Hoaglund. A study of the bone machining process—drilling. *Journal of Biomechanics*, 9(5):345–349, 1976.

[165] Mustafa B Abouzgia and David F James. Measurements of shaft speed while drilling through bone. *Journal of Oral and Maxillofacial Surgery*, 53(11):1308–1315, 1995.

[166] S Karmani and F Lam. The design and function of surgical drills and k-wires. *Current Orthopaedics*, 18(6):484–490, 2004.

[167] M Eugene Merchant. Mechanics of the metal cutting process. i. orthogonal cutting and a type 2 chip. *Journal of applied physics*, 16(5):267–275, 1945.

[168] Giampiero Cordioli and Zeina Majzoub. Heat generation during implant site preparation: an in vitro study. *International Journal of Oral & Maxillofacial Implants*, 12(2), 1997.

[169] Sherif H Tehemar. Factors affecting heat generation during implant site preparation: a review of biologic observations and future considerations. *Int J Oral Maxillofac Implants*, 14(1):127–36, 1999.

[170] Eyup Bagci and Babur Ozcelik. Effects of different cooling conditions on twist drill temperature. *The International Journal of Advanced Manufacturing Technology*, 34(9-10):867–877, 2007.

[171] Varahalaraju Kalidindi. Optimization of drill design and coolant systems during dental implant surgery. 2004.

[172] Goran Augustin, Slavko Davila, Toma Udilljak, Tomislav Staroveski, Danko Brezak, and Slaven Babic. Temperature changes during cortical bone drilling with a newly designed step drill and an internally cooled drill. *International orthopaedics*, 36(7):1449–1456, 2012.

[173] T Hüfner, J Geerling, G Oldag, M Richter, M Kfuri Jr, T Pohlemann, and C Krettek. Accuracy study of computer-assisted drilling: the effect of bone density, drill bit characteristics, and use of a mechanical guide. *Journal of orthopaedic trauma*, 19(5):317–322, 2005.

[174] Marcin Basiaga, Zbigniew Paszenda, Janusz Szewczenko, and MARCIN Kaczmarek. Numerical and experimental analyses of drills used in osteosynthesis. *Acta of Bioengineering and Biomechanics*, 13(4):29–36, 2011.

[175] Sean RH Davidson and David F James. Drilling in bone: modeling heat generation and temperature distribution. *Journal of Biomechanical Engineering*, 125(3):305–314, 2003.

[176] Simin Li, Adel Abdel-Wahab, Emrah Demirci, and Vadim V Silberschmidt. Penetration of cutting tool into cortical bone: experimental and numerical investigation of anisotropic mechanical behaviour. *Journal of biomechanics*, 47(5):1117–1126, 2014.

[177] Z Paszenda and M Basiaga. Fem analysis of drills used in bone surgery. *Archives of Materials Science and Engineering*, 36(2):103–109, 2009.

[178] Miguel Marco, Marcos Rodríguez-Millán, Carlos Santiuste, Eugenio Giner, and María Henar Miguélez. A review on recent advances in numerical modelling of bone cutting. *Journal of the mechanical behavior of biomedical materials*, 44:179–201, 2015.

[179] Arne G Nielsen, James R Richards, and Robert B Wolcott. Ultrasonic dental cutting instrument: I. *The Journal of the American Dental Association*, 50(4):392–399, 1955.

[180] Lewis Balamuth. Ultrasonics and dentistry. *Sound: Its Uses and Control*, 2(2):15–19, 1963.

[181] Matthew C Catuna. Sonic energy; a possible dental application. *Ann. Dent.*, 12:100–101, 1953.

[182] VA Polyakov. *Ultrasonic bonding of bones and cutting of live biological tissues*. Mir Publ, 1974.

[183] Vang Alfred. Vibratory surgical instruments, August 9 1955. US Patent 2,714,890.

[184] MV Volkov. The use of ultrasonic instrumentation for the transection and uniting of bone tissue in orthopaedic surgery. *Reconstr Surg Traumatol*, 14:147–152, 1974.

[185] Andrew Mathieson, Andrea Cardoni, Niccolò Cerisola, and Margaret Lucas. Understanding nonlinear vibration behaviours in high-power ultrasonic surgical devices. *Proc. R. Soc. A*, 471(2176):20140906, 2015.

[186] HB Mazorow. Bone repair after experimentally produced defects. *J Oral Surg, Anesth & Hosp D Serv*, 18:107–115, 1960.

[187] TA McFall, GM Yamane, and GW Burnett. Comparison of the cutting effect on bone of an ultrasonic cutting device and rotary burs. *Journal of oral surgery, anesthesia, and hospital dental service*, 19:200–209, 1961.

[188] John E Horton, Thomas M Tarpley, and Larry D Wood. The healing of surgical defects in alveolar bone produced with ultrasonic instrumentation, chisel, and rotary bur. *Oral Surgery, Oral Medicine, Oral Pathology*, 39(4):536–546, 1975.

[189] John E Horton, Thomas M Tarpley, and John R Jacoway. Clinical applications of ultrasonic instrumentation in the surgical removal of bone. *Oral Surgery, Oral Medicine, Oral Pathology*, 51(3):236–242, 1981.

[190] H Aro, H Kallioniemi, AJ Aho, and P Kellokumpu-Lehtinen. Ultrasonic device in bone cutting: A histological and scanning electron microscopical study. *Acta Orthopaedica Scandinavica*, 52(1):5–10, 1981.

[191] BS Khambay and AD Walmsley. Investigations into the use of an ultrasonic chisel to cut bone. part 1: forces applied by clinicians. *Journal of dentistry*, 28(1):31–37, 2000.

[192] T Vercellotti, A Crovace, A Palermo, and A Molfetta. The piezoelectric osteotomy in orthopedics: clinical and histological evaluations (pilot study in animals). *Mediterr J Surg Med*, 9:89–96, 2001.

[193] Philippe Leclercq, Charlotte Zenati, Sarah Amr, and David M Dohan. Ultrasonic bone cut part 1: State-of-the-art technologies and common applications. *Journal of Oral and Maxillofacial Surgery*, 66(1):177–182, 2008.

[194] Brendan J O'Daly, Edmund Morris, Graham P Gavin, John M O'Byrne, and Garrett B McGuinness. High-power low-frequency ultrasound: A review of tissue dissection and ablation in medicine and surgery. *Journal of materials processing technology*, 200(1-3):38–58, 2008.

[195] G Pavlíková, R Foltán, M Horká, T Hanzelka, H Borunská, and J Šedỳ. Piezosurgery in oral and maxillofacial surgery. *International journal of oral and maxillofacial surgery*, 40(5):451–457, 2011.

[196] Alberto González-García, Márcio Diniz-Freitas, Manuel Somoza-Martín, and Abel García-García. Ultrasonic osteotomy in oral surgery and implantology. *Oral Surgery, Oral Medicine, Oral Pathology, Oral Radiology, and Endodontology*, 108(3):360–367, 2009.

[197] Cornelio Blus and Serge Szmukler-Moncler. Split-crest and immediate implant placement with ultra-sonic bone surgery: a 3-year life-table analysis with 230 treated sites. *Clinical Oral Implants Research*, 17(6):700–707, 2006.

[198] Stefan Schaeren, Claude Jaquiéry, Michael Heberer, Markus Tolnay, Tomaso Vercellotti, and Ivan Martin. Assessment of nerve damage using a novel ultrasonic device for bone cutting. *Journal of oral and maxillofacial surgery*, 66(3):593–596, 2008.

[199] Constantin A Landes, Stefan Stübinger, Jörg Rieger, Babett Williger, Thi Khanh Linh Ha, and Robert Sader. Critical evaluation of piezoelectric osteotomy in orthognathic surgery: operative technique, blood loss, time requirement, nerve and vessel integrity. *Journal of Oral and Maxillofacial Surgery*, 66(4):657–674, 2008.

[200] Dipesh Parmar, Malveen Mann, A Damien Walmsley, and Simon C Lea. Cutting characteristics of ultrasonic surgical instruments. *Clinical oral implants research*, 22(12):1385–1390, 2011.

[201] Philippe Hennet. Piezoelectric bone surgery: a review of the literature and potential applications in veterinary oromaxillofacial surgery. *Frontiers in veterinary science*, 2:8, 2015.

[202] B Kotrikova, R Wirtz, R Krempien, J Blank, G Eggers, A Samiotis, and J Mühling. Piezosurgery—a new safe technique in cranial osteoplasty? *International journal of oral and maxillofacial surgery*, 35(5):461–465, 2006.

[203] Arnaud Gleizal, Jean-Christophe Bera, Bernard Lavandier, and Jean-Luc Beziat. Piezoelectric osteotomy: a new technique for bone surgery—advantages in craniofacial surgery. *Child's Nervous System*, 23(5):509–513, 2007.

[204] Giuseppe Spinelli, Davide Lazzeri, Marco Conti, Tommaso Agostini, and Giuditta Mannelli. Comparison of

piezosurgery and traditional saw in bimaxillary orthognathic surgery. *Journal of Cranio-Maxillofacial Surgery*, 42(7):1211–1220, 2014.

[205] J-L Beziat, J-C Bera, B Lavandier, and A Gleizal. Ultrasonic osteotomy as a new technique in craniomaxillofacial surgery. *International journal of oral and maxillofacial surgery*, 36(6):493–500, 2007.

[206] Bernhard J Schaller, R Gruber, H A Merten, Thomas Kruschat, H Schliephake, Michael Buchfelder, and H C Ludwig. Piezoelectric bone surgery: a revolutionary technique for minimally invasive surgery in cranial base and spinal surgery? technical note. *Operative Neurosurgery*, 57(suppl_4):ONS–E410, 2005.

[207] Yue Zhang, Chengyong Wang, Shaobo Zhou, Wentao Jiang, Zhihua Liu, and Linlin Xu. A comparison review on orthopedic surgery using piezosurgery and conventional tools. *Procedia CIRP*, 65:99–104, 2017.

[208] Markus Martini, Andreas Röhrig, Rudolf Hermann Reich, and Martina Messing-Jünger. Comparison between piezosurgery and conventional osteotomy in cranioplasty with fronto-orbital advancement. *Journal of Cranio-Maxillofacial Surgery*, 45(3):395–400, 2017.

[209] Luigi Piersanti, Matteo Dilorenzo, Giuseppe Monaco, and Claudio Marchetti. Piezosurgery or conventional rotatory instruments for inferior third molar extractions? *Journal of Oral and Maxillofacial Surgery*, 72(9):1647–1652, 2014.

[210] Georg Eggers, Johannes Klein, Julia Blank, and Stefan Hassfeld. Piezosurgery®: an ultrasound device for cutting bone and its use and limitations in maxillofacial surgery. *British Journal of oral and maxillofacial surgery*, 42(5):451–453, 2004.

[211] Philippe Leclercq, Charlotte Zenati, and David M Dohan. Ultrasonic bone cut part 2: state-of-the-art specific clinical applications. *Journal of Oral and Maxillofacial Surgery*, 66(1):183–188, 2008.

[212] G Chiriac, M Herten, F Schwarz, D Rothamel, and J Becker. Autogenous bone chips: influence of a new

piezoelectric device (piezosurgery®) on chip morphology, cell viability and differentiation. *Journal of clinical periodontology*, 32(9):994–999, 2005.

[213] Rafid Al-Mahfoudh, Eman Qattan, Jonathan Richard Ellenbogen, Martin Wilby, Chris Barrett, and Tim Piggott. Applications of the ultrasonic bone cutter in spinal surgery–our preliminary experience. *British journal of neurosurgery*, 28(1):56–60, 2014.

[214] Juergen Grauvogel, Christian Scheiwe, and Jan Kaminsky. Use of piezosurgery for removal of retrovertebral body osteophytes in anterior cervical discectomy. *The Spine Journal*, 14(4):628–636, 2014.

[215] Dominik J Hoigne, Stefan Stübinger, Oliver Von Kaenel, Sonia Shamdasani, and Paula Hasenboehler. Piezoelectric osteotomy in hand surgery: first experiences with a new technique. *BMC Musculoskeletal disorders*, 7(1):36, 2006.

[216] Angelo Salami, Tommaso Vercellotti, Renzo Mora, and Massimo Dellepiane. Piezoelectric bone surgery in otologic surgery. *Otolaryngology-Head and Neck Surgery*, 136(3):484–485, 2007.

[217] Dawn K De Castro, Aaron Fay, Edward J Wladis, John Nguyen, Tammy Osaki, Ralph Metson, and William Curry. Self-irrigating piezoelectric device in orbital surgery. *Ophthalmic Plastic & Reconstructive Surgery*, 29(2):118–122, 2013.

[218] Khurshid Alam, AV Mitrofanov, and Vadim V Silberschmidt. Experimental investigations of forces and torque in conventional and ultrasonically-assisted drilling of cortical bone. *Medical engineering & physics*, 33(2):234–239, 2011.

[219] N Ahmed, AV Mitrofanov, VI Babitsky, and VV Silberschmidt. Analysis of forces in ultrasonically assisted turning. *Journal of Sound and Vibration*, 308(3-5):845–854, 2007.

[220] Khurshid Alam, Abdul Ghafoor, and Vadim V Silberschmidt. Analysis of forces and temperatures in conventional and ultrasonically-assisted cutting of bone. In *Advanced Materials Research*, volume 223, pages 247–254. Trans Tech Publ, 2011.

[221] K Alam and Vadim V Silberschmidt. Analysis of temperature in conventional and ultrasonically-assisted drilling of cortical bone with infrared thermography. *Technology and Health Care*, 22(2):243–252, 2014.

[222] T Vercellotti. Technological characteristics and clinical indications of piezoelectric bone surgery. *Minerva stomatologica*, 53(5):207–214, 2004.

[223] Y Raja Rampersaud, Kevin T Foley, Alfred C Shen, Scott Williams, and Milo Solomito. Radiation exposure to the spine surgeon during fluoroscopically assisted pedicle screw insertion. *Spine*, 25(20):2637–2645, 2000.

[224] Roy Sanders, Kenneth J Koval, Thomas DiPasquale, Gregory Schmelling, Steven Stenzler, and Eric Ross. Exposure of the orthopaedic surgeon to radiation. *The Journal of bone and joint surgery. American volume*, 75(3):326–330, 1993.

[225] PN Brett, CA Fraser, M Hennigan, MV Griffiths, and Y Kamel. Automatic surgical tools for penetrating flexible tissues. *IEEE Engineering in Medicine and Biology Magazine*, 14(3):264–270, 1995.

[226] FR Ong and K Bouazza-Marouf. The detection of drill bit break-through for the enhancement of safety in mechatronic assisted orthopaedic drilling. *Mechatronics*, 9(6):565–588, 1999.

[227] R Taylor, X Du, D Proops, A Reid, C Coulson, and PN Brett. A sensory-guided surgical micro-drill. *Proceedings of the Institution of Mechanical Engineers, Part C: Journal of Mechanical Engineering Science*, 224(7):1531–1537, 2010.

[228] B Allotta, F Belmonte, L Bosio, and P Dario. Study on a mechatronic tool for drilling in the osteosynthesis of long bones: tool/bone interaction, modeling and experiments. *Mechatronics*, 6(4):447–459, 1996.

[229] Peter N Brett, Andrew J Harrison, and Trevor A Thomas. Schemes for the identification of tissue types and boundaries at the tool point for surgical needles. *IEEE Transactions on Information Technology in Biomedicine*, 4(1):30–36, 2000.

[230] Wen-Yo Lee, Ching-Long Shih, and Shih-Tseng Lee. Force control and breakthrough detection of a bone-drilling system. *IEEE/ASME Transactions on Mechatronics*, 9(1):20–29, 2004.

[231] Benedetto Allotta, Giuseppe Giacalone, and Luigi Rinaldi. A hand-held drilling tool for orthopedic surgery. *IEEE/ASME Transactions on Mechatronics*, 2(4):218–229, 1997.

[232] Wayne Anderson. Depth controllable and measurable medical driver devices and methods of use, September 2 2014. US Patent 8,821,493.

[233] Benedetto Allotta. Surgical drill with bit penetration control and breakthrough detection, March 7 2000. US Patent 6,033,409.

[234] Yeh-Liang Hsu, Shih-Tseng Lee, Chong-Fai Wang, Jia-Wen Chen, Hao-Wei Lin, and Tsung-Cheng Huang. Automatic bone drilling apparatus for surgery operation, January 8 2002. US Patent 6,336,931.

[235] Wen-Yo Lee and Ching-Long Shih. Control and breakthrough detection of a three-axis robotic bone drilling system. *Mechatronics*, 16(2):73–84, 2006.

[236] Zahari Taha, A Salah, and J Lee. Bone breakthrough detection for orthopedic robot-assisted surgery. In *APIEMS 2008 Proceedings of the 9th Asia Pacific Industrial Engineering and Management Systems Conference*, pages 2742–2746, 2008.

[237] R Kastelov, G Boiadjiev, T Boiadjiev, V Vitkov, K Delchev, K Zagurski, and I Veneva. Automation of bone drilling in the orthopedic surgery: Accuracy. In *12 th Congress of European Federation of Orthopedics and Traumatology, EFORT*, pages 1–4, 2011.

[238] Kazimir Zagurski, Toni Boiadjiev, Georgi Boiadjiev, Kamen Delchev, Rumen Kastelov, and Vladimir Vitkov. Automatic bone drilling in surgery: safety conditions improvement. *Journal Problems of Engineering Cybernetics and Robotics*, 65:85–91, 2012.

[239] George Boiadjiev, Vladimir Kotev, Kazimir Zagurski, Kamen Delchev, Tony Boiadjiev, and Rumen Kastelov. Robotized system for bone drilling and cutting in orthopedic surgery. In *Advanced Materials Research*, volume 740, pages 92–98. Trans Tech Publ, 2013.

[240] M Shoham, IH Lieberman, EC Benzel, D Togawa, E Zehavi, B Zilberstein, M Roffman, A Bruskin, A Fridlander, L Joskowicz, et al. Robotic assisted spinal surgery–from concept to clinical practice. *Computer Aided Surgery*, 12(2):105–115, 2007.

[241] Vishal Gupta, Pulak M Pandey, and Vadim V Silberschmidt. Rotary ultrasonic bone drilling: Improved pullout strength and reduced damage. *Medical engineering & physics*, 41:1–8, 2017.

[242] K Alam, Edris Hassan, Syed Husain Imran, and Mushtaq Khan. In-vitro analysis of forces in conventional and ultrasonically assisted drilling of bone. *Bio-medical materials and engineering*, 27(1):101–110, 2016.

[243] Edward L Duran and Ralph L Lundin. Ultrasonic drilling apparatus, May 9 1989. US Patent 4,828,052.

[244] Toshiiku Sashida and Takashi Kenjo. Introduction to ultrasonic motors. 1993.

[245] Karl F Graff. A history of ultrasonics. In *Physical acoustics*, volume 15, pages 1–97. Elsevier, 1981.

[246] Pierre Louis Leonard Marie Derks. *The design of ultrasonic resonators with wide output cross-sections*. PhD thesis, Technische Hogeschool Eindhoven, 1984.

[247] Wolfgang Sachse and Nelson N Hsu. Ultrasonic transducers for materials testing and their characterization. In *Physical acoustics*, volume 14, pages 277–406. Elsevier, 1979.

[248] Amir Abdullah, Mohsen Shahini, and Abbas Pak. An approach to design a high power piezoelectric ultrasonic transducer. *Journal of Electroceramics*, 22(4):369–382, 2009.

[249] Sheng-He Wang and Mi-Ching Tsai. Dynamic modeling of thickness-mode piezoelectric transducer using the block diagram approach. *Ultrasonics*, 51(5):617–624, 2011.

[250] L Svilainis and V Dumbrava. Evaluation of the ultrasonic transducer electrical matching performance. *Ultragarsas" Ultrasound"*, 62(4):16–21, 2007.

[251] DA DeAngelis, GW Schulze, and KS Wong. Optimizing piezoelectric stack preload bolts in ultrasonic transducers. *Physics Procedia*, 63:11–20, 2015.

[252] Dominick A DeAngelis. Predicting the displacement gain from the mechanical quality factor in ultrasonic transducers. *Physics Procedia*, 87:2–9, 2016.

[253] Zeina Abdallah, Yann G Boucher, Arnaud Fernandez, Stéphane Balac, and Olivier Llopis. Radio frequency spectral characterization and model parameters extraction of high q optical resonators. *Scientific reports*, 6:27208, 2016.

[254] Cleofé Campos-Pozuelo and Juan Antonio Gallego-Juárez. Limiting strain of metals subjected to high-intensity ultrasound. *Acta Acustica united with Acustica*, 82(6):823–828, 1996.

[255] VA Kuz'menko. Fatigue strength of structural materials at sonic and ultrasonic loading frequencies. *Ultrasonics*, 13(1):21–30, 1975.

[256] Aditya Chauhan, Rahul Vaish, and Chris Bowen. Piezoelectric material selection for ultrasonic transducer and actuator applications. *Proceedings of the Institution of Mechanical Engineers, Part L: Journal of Materials: Design and Applications*, 229(1):3–12, 2015.

[257] Shuyu Lin and Jie Xu. Effect of the matching circuit on the electromechanical characteristics of sandwiched piezoelectric transducers. *Sensors*, 17(2):329, 2017.

[258] Qiming M Zhang and Jianzhong Zhao. Electromechanical properties of lead zirconate titanate piezoceramics under the influence of mechanical stresses. *IEEE transactions on ultrasonics, ferroelectrics, and frequency control*, 46(6):1518–1526, 1999.

[259] James F Tressler, Sedat Alkoy, and Robert E Newnham. Piezoelectric sensors and sensor materials. *Journal of electroceramics*, 2(4):257–272, 1998.

[260] JA Gallego-Juarez. Piezoelectric ceramics and ultrasonic transducers. *Journal of Physics E: Scientific Instruments*, 22(10):804, 1989.

[261] Kenji Uchino. Piezoelectric ultrasonic motors: overview. *Smart Materials and Structures*, 7(3):273–285, jun 1998.

[262] K. Uchino. Materials issues in design and performance of piezoelectric actuators: an overview. *Acta Materialia*, 46(11):3745 – 3753, 1998.

[263] Yang Kuang. *Resonance tracking and vibration stabilisation of ultrasonic surgical instruments*. PhD thesis, University of Dundee, 2014.

[264] A. Ramos-Fernandez, J.A. Gallego-Juarez, and F. Montoya-Vitini. Automatic system for dynamic control of resonance in high power and high q ultrasonic transducers. *Ultrasonics*, 23(4):151 – 156, 1985.

[265] Mikio Umeda, Kentaro Nakamura, and Sadayuki Ueha. The measurement of high-power characteristics for a piezoelectric transducer based on the electrical transient response. *Japanese Journal of Applied Physics*, 37(Part 1, No. 9B):5322–5325, sep 1998.

[266] Y. Kuang, Y. Jin, S. Cochran, and Z. Huang. Resonance tracking and vibration stablilization for high power ultrasonic transducers. *Ultrasonics*, 54(1):187 – 194, 2014.

[267] F.J. Arnold, R.L. Ximenes, R. Arthur, and S.S. Mühlen. A driver for piezoelectric transducers with control of resonance. *Physics Procedia*, 63:114 – 119, 2015. 43rd Annual UIA Symposium 23—25 April 2014 CSIC Madrid, Spain.

[268] Edmund J.F. Dickinson, Henrik Ekström, and Ed Fontes. Comsol multiphysics®: Finite element software for electrochemical analysis. a mini-review. *Electrochemistry Communications*, 40:71 – 74, 2014.

[269] Andrea Cardoni and Margaret Lucas. Enhanced vibration performance of ultrasonic block horns. *Ultrasonics*, 40(1-8):365–369, 2002.

[270] Alan MacBeath. *Ultrasonic bone cutting*. PhD thesis, University of Glasgow, 2006.

[271] Simona Valentini. *Impedance in Human-Machine interaction*. PhD thesis, School of engineering, Università Campus Bio-Medico di Roma, 2018.

[272] FG Evans and FG Evans. Mechanical properties of bone. charles c. thomas. *Springfield. 1lll*, 1973.

[273] Frank Linde, Ivan Hvid, and Frank Madsen. The effect of specimen geometry on the mechanical behaviour of trabecular bone specimens. *Journal of biomechanics*, 25(4):359–368, 1992.

[274] Amy L Evans, Margaret A Paggiosi, Richard Eastell, and Jennifer S Walsh. Bone density, microstructure and strength in obese and normal weight men and women in younger and older adulthood. *Journal of Bone and Mineral Research*, 30(5):920–928, 2015.

[275] Georg Osterhoff, Elise F Morgan, Sandra J Shefelbine, Lamya Karim, Laoise M McNamara, and Peter Augat. Bone mechanical properties and changes with osteoporosis. *Injury*, 47:S11–S20, 2016.

[276] Melanie Schorr, Anne Drabkin, Micol S Rothman, Erinne Meenaghan, Gillian T Lashen, Margherita Mascolo, Ashlie Watters, Tara M Holmes, Kate Santoso, Elaine W Yu, et al. Bone mineral density and estimated hip strength in men with anorexia nervosa, atypical anorexia nervosa and avoidant/restrictive food intake disorder. *Clinical endocrinology*, 90(6):789–797, 2019.

[277] F Chagneau and M Levasseur. Mechanical analysis of bone structures by dynamostratigraphy. *European journal of mechanics. A. Solids*, 11(4):551–571, 1992.

[278] T Karalis and P Galanos. Research on the mechanical impedance of human bone by a drilling test. *Journal of biomechanics*, 15(8):561–581, 1982.

[279] MICHAEL D Smith, DIANNA DICKIE Cody, STEVEN A Goldstein, ANDREW M Cooperman, LARRY S Matthews, and MICHAEL J Flynn. Proximal femoral bone density and its correlation to fracture load and hip-screw penetration load. *Clinical orthopaedics and related research*, (283):244–251, 1992.

[280] Joseph J Schreiber, Paul A Anderson, and Wellington K Hsu. Use of computed tomography for assessing bone mineral density. *Neurosurgical focus*, 37(1):E4, 2014.

[281] Qasim Zaidi, Olumide A Danisa, and Wayne Cheng. Measurement techniques and utility of hounsfield unit values for assessment of bone quality prior to spinal instrumentation: a review of current literature. *Spine*, 44(4):E239–E244, 2019.

[282] Shaun P Patel, John J Lee, Garin G Hecht, Sven A Holcombe, Stewart C Wang, and James A Goulet. Normative vertebral hounsfield unit values and correlation with bone mineral density. *Journal of Clinical & Experimental Orthopaedics*, 2(1), 2016.

[283] N Batawil and S Sabiq. Hounsfield unit for the diagnosis of bone mineral density disease: A proof of concept study. *Radiography*, 22(2):e93–e98, 2016.

[284] Joseph J Schreiber, Paul A Anderson, Humberto G Rosas, Avery L Buchholz, and Anthony G Au. Hounsfield units for assessing bone mineral density and strength: a tool for osteoporosis management. *JBJS*, 93(11):1057–1063, 2011.

[285] Joshua Broder and Robert Preston. Chapter 1 - imaging the head and brain. In Joshua Broder, editor, *Diagnostic Imaging for the Emergency Physician*, pages 1 – 45. W.B. Saunders, Saint Louis, 2011.

[286] Joshua Broder. Chapter 9 - imaging of nontraumatic abdominal conditions. In Joshua Broder, editor, *Diagnostic Imaging for the Emergency Physician*, pages 445 – 577. W.B. Saunders, Saint Louis, 2011.

[287] N L Tagliamonte, F Sergi, G Carpino, D Accoto, and E Guglielmelli. Design of a variable impedance differential actuator for wearable robotics applications. *Intelligent Robots and Systems (IROS), 2010 IEEE/RSJ International Conference on*, pages 2639 – 2644, 2010.

[288] Dino Accoto, Giorgio Carpino, Fabrizio Sergi, Nevio Luigi Tagliamonte, Loredana Zollo, and Eugenio Guglielmelli. Design and characterization of a novel high-power series elastic actuator for a lower limbs

robotic orthosis. *International Journal of Advanced Robotic Systems*, 10, 2013.

[289] Nevio Luigi Tagliamonte, Fabrizio Sergi, Dino Accoto, Giorgio Carpino, and Eugenio Guglielmelli. Double actuation architectures for rendering variable impedance in compliant robots: A review. *Mechatronics*, 22(8):1187 – 1203, 2012.

[290] Andrea Cardoni, Patrick Harkness, and Margaret Lucas. Ultrasonic rock sampling using longitudinal-torsional vibrations. *Physics Procedia*, 3(1):125–134, 2010.

[291] Hassan Dakhil Al-Budairi. *Design and analysis of ultrasonic horns operating in longitudinal and torsional vibration*. PhD thesis, University of Glasgow, 2012.

[292] Yinchao Wang, He Li, Deen Bai, Qiquan Quan, Hongying Yu, Dewei Tang, and Zongquan Deng. A rotary-percussive ultrasonic drill for planetary rock sampling. In *2016 IEEE/RSJ International Conference on Intelligent Robots and Systems (IROS)*, pages 2966–2971. IEEE, 2016.

[293] Dajun Zhao, Shulei Zhang, Yan Zhao, and Meiyan Wang. Experimental study on damage characteristics of granite under ultrasonic vibration load based on infrared thermography. *Environmental Earth Sciences*, 78(14):419, 2019.